

Kochi University of Technology  
Department of Environmental Science and Engineering  
Kochi, Japan

**A Study of Degradation Mechanism of In-Ga-Zn-O  
Thin-Film Transistor under Negative Bias-Illumination Stress  
and Positive Bias Stress for Highly Reliable Display Devices**

Ph.D candidate: **Mai Phi Hung**

Supervisor: **Prof. Mamoru Furuta**

A dissertation submitted to Kochi University of Technology  
in partial fulfillment of the requirements for  
the degree of Doctor of Engineering

September, 2015

# Acknowledgements

It is with immense gratitude that I acknowledge the support and help of all those who have been beside me during my research period and the preparation of this thesis.

Particular thanks are due to my academic supervisor, **Prof. Mamoru Furuta**, professor of Kochi University of Technology (KUT), for his insightful advice, continuous encouragement and patient personal counseling as well as the guidance and commendation he has given me. I would like to thank my co-advisors *Prof. T.Maeda*, *Prof. L.Chaoyang*, *A.Prof. S.Momota* and *A.Prof. Nitta Noriko* for their kindly help.

I wish to express my gratitude and sincere thanks to *Dr. Dapeng Wang*, assistance professor of KUT, for teaching me fabrication and evaluation techniques. Your support in both research work and life helped me a lot. I would also like to thank *A.Prof. Kawaharamura Toshiyuki* for teaching me XRD, XRR, and mist CVD, and *A.Prof. Nitta Noriko*, who introduced me FIB and FE-SEM. I really appreciate *Prof. Hiroshi Furuta* 's help with fitting the XRR data.

I am very grateful to *Prof. Lawrence Hunter*, who spent a lot of time and effort on editing my papers. Your academic English writing courses were one of the most effective courses that I have taken in KUT.

I sincerely appreciate *Shane-san*, *Yoshida Motoi-san* and Mr. Toda for helping me establishing my life in Japan. I would like to thank to the M.Furuta lab members for their cooperation and academic support.

I really appreciate Prof. Kubo, Ms. Mari Yamasaki, Ms. Sakamoto Kimiko, Ms. Miki Okauchi, Ms. Saki Hamamura and all KUT IRC staff members for helping to make my life in Japan comfortable, and memorable.

Words cannot express my gratitude to my family for their encouragement and many sacrifices to ensure I was able to complete the study.

# **A Study of Degradation Mechanism of In-Ga-Zn-O Thin-Film Transistor under Negative Bias-Illumination Stress and Positive Bias Stress for Highly Reliable Display Devices**

## **Abstract**

In-Ga-Zn-O (IGZO) is an ionic amorphous oxide semiconductor, which has high field effect mobility ( $10 \sim 30 \text{ cm}^2/\text{Vs}$ ), transparency to visible light (bandgap of  $\sim 3.2 \text{ eV}$ ), and room temperature deposition. These properties make IGZO thin film transistors (TFTs) a promising candidate for active-matrix backplane of flat panel displays (FPDs). Low power consumption, high frame rate, and ultra-high resolution are some advantages of FPDs driven by an IGZO TFT array compared with an amorphous Si TFT. In FPDs, a negative voltage is normally applied to the gate electrode when the pixel is held. Besides that, TFTs can also be illuminated by back light unit. Therefore, the TFTs are operated under negative bias and illumination stress (NBIS). On the other hand, a positive voltage is applied to the gate electrode when TFT is operated at the on-state. The TFTs are operated under positive bias stress (PBS). Therefore, the reliability of TFTs under NBIS and under PBS is required for the display application. However, reliability of IGZO TFT under PBS and under NBIS has been known to be critical issues. This research focuses on investigating the degradation mechanism of IGZO TFT under PBS and under NBIS. Based on the investigated degradation mechanism, a method to improve the reliability of IGZO TFT under PBS and NBIS was proposed. This dissertation includes 8 chapters.

+) Chapter 1 is an overview on the history of display technology and of materials used for TFTs, which have been used in FPDs backplane. The reasons for high carrier mobility in amorphous IGZO comparing to that in amorphous silicon will also be explained.

+) Chapter 2 will describe the working principle of the deposition and evaluation equipments that were used in this research, such as DC-magnetron sputtering, Plasma-Enhanced Chemical Vapor Deposition (PECVD), X-ray Reflectivity Measurement (XRR), and Secondary Ion Mass Spectrometry (SIMS) Measurement, and so on.

+) In chapter 3, we will introduce our new measurement method, which we have named as Positive Gate Pulse Mode (PGPM). PGPM was used to investigate the NBIS degradation

mechanism. Due to the importance of the NBIS reliability issue in FPDs application, a number of researches relating to the NBIS degradation have been reported. Trapped holes in the gate insulator (GI), generated defects in the channel have been widely accepted as reasons for the NBIS instability in IGZO TFT.

In previous reports, TFT transfer characteristic were measured by single sweeping mode (SSM), in which the gate voltage was swept half cycle, for instance from a negative voltage to a positive voltage. However, we found that the SSM did not fully capture the NBIS degradation behaviors. Therefore, Double Sweeping Mode (DSM) was used to measure the transfer characteristics of IGZO TFT under NBIS. DSM is a transfer characteristic measurement method in which gate voltage was swept one cycle, for instance from a negative voltage to a positive voltage and reversed. By using DSM, a new NBIS degradation behavior - a positive shift in reverse curve - was observed during NBIS stress time. Threshold voltage ( $V_{th}$ ) in reverse measurement ( $V_{rev}$ ) shifted positively without subthreshold swing ( $S_s$ ) degradation. The change in  $V_{rev}$  with NBIS stress time was well fitted by a stretched-exponential equation. These results indicate that trapped electrons at the back channel interface are the reason for the positive shift in reverse curve. By using DSM, a new mechanism for the NBIS instability - the trapped electrons at the back channel interface - was found.

Using DSM, we also found that TFT hysteresis ( $V_h$ ) increased with NBIS duration. The results of our studies indicate that the trapping/detrapping of holes and the generation/stabilization of defects could be reasons for the increase in hysteresis. Therefore, a quantitative analysis effect of the trapped holes and the generated defects is necessary for finding a method to improve the NBIS reliability. In order to do that, we developed a novel measurement method, which we named Positive Gate Pulse Mode (PGPM). PGPM is a transfer characteristic measurement method in which a short positive gate pulse is applied to the TFT before every transfer characteristic measurement. Results measured by PGPM indicate that the hole trapping in the GI is the main cause of the NBIS instability in the IGZO TFT. The contribution of hysteresis induced by the trapped holes to the hysteresis was 80%. Therefore, reducing the hole trapping in the GI will significantly improve the NBIS stability of the IGZO TFT. Based on the results obtained by DSM and PGPM, a new degradation mechanism of the IGZO TFT under NBIS was proposed. Quality of the IGZO channel, of the back channel interface and of the GI

strongly affects the NBIS reliability of IGZO TFT. Therefore, the effects of channel film density and of the back channel quality on the NBIS reliability will be discussed in chapter 4, and 5, respectively. Chapter 6 will discuss the hole trapping mechanism and a driving method to improve the NBIS reliability of the IGZO TFT.

+) In chapter 4, the effect of film density of IGZO channel on the defect creation in IGZO TFT under NBIS was investigated by using PGPM. The IGZO channel was deposited by DC-magnetron sputtering at a substrate temperature of without heating, 150, 250°C. The film density of IGZO channel which was measured by X-ray reflectivity (XRR) measurement increased with deposition temperature. The PGPM was conducted to quantitative analyze the effect of IGZO deposition temperature on the trapped holes and on the generated defects. Results indicated that the generated defects in the channel can be reduced by increasing the film density of the IGZO channel. The positive shift in reversed curve was greater when the film density of the channel decreased. This result implies that the electron trapping at the back channel interface was reduced with the IGZO film density. In other words, high film density of the channel can reduce generation of the defects not only in the channel but also at the back channel interface, resulting an improvement of the NBIS reliability. However, it was also found that the hole trapping in GI was not dependent on the IGZO film density.

+) In chapter 5, we investigated the effects of back channel interface quality on the NBIS reliability. Quality of the back channel interface was varied by the PE-CVD plasma power of SiO<sub>x</sub> etching stopper (ES) deposition. The plasma power of SiO<sub>x</sub> ES deposition was varied as 40, 50 and 55 W. A positive shift in reverse curve and hysteresis induced by generated defects was smaller when the plasma power decreased. This result implies that the generation of the defects at the back channel interface and in the channel could be reduced by decreasing the plasma power of the SiO<sub>x</sub> ES deposition.

+) Chapter 6: We will present hole generation mechanism and propose a driving method to improve the NBIS reliability. As reported in chapter 3, the results obtained from PGPM indicated that hole trapping at the GI/channel interface is the main cause of the NBIS instability in IGZO TFT. A reduction in the hole trapping at the GI/channel interface should strongly improve the NBIS reliability. One way to reduce hole trapping is by increasing potential barriers to hole trapping at the GI/channel interface. However, it is difficult to evaluate the energy barrier for

hole trapping if the effects of trapped holes and generated defects on the NBIS instability were not separated. Using PGPM to separate this effect, the average effective energy barrier for hole trapping in GI was calculated to be 0.39 eV.  $\text{SiO}_x$  and  $\text{AlO}_x$  have been found to be the best GI materials to reduce hole trapping in the GI. Therefore, the hole generation mechanism was investigated in order to find another method to further reducing the hole trapping in the GI. The hole generation mechanism was classified by studying the effects of negative duration and of light intensity on the NBIS degradation behaviors. The obtained results suggest hole generation. The generated defects are unstable and act as midgap trap states for hole generation. These results suggest that a reduction of DOS existing at midgap will improve the NBIS stability. The results obtained from PGPM suggested that, the midgap trap state could be stabilized by a positive gate pulse. Therefore, the NBIS stability of the IGZO TFT could be improved by applying a positive gate pulse alternatively with a negative gate pulse. In other words, in order to improve the NBIS stability, the FPDs need to be working at high frame rate and low refresh time.

+) Chapter 7 will covers the PBS degradation mechanism and method to improve the PBS reliability. PBS reliability of IGZO TFT is not such as serious problem compared with the NBIS reliability; although the reliability of the IGZO TFT under PBS has gained the attention of many researchers. The PBS degradation mechanism has been extensively investigated. Trapped electrons at the GI and deep defects creation in the channel have been widely acknowledged as reasons for the PBS instability. The deep defect creation in IGZO TFT under PBS has been predicted by the study of the activation energy of electron trapping into and detrapping from (recovery process) the GI. However, direct evidence of the deep defect creation and the energy level of the created defects has not yet been reported. This is due to the fact that, the trapped electrons and the created deep defects induce the same degradation behavior in both transfer and C-V characteristic. In this study, the conductance measurement method was used to investigate the PBS degradation mechanism of the IGZO TFT. The conductance measurement method not only measures the density of state at the GI/channel interface but also extracts the defect properties such as capturing cross section and capturing time. This information is important to recognize the characteristics of the defects that was overlapped each other. The obtained results indicate that the stabilization of donor-like interface defects is a reason for the PBS instability. We also investigate the effects of post annealing time on the PBS stability of the IGZO TFT.

Results show that, the PBS stability increased with post annealing time. When the post annealing time increased from 1 to 5 hours, the electron trapping at the IGZO/SiO<sub>x</sub> interface was reduced. This is a reason for the PBS improvement mentioned above. However, when the post annealing time was increased to 5 hours, deep acceptor-like interface defects were detected. The defects were located just below Fermi level. This result also suggests that the PBS degradation mechanism changed from donor-like defects stabilization to deep acceptor-like defects creation.

+) Chapter 8 is conclusions of this thesis. The NBIS degradation mechanism of IGZO TFT was investigated by using the DSM and PGPM. We clarified that hole trapping in the GI, the defect generation in the TFT channel and electron trapping at the back channel interface was reasons for the NBIS instability of the IGZO TFTs. The PGPM, a new measurement method, was successfully developed to separate the effects of hole trapping and of defect generation on the NBIS instability. Results obtained from PGPM indicate that hole trapping was the main cause of the NBIS instability. By separating effects of hole trapping and of defects generation, a hole trapping energy barrier of 0.39 eV was calculated for the IGZO/SiO<sub>x</sub> interface. The electron trapping at the back channel interface and the defect generation in the channel was controlled by either the film density of the channel or the PE-CVD plasma power of the SiO<sub>x</sub> ES deposition. The generated defects were unstable electrons and act as midgap traps for hole generation. The generated defects could be stabilized by capturing electrons. Based on these results, a control algorithm of FPDs driving was also proposed to improve the NBIS stability of the IGZO TFT. An increasing frame rate and reduce refresh time of the FPDs significantly improved the NBIS stability of the IGZO TFT. Results in chapter 3, 4, 5, 6 indicate that the PGPM is an effective measurement method for investigating the degradation mechanism. The results of PGPM make a valuable contribution to the work to improve the NBIS reliability of IGZO.

The PBS degradation mechanism of IGZO TFT was also clarified by the conductance measurement method. The donor-like interface defects act as the electron trap states and were stabilized by capturing electrons. The stabilization of donor-like interface defects was the main reason for the PBS instability in the TFT. An increasing post annealing time reduced electron trapping in the GI of PE-CVD SiO<sub>x</sub>. The acceptor-like interface defects were experimentally detected by the conductance measurement method. The PBS reliability of IGZO TFT can be improved by increasing the post annealing time.

# Table of Contents

<b>Table of Contents .....</b>	<b>vi</b>
Figure captions .....	ix
<b>Chapter 1: Introduction .....</b>	<b>1</b>
1.1 Display technology .....	1
1.2 Amorphous oxide semiconductor TFTs .....	2
1.3 Single component oxide TFTs .....	2
1.4 Multicomponent oxide TFTs .....	3
1.5 Carrier transport and subgap defect in oxide semiconductor .....	6
1.6 Thesis proposal .....	8
<b>Chapter 2: TFT Fabrication and characterization.....</b>	<b>11</b>
2.1 Thin film deposition and processing .....	11
2.1.1 DC magnetron sputtering .....	11
2.1.2 Plasma-enhanced chemical vapor deposition (PE-CVD) .....	12
2.1.3 Inductively coupled plasma chemical vapor deposition (ICP-CVD) .....	14
2.1.4 Dry-Etching .....	15
2.2 Characterization techniques .....	16
2.2.1 Secondary ion mass spectroscopy (SIMS) .....	16
2.2.2 X-ray diffraction (XRD) and X-ray reflectivity (XRR) .....	17
2.2.3 Initial properties and reliability testing .....	19
2.2.4 Flat band calculation and Conductance measurement method .....	20
2.3 Summary .....	23
<b>Chapter 3: NBIS degradation mechanism of IGZO TFT .....</b>	<b>24</b>
3.1 Introduction .....	24
3.2 Experimental .....	25
3.3 Results and Discussions .....	26
3.3.1 NBIS degradation behavior .....	26
3.3.2 Trapped electrons at the back channel interface .....	30
3.3.3 Positive gate pulse measurement method .....	31
3.3.4 Effects of pulse height and pulse width on hysteresis .....	33
3.3.5 The NBIS degradation mechanism .....	34



3.4 Summary .....	35
<b>Chapter 4: Effect of channel density on the NBIS stability .....</b>	<b>37</b>
4.1 Introduction .....	37
4.2 Experimental .....	38
4.3 Results and Discussions .....	38
4.3.1 Effects of IGZO deposition temperature on the initial properties.....	38
4.3.2 Quantitative effects of IGZO deposition temperature on the hole trapping and defect generation in IGZO TFT under NBIS.....	41
4.3.3 Effect of stress temperature on the NBTIS stability of IGZO TFT .....	47
4.4 Summary .....	49
<b>Chapter 5: Effects of back channel interface on NBIS stability.....</b>	<b>50</b>
5.1 Introduction .....	50
5.2 Experimental .....	51
5.3 Results and Discussions .....	51
5.3.1 Effects of ES deposition conditions on the initial properties.....	51
5.3.2 Quantitative Effects of ES deposition conditions on NBIS stability of IGZO TFT.....	52
5.4 Summary .....	54
<b>Chapter 6: A driving method to improve the NBIS reliability.....</b>	<b>56</b>
6.1 Introduction .....	56
6.2 Experimental .....	56
6.3 Results and Discussions .....	57
6.3.1 Effects of Positive gate pulse on the NBIS stability of IGZO TFT .....	57
6.3.2 Hole generation mechanism .....	61
6.4 Summary .....	65
<b>Chapter 7: PBS degradation mechanism and method to improve the PBS reliability .....</b>	<b>66</b>
7.1 Introduction .....	66
7.2 Experimental Details .....	67
7.3 Results and Discussion.....	67
7.3.1 Effect of Post-Annealing Time on Initial Transfer Characteristic and Positive Bias Stress Stability .....	67
7.3.2 DOS of Interface defects at the initial state.....	69
7.3.3 PBS degradation mechanism of 1 hour post-annealing sample.....	73

7.3.4 PBS degradation mechanism of 5 hours post-annealing sample .....	77
7.4 Summary .....	81
<b>Chapter 8: summary .....</b>	<b>82</b>
<b>Publications and oral presentations .....</b>	<b>88</b>
<b>Reference: .....</b>	<b>90</b>

## *Figure captions*

Figure 1. 1: Evolution of transparent display market and flat panel display market [30] .....	3
Figure 1. 2: Correlation between carrier mobility of TFTs and number of pixel [31] .....	4
Figure 1. 3: Schematic orbital drawing for the carrier transport paths in (a) Silicon, (b) Oxide semiconductor. ....	7
Figure 1. 4: Schematic model of subgap DOS in a-IGZO [41] .....	8
Figure 2. 1 Schematic of DC magnetron sputtering .....	12
Figure 2. 2: Basic geometries of PE-CVD [45]. ....	14
Figure 2. 3: Schematic of ICP-CVD. ....	15
Figure 2. 4 principle of secondary ion mass spectrometry. ....	17
Figure 2. 5: Schematic of XRD measurement .....	18
Figure 2. 6: Schematic of XRR measurement .....	19
Figure 2. 7: Schematic of measurement system.....	20
Figure 2. 8: Relation between semiconductor band diagrams and interface traps; (a) flat band condition ( $V_g = V_{FB}$ ), (b) $V_g > V_{FB}$ , (c) $V_g < V_{FB}$ . ....	21
Figure 2. 9 Equivalent circuits for conductance measurement (a) metal oxide semiconductor, (b) simplified circuit, (c) measurement circuit.....	23
Figure 3. 1: The schematic of Positive gate pulse mode.....	26
Figure 3. 2: (a) Schematic cross-sectional view and (b) initial transfer characteristics of a-IGZO TFTs. ....	27
Figure 3. 3: The change in TFT transfer characteristic with NBIS duration measured by single sweeping mode (a) first time measurement ( $V_{DS} = 0.1$ V), (b) second time measurement ( $V_{DS} = 10.1$ V). ....	27
Figure 3. 4: Transfer characteristics of a-IGZO TFTs before and after (a) NBS and (b) NBIS, (c) the change of hysteresis under NBS and NBIS as a function of stress duration of $10^4$ s. ....	29
Figure 3. 5: Transfer characteristics of a-IGZO TFTs before and after NBIS (a) $V_{st} = -20$ V, and (b) $V_{st} = -40$ V.....	30
Figure 3. 6: (a) Change in transfer characteristics under NBIS with $V_{st} = -40$ V in forward measurement, (b) Transfer characteristic of TFTs without and with 1 ms - 10 V	

positive gate pulse after NBIS of $10^4$ s, the change of (c) hysteresis and (d) $S_s$ value as a function. ....	32
Figure 3. 7: The change in field-effect mobility with NBIS duration .....	33
Figure 3. 8: Transfer characteristic of TFTs after NBIS of $10^4$ s (a) without and with 1 ms pulse width and 5, 10, 15 V pulse high positive of gate pulse, (b) without and with 1 ms and 25 s pulse width and 10 V pulse high of positive gate pulse. ....	34
Figure 3. 9: Schematics band diagrams of degradation mechanism under NBIS.....	35
Figure 4. 1 Transfer characteristic of (a) TFT-1, (b) TFT-2, (c) TFT-3, (d) correlation between electron mobility, threshold voltage and IGZO deposition temperature, and (e) cross section view of IGZO-TFT. ....	40
Figure 4. 2: The SIMS profile of hydrogen, Indium, gallium and oxygen in 100nm IGZO film deposited at (a) RT, (b) 220°C. ....	41
Figure 4. 3: Transfer characteristic of (a) TFT-1, (b) TFT-2, (c) TFT-3 after $10^4$ s NBIS measured using double sweeping mode and positive gate pulse mode, and duration of hysteresis detected using double sweeping mode and positive gate pulse mode in (d) TFT-1, (e) TFT-2, (f) TFT-3 under NBIS (Inset shows dependence of $\Delta V_{\text{defect}}$ and $\Delta V_{\text{hole}}$ on IGZO deposition temperature).....	42
Figure 4. 4: The NBIS stress time dependence of subthreshold swing for different IGZO deposition temperature. ....	43
Figure 4. 5:(a) XRR data, (b) XRD spectra of IGZO thin films deposited at different temperatures. ....	46
Figure 4. 6: Transfer characteristics of TFT-3 after $10^4$ s NBITS at different temperatures (a) RT, (b) 35°C, and (c) 50°C. The durations of TFT-3 hysteresis under NBIS at difference temperatures (d) RT, (e) 35°C (Inset shows dependence of $\Delta V_{\text{defect}}$ and $\Delta V_{\text{hole}}$ on NBITS stress temperature), and (f) 50°C (Inset shows the value of $\beta$ and $\ln(\tau)$ as a function of NBITS stress temperature). ....	48
Figure 5. 2: Figure 4. 3: Transfer characteristic of (a) TFT-1, (b) TFT-2, (c) TFT-3 after $10^4$ s NBIS measured using double sweeping mode and positive gate pulse mode, and duration of hysteresis detected using double sweeping mode and positive gate pulse mode in (d) TFT-1, (e) TFT-2, (f) TFT-3 under NBIS .....	55
Figure 5. 1: Transfer characteristic of (a) TFT-1, (b) TFT-2, (c) TFT-3.....	52

Figure 5. 2: Figure 4. 3: Transfer characteristic of (a) TFT-1, (b) TFT-2, (c) TFT-3 after $10^4$ s NBIS measured using double sweeping mode and positive gate pulse mode, and duration of hysteresis detected using double sweeping mode and positive gate pulse mode in (d) TFT-1, (e) TFT-2, (f) TFT-3 under NBIS .....	55
Figure 6. 1: Fabrication process of IGZO TFTs with a $\text{SiN}_x/\text{F}/\text{SiO}_x$ gate stack layer .....	57
Figure 6. 2: Initial transfer characteristic of IGZO TFT with stack gate insulator .....	58
Figure 6. 3: Change in transfer characteristic of IGZO TFT under DC-NBIS measured by (a) single sweeping mode, and (b) positive gate pulse mode. ....	59
Figure 6. 4: Change in transfer characteristic under AC-NBIS with different gate bias condition; (a) NBIS-1, (b) NBIS-3, (c) NBIS-4, (d) NBIS-5. (e) the stress time dependence of $\Delta V_{th}$ under NBIS, (f) the $\Delta V_{th}$ at the AC-NBIS duration of $10^4$ s as a function of negative pulse width. 60	60
Figure 6. 5: The transfer characteristic of IGZO TFT measured before applying the positive gate pulse at light intensity of $0.2 \text{ mW/cm}^2$ and the DC-NBIS duration of (a) 200 s, (b) 250 s. The transfer characteristic of the IGZO TFT measured after applying the positive gate pulse at the DC-NBIS duration of (a) 200 s, (b) 250 s. ....	62
Figure 6. 6 The transfer characteristic of IGZO TFT at the DC-NBIS duration of 250 s measured before applying the positive gate pulse with a light intensity of (a) $0.1 \text{ mW/cm}^2$ , (b) $0.4 \text{ mW/cm}^2$ . The transfer characteristic of the IGZO TFT at the DC-NBIS duration of 250 s measured after applying the positive gate pulse with a light intensity of (a) $0.1 \text{ mW/cm}^2$ , (b) $0.4 \text{ mW/cm}^2$ .....	63
Figure 6. 7: (a) the defect generation mechanism, (b) the hole generation mechanism.....	65
Figure 7. 1: schematic diagram of the PBS testing and conductance measurement .....	67
Figure 7. 2: The Initial transfer characteristic of IGZO TFT of (a) sample A1 and of (b) sample A2; change in transfer characteristic ( $V_{DS} = 0.1 \text{ V}$ ) under PBS of (c) sample A1, and of (d) sample A2.....	69
Figure 7. 3: A set of $G_m/\omega$ versus $f$ curves with different applied DC gate voltage for (a) sample A1, and for (d) sample A2 at initial state; the distribution of $D_i$ as function of applied DC gate voltage for (b) sample A1, and for (e) sample A2 at initial state; the variation of $\tau_i$ as function of applied DC gate voltage for (c) sample A1, and for (f) sample A2 at initial state. ....	72
Figure 7. 4: capacitance - gate voltage curve of (a) sample A1, of (c) sample A2 and surface potential - gate voltage relationship of (b) sample A1, of (d) sample A2.....	73

Figure 7. 5: capacitance - gate voltage curve of sample A1 after (a) 1000 s PBS, (c) 5000 s PBS and surface potential - gate voltage relationship of sample A1 after (b) 1000 s PBS, (d) 5000 s PBS.....	75
Figure 7. 6: A set of $G_m/\omega$ versus $f$ curves with different applied DC gate voltage for (a) sample A1 after (a) 1000 s , (d) 5000 s PBS; the distribution of (b) $D_i$ , and (c) $\tau_i$ as function of applied DC gate voltage in sample A1 after 1000 s PBS; the distribution of (e) $D_i$ , and (f) $\tau_i$ as function of applied DC gate voltage in sample A1 after 5000 s PBS. ....	76
Figure 7. 7: capacitance - gate voltage curve of sample A2 after (a) 1000 s PBS, (c) 5000 s PBS and surface potential - gate voltage relationship of sample A2 after (b) 1000 s PBS, (d) 5000 s PBS.....	79
Figure 7. 8: A set of $G_m/\omega$ versus $f$ curves with different applied DC gate voltage for the sample A2 at PBS stress time of (a) 1000 s, and of (d) 5000 s; the distribution of (b) $D_i$ , and (c) $\tau_i$ as function of applied DC gate voltage in sample A2 after 1000 s PBS; the distribution of (e) $D_i$ , and (f) $\tau_i$ as function of applied DC gate voltage in sample A2 after 5000 s PBS; insert figure.(b) and (e) are the enlarge of the Figure. (b) and (e), respectively. ....	80

### ***1.1 Display technology***

A display is defined as an interface containing information that simulates human vision. The information can be texts, pictures, movies, and so on [1]. Nowadays, displays are everywhere and play an important part in our daily life. The earliest type of display was a mechanical type. It was invented in 1884 by the German, Paul Gottlieb Nipkow, and is known as the “Nipkow disk” [2]. The mechanical display was developed until 1931, when it was replaced by an electronic display system.

The first electronic display system was demonstrated in 1907 by Boris Rosing, a Russian inventor [3]. Rosing’s display was a primitive form of cathode ray tube displays (CRTs). It consisted of a cathode ray tube in addition to a mechanical scanner system. On December 25, 1926, Kenjiro Takayanagi, a Japanese inventor, succeeded in transmitting the Japanese character 𐤀 (i) on a Braun tube using a Nipkow disc camera [4]. CRT television (TV) was then rapidly developed. Now, CRT is a highly developed technology. The CRT has many advantages such as self-emission, wide viewing angle, good color saturation, good image quality, long lifetime, and fast response. The main disadvantages of the CRT are its bulky size heavy weight. These disadvantages limit the CRT’s potential applications. Therefore, a slimmer and lighter display was required. Flat panel displays (FPDs) satisfy these requirements. Flat panel displays are relatively thin with a display size ranging from less than 1 inch (microdisplay) to over 100 inches [5]. Several FPDs have been developed, for instance, liquid crystal display (LCD), light emitting diode (LED), plasma display panel (PDP), field emission display (FED). Each technology has its own unique properties and applications. Looking back over the history of display, display development has been strong correlated with material science. The black and white CRT was replaced by full color CRT when multilayer Red, Green, Blue phosphor was invented. The investigation of liquid crystal materials is a necessary and pre-condition for threshold development in display technology, from CRTs to LCD [6]. The LCD is usually driven by a thin film transistors (TFTs) array. The TFTs act as electrical switches to turn each picture element (pixel) “on” (light) or “off” (dark) individually. The material and technology for fabricating the TFT have a strong impact on the physical and performance properties of LCDs. Therefore, the

investigation of oxide semiconductors including InZnO, SnZnO, InGaZnO is expected to be a groundbreaking development in LCD technology [7]–[9].

### ***1.2 Amorphous oxide semiconductor TFTs***

The history of oxide TFTs began in 1964 with tin oxide TFT [10]. However, oxide TFTs have been attracting much attentions since 2003 when investigations into ZnO TFTs and especially InGaZnO TFTs were first reported [11], [12]. Compared to conventional a-Si TFTs, AOS TFTs have several advantageous properties such as transparence to visible light, high field effect mobility, controllable turn on voltage and steep subthreshold swing. Good uniformity and smooth surface at low temperature deposition of AOS thin film helps extend the potential applications for AOS TFTs, for instance in large area, transparence displays or in flexible devices. Besides the advantageous properties, AOS TFTs are also easily to fabricate into devices. Due to the fact that a-Si easily reacts with O<sub>2</sub> in air; a-Si TFTs fabrication process requires a closed system and normally with a vacuum condition. In spite of that, AOS TFTs can be fabricated in ambient pressure using an open system, for instance spin coating, chemical bath, spray pyrolysis, and mist-CVD [13]–[17]. Therefore, the fabrication costs can be significantly reduced. The oxide semiconductor materials can be clarified into single component oxide and multicomponent oxide materials.

### ***1.3 Single component oxide TFTs***

Single component oxide semiconductors are usually polycrystalline even if they are deposited at room temperature. ZnO, In<sub>2</sub>O<sub>3</sub>, SnO<sub>2</sub>, Ga<sub>2</sub>O<sub>3</sub> are some examples of single component oxide semiconductors [18]–[22]. In<sub>2</sub>O<sub>3</sub> and SnO<sub>2</sub> are not suitable for the channel of TFT because of high carrier concentration. The carrier concentration in In<sub>2</sub>O<sub>3</sub> and SnO<sub>2</sub> can be slightly modulated by limiting the O<sub>2</sub> partial pressure during either deposition or post annealing [23], [24]. The threshold voltage of the TFTs can be controlled by the thickness of the channel [25]. In spite of high carrier concentration in In<sub>2</sub>O<sub>3</sub> and SnO<sub>2</sub>, the limitation of Ga<sub>2</sub>O<sub>3</sub> is its low field effect mobility. The mobility of Ga<sub>2</sub>O<sub>3</sub> TFT is 0.05 cm<sup>2</sup>/Vs even at a deposition temperature of 550°C [22].

ZnO has been intensively studied, both for TFT applications and LED applications. Single crystalline ZnO has a bandgap of ~ 3.4 eV and mobility of ~ 200 cm<sup>2</sup>/Vs. Due to its transparence



to visible light and high carrier mobility, ZnO is a promising candidate as a channel material for TFT. Therefore, polycrystalline ZnO (poly-ZnO) is expected to replace TFT hydrogenated amorphous Silicon (a-Si) TFTs which is currently used in FPD [18], [26]. LCDs driven by ZnO-TFT arrays were demonstrated in 2006 by Kochi University of Technology [27]. OLEDs driven by ZnO-TFT arrays have also been demonstrated in 2006 by Electronics and Telecommunications Research Institute (ETRI) and LG electronics group [28]. However, ZnO TFTs have many issues that need to be addressed. Reasons for the limitations of ZnO TFTs are that ZnO is naturally formed as polycrystalline and its chemical instability. The poly-ZnO can be deposited even on an unheated substrate. The polycrystalline ZnO thin films characterize by a high surface roughness, low uniformity as well as unstable electrical properties. The chemical instability of ZnO limits the fabrication into microdevices. Those disadvantages lead to a requirement for new oxide materials, which has amorphous state, high sufficient mobility, and low deposition temperature as well. Hideo Hosono and his partners have investigated the “role” for “designing” AOS materials [29]. By using the role, multicomponent AOS materials which satisfy the requirements mentioned above have been synthesized.

#### 1.4 Multicomponent oxide TFTs

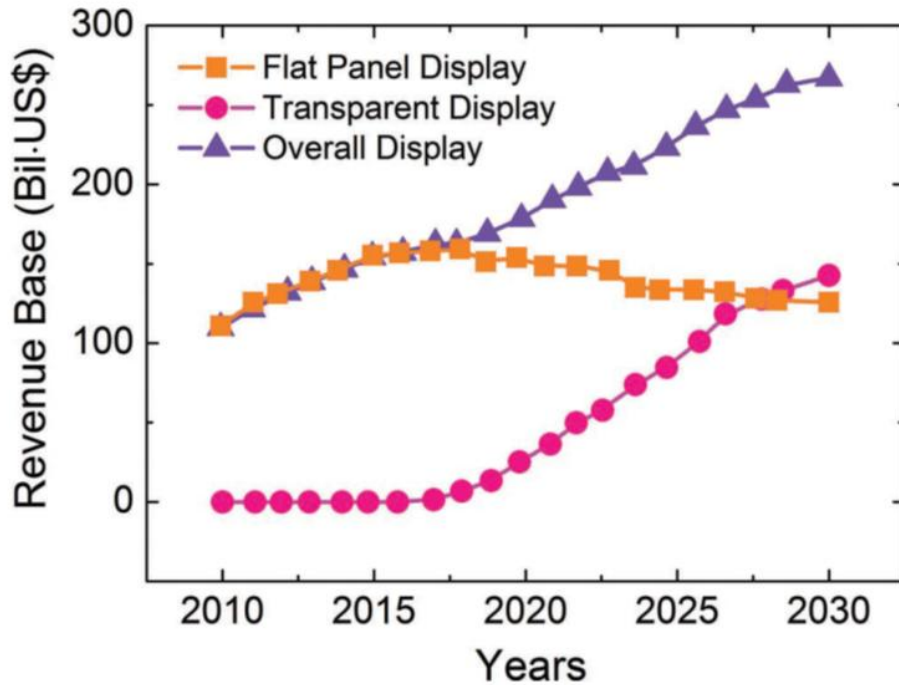


Figure 1. 1: Evolution of transparent display market and flat panel display market [30]

Method to obtain a stable amorphous oxide was investigated by considering ZnO and In<sub>2</sub>O<sub>3</sub> materials. Pure ZnO and In<sub>2</sub>O<sub>3</sub> thin film have a crystalline structure even they are deposited on unheated substrates. However, when ZnO and In<sub>2</sub>O<sub>3</sub> are mixed with a certain mixing ratio, an amorphous multicomponent oxide (InZnO) is obtained. This result suggests that an amorphous oxide semiconductor can be obtained by mixing 2 or more oxide semiconductors which have different cation charges and cation size.

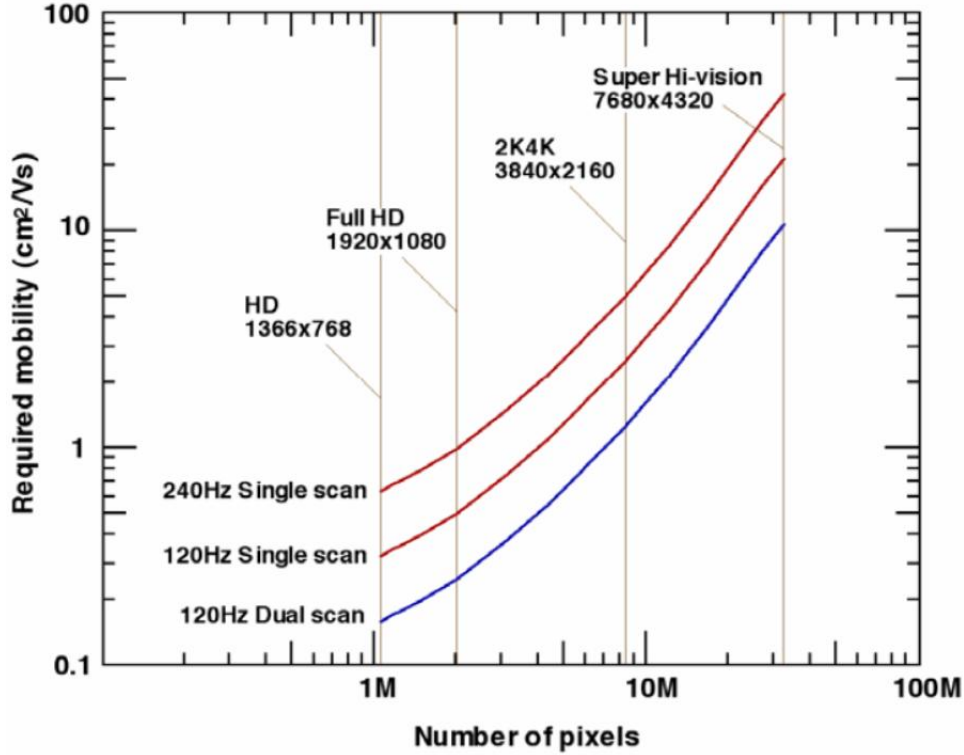


Figure 1. 2: Correlation between carrier mobility of TFTs and number of pixel [31]

There are a number of multicomponent AOS TFTs, including InZnO, InGaZnO, ZnSnO, InWO ... InSnO TFTs, with high electron mobility ( $\sim 40 \text{ cm}^2/\text{Vs}$ ) [32]. However, IZO TFTs are depletion mode devices. This is due to the fact that the carrier concentration in IZO is difficult to suppress. Ga has been doped to IZO to reduce carrier concentration. The high ionic potential and small ionic radius of  $\text{Ga}^{3+}$  is expected to increase the metal oxide bonding, resulting in the suppression of oxygen vacancy in the film [33], [34]. As expected, carrier concentration decreased from  $10^{18}$  (in IZO) to  $10^{13} \text{ cm}^{-3}$  (in IGZO) when Ga was doped to IZO [11]. The carrier mobility, and carrier concentration of IGZO are strongly affected by the element ratio between In:Ga:Zn:O. The terms InGaZnO or IGZO do not imply that the element ratio is 1:1:1:1.

Carrier concentration in IGZO thin film can be controlled either by the percentage of In or by the percentage of Ga in the film [35]. If the IGZO thin film is deposited by physical deposition methods, the carrier concentration can also be regulated by the oxygen partial pressure or by the substrate temperature [36], [37]. Among these AOS TFTs, a-IGZO TFTs have been extensively investigated. Amorphous IGZO TFTs exhibit high field effect mobility ( $10 - 20 \text{ cm}^2/\text{Vs}$ ) and on/off ratio, low off current ( $<10^{-13} \text{ A}$ ), controllable threshold voltage, steep subthreshold swing ( $\sim 0.2 \text{ V/dec}$ )[31].

Table 1. 1: A Comparison between a-Si:H; LTPS, Org-semiconductor; and IGZO technology.

Property	a-Si:H	LTPS	Org-semicon	IGZO	
Microstructure	Amorphous	Polycrystalline	polymer	Amorphous	
Uniformity	Good	Poor	???	Fair	
Process complexity	Low	High	Low	Low	
Scalability	10G	4G	Good	8G	
Stability	Poor	Good	Low (in air)	Bias stress	NBIS
Mobility ( $\text{cm}^2\text{V}^{-1}\text{s}^{-1}$ )	$< 1$	50-100	0.1-10	10-30	
On/of ratio	$10^6$	$10^7$	$10^7$	$10^9$	
Touch panel influence	high	high	high	Low	
Power consumption	high	high	high	Low	
Normal		Good		The best	

From the view point of display application, a-Si TFTs are usually used in FPD backplane because of low cost, well developed technology, good uniformity and suitability for fabrication on glass substrate. However, the low mobility of a-Si ( $\sim 1 \text{ cm}^2/\text{Vs}$ ) limits the size and the pixel density of display. The correlation between field effect mobility of the TFT and number of pixels is shown in figure 1.2 [31]. Low bias stress reliability is also other disadvantage of a-Si TFTs. It reduces the lifetime of LCD and brightness of OLED due to the shift in threshold voltage. The disadvantages of a-Si TFTs can be overcome by low temperature polysilicon (LTPS) TFTs. LTPS TFTs have high field effect mobility ( $\sim 100 \text{ cm}^2/\text{Vs}$ ) and high stability. However, LTPS technology also has some drawbacks. LTPS is crystallized from a-Si by excimer laser annealing. Using laser annealing increases fabrication cost and reduces scalability. In addition, the polycrystalline also reduces the uniformity of TFT properties due to the grain boundary problem.

Amorphous IGZO has been designed to overcome those limitations. Amorphous IGZO TFTs have many advantages over a-Si and LTPS TFTs. Due to low deposition temperature and large bandgap, a-IGZO TFTs are promising candidate for flexible and transparent displays. Transparent, flexible and bendable displays are expected to be the next groundbreaking in display technology. The research from displaybank predicted that the flat panel display market will be saturated and that of transparent displays will rapidly expand in around 2020. The data is shown in figure 1.1 [30]. Due to high electron mobility, the dimensions of a-IGZO TFT can be decreased resulting in increased pixel density on the display. As a consequence of the smaller TFT, the influence of TFTs operation on the touch signal in the touch screen display is also reduced. The low off current in a-IGZO TFT reduces the refresh time, resulting in reduced energy consumption in an IGZO display. Detailed comparisons between a-IGZO, a-Si, low temperature polysilicon (LTPS) and organic TFTs are shown in table 1.1.

### ***1.5 Carrier transport and subgap defect in oxide semiconductor.***

The correlation between bandgap and chemical bonding in semiconductor material has been used to explain the origin of high electron mobility in a-IGZO. When 2 atoms make a bond, the orbitals of 2 atoms overlap. Electrons will locate at the lowest energy level (occupied orbitals) and are called bonding orbitals. Other unoccupied orbitals locate at higher energy level and are called anti-bonding orbitals. The energy difference between bonding orbitals and antibonding orbitals corresponds to the bandgap in a semiconductor. The bandgap and carrier mobility of semiconductors depends on the bonding length and overlapping spatial volume of the 2 orbitals. In Si materials, Si atoms bond to each other by a  $\sigma$  bonding, which is formed by the overlapping  $sp^3$  hybrid orbital of Si. Due to the tetrahedral dumbbell shape of the  $sp^3$  hybrid orbital, the overlapping spatial volume between 2 bonded orbitals is highest when the bond angle is  $180^\circ$ . Any fluctuation in the bond angle dramatically reduces the overlapping spatial volume. In an amorphous state, Si-Si bond angle fluctuates with a large aptitude, so some Si-Si bonds cannot be formed, as shown in figure 1.3(a). The overlapping spatial volume decreases dramatically, so the conducting path cannot be achieved. The carrier transport in amorphous Si is limited by hopping mechanism. As a result, the carrier mobility is also drastically decreased. In spite of the  $sp^3 - sp^3$  bond in Si,

the bonds in oxide semiconductor are ionic chemical bonds and formed by an overlap between p orbital in oxygen atom and s orbital in heavy metal. Due to the spherical shape of s orbitals, the overlapping spatial volume of an s – p bond is not strongly dependant on the bonding angle. Besides that, the large s orbitals of heavy metals can also themselves overlap each other to form a conducting path, as shown in figure 1.3(b). Therefore, the conducting path can be achieved even in amorphous oxide semiconductor. As a result, the carrier mobility in amorphous oxide semiconductor is much higher than that in amorphous silicon. However, due to the high density of weak bonding, and undercoordinated atoms in amorphous state, the density of state (DOS) of subgap states in IGZO is high.

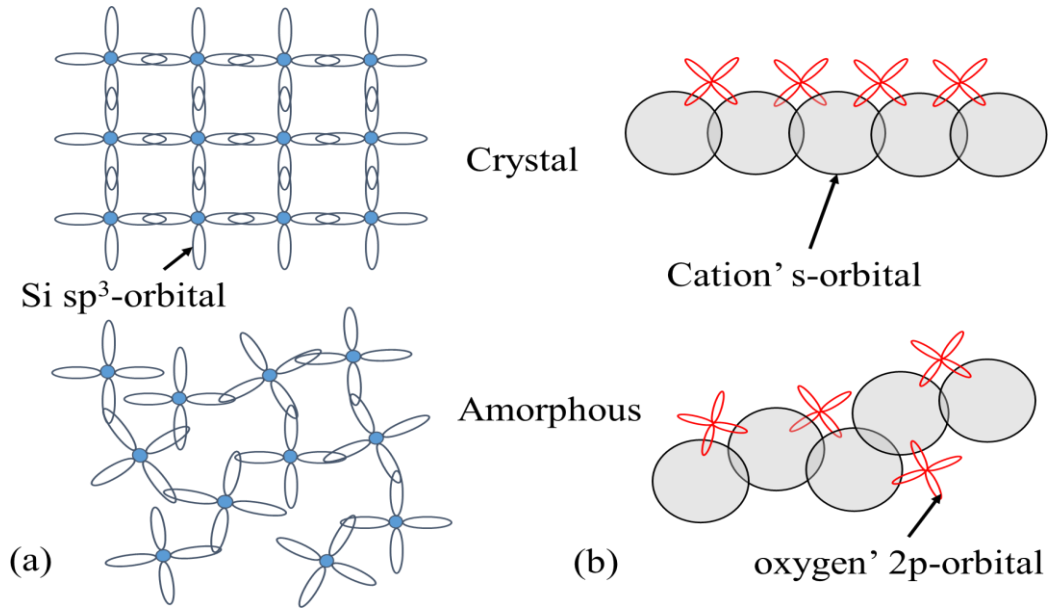


Figure 1. 3: Schematic orbital drawing for the carrier transport paths in (a) Silicon, (b) Oxide semiconductor.

The subgap defects in a-IGZO are distributed at many energy levels. A schematic model of density of state of subgap in a-IGZO is shown in figure 1.4. A deep state related with oxygen vacancy located at the level  $\sim 1.5$  eV far from conduction band minimum ( $E_C$ ). The term “oxygen vacancy” is used as a reference from a study in ZnO crystalline or IGZO crystalline. However, it is difficult to determine or to define a “vacancy” in amorphous state. In 2014, S. Sallis et. al. proved that the origin of the deep subgap feature in a-IGZO is not

due to oxygen vacancies. The local coordination of the oxygen states in a-IGZO is the origin of the deep subgap defects [38]. Several defects states located  $\sim 0.1 - 0.15$  eV from  $E_C$ . IGZO has a conducting path located about 0.03-0.1 eV above  $E_C$ . Therefore, when carrier concentration was increased, in spite of conventional semiconductor, mobility in IGZO also increased [39], [40]. Due to the high DOS of subgap states and of subgap traps defects, the reliability of IGZO TFTs under positive bias stress (PBS) and especially negative bias and illumination stress (NBIS) remain critical issues.

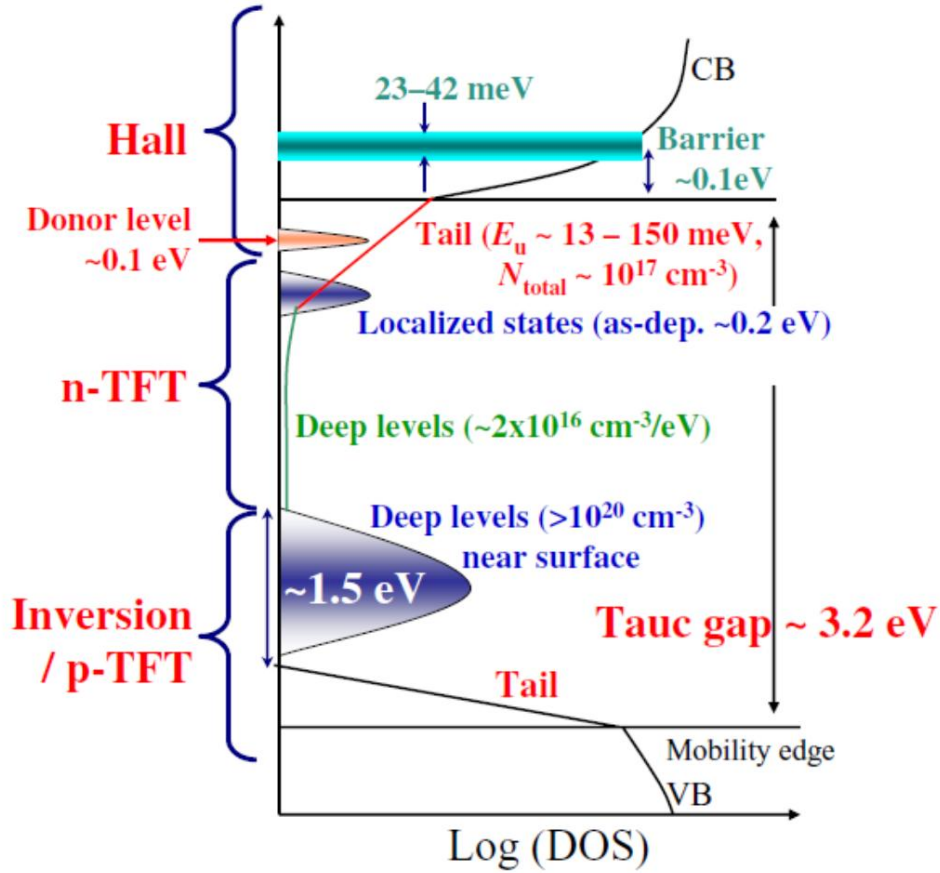


Figure 1. 4: Schematic model of subgap DOS in a-IGZO [41]

## 1.6 Thesis proposal

The goals of this research are to investigate the degradation mechanism of IGZO TFTs under NBIS and under PBS. Based on the PBS and NBIS degradation mechanism, a method for

improving the stability of IGZO TFTs under PBS and under NBIS will be suggested. In order to meet its goals, the research will be presented in 8 chapters. Chapter 1 is an overview the history of display technology and of materials for TFTs which have been used in FPD backplanes. The advantages and disadvantages of each material will also be compared. We also explain the reasons for high carrier mobility in amorphous oxide semiconductor compared to that in amorphous silicon. In chapter 2, the working principles of fabrication and analysis devices will be briefly introduced. From chapter 3 to chapter 7, the breakdown of each chapter is as follows: we first summarize other published works to give an overview on each research topic; this is followed by an experiment, results and discussion; each chapter will be concluded with a short summary. In chapter 3, NBIS degradation was investigated using our developed measurement method, which we named Positive Gate Pulse Mode (PGPM). The PGPM is a transfer characteristic measurement, in which a positive gate pulse is applied to the TFTs prior to the transfer characteristic measurement. We found that the created defects are unstable, and can be neutralized by capturing electrons. The PGPM was also found to be a measurement method that can separate effect of trapped holes and of created defects on the NBIS stability of IGZO TFTs. The degradation mechanism of IGZO TFTs under NBIS will be discussed in detail, based on the results measured by PGPM and double sweeping mode (DSM). Based on the result of DSM, the trapped electrons at a back channel interface were found to be another reason for NBIS instability in the TFTs. Chapters 4 and 5 will respectively present the effects of etching stopper (ES) and channel deposition condition on the NBIS stability of IGZO TFTs. The results indicate that bad formation of the back channel interface and low film density in the channel reduces the stability of IGZO TFT under NBIS. This result confirms the suggestion in chapter 3 that the trapped electron at the back channel interface is one reason for the NBIS stability. The influence of etching stopper deposition and of channel deposition condition on the NBIS reliability also implies that the defects are mainly generated at the back channel interface. The quantitative effect of deposition temperature of IGZO on hole trapping and defect generation by PGPM indicates that the trapped holes at the gate insulator are the main cause of the NBIS instability. This result suggests that reducing trapped holes at the GI will have a great impact on improving NBIS reliability. Therefore, understanding the hole generation mechanism is essential to the work on improving NBIS stability. The degradation mechanism and the driving method to improve the NBIS stability in IGZO TFT are presented in chapter 6. By studying the effects of

AC-NBIS and of the incident light intensity on the NBIS degradation behavior, we found that the created defects act not only as the donor-like defects but also as the midgap trap states for hole generation. The created defects were also unstable, as mentioned in chapter 3. Those results suggest that the NBIS stability of IGZO TFT can be significantly improved by increasing the working frame rate and reducing the refresh time of the FPD. Besides the NBIS instability, the PBS instability of IGZO TFTs also is known as a remained issue. The PBS degradation mechanism will be illustrated in chapter 7. The conductance measurement method was used to investigate the PBS degradation. The conductance measurement can not only estimate the DOS of interface defects but also provide the trap time constant of the defects. The trap time constant is an important parameter to distinguish defects that have overlap energy distribution. The results indicate that the stabilization of donor-like defects is a cause of PBS instability. A generated deep acceptor-like defects in the TFT under PBS is experimentally detected. The influences of post annealing time on the PBS degradation mechanism will also be presented. Increasing post annealing time improve the PBS stability of IGZO TFTs. We also found that electron trapping resistivity of PECVD can be improved by increasing post annealing time. In 5 hours annealing sample, the creation of deep acceptor-like defects was identified as the main cause of the PBS instability. The deep acceptor-like defects were located just below Fermi level. The PBS degradation changed from donor-like defects stabilization to deep acceptor creation when the post annealing time was increased from 1 to 5 hours. All of this work will be summarized in chapter 8.



This chapter will cover the working principles of the deposition and evaluation equipment, which were used in this thesis. DC magnetron sputtering was used to deposit the Cr gate electrode, the IGZO channel and ITO source and drain electrode. Plasma-Enhanced Chemical Vapor Deposition was used to form  $\text{SiO}_x$  thin films, which acted as gate insulator, etching stopper and passivation layer. Inductively Coupled Plasma-Enhanced Chemical Vapor Deposition (ICP-CVD) was also used to grow  $\text{SiO}_x\text{:F}$ . Thin film evaluation equipments, for instance X-ray reflectivity measurement (XRR), X-Ray diffraction (XRD), and Secondary ion mass spectrometry (SIMS) measurement, were used to characterize the TFT channel properties. We also discuss electrical characterization and reliability evaluation methods.

### ***2.1 Thin film deposition and processing***

#### *2.1.1 DC magnetron sputtering*

A sputtering event is started by the first collision between energetic particles and surface atoms of a target, followed by the second and third collisions between the target surface atoms. As a result, a plume of material is released [42]. The source of the incident particles is an ion type that can be introduced either by a local plasma or a separate ion beam source. Two sputtering mechanisms have been proposed: thermal-vaporization and momentum-transfer. The thermal-vaporization mechanism was suggested by Hoppel in 1926, and the momentum-transfer model was proposed by Stark in 1908. At present a collision cascade in the surface layers of a target is believed to be the reason for the sputtering. Depending on the method used to generate the incident particles, sputtering can be classified as DC Diode sputtering, magnetron sputtering, RF, MF and pulse sputtering, ion beam deposition and so on. Among them, magnetron sputtering has been used in a wide range of industrial coatings [43]. The magnetron sputtering can also be divided into balanced and unbalanced magnetron sputtering, depending on magnetic flux. The DC balanced magnetron sputtering (conventional magnetron sputtering) was used in this thesis to deposit Cr gate electrodes, InGaZnO channel and InSnO (ITO) source and drain electrodes.

Schematic of a balanced magnetron sputtering is represented in figure 2.1. When a voltage ( $\sim 100$  V/cm) is applied between the target and the substrate holder, any free electron or ionized gas is accelerated by the applied electric field. This accelerated charge reaches a high enough energy level and starts to ionize other gas atoms via collision. With conventional sputtering, the target acts as a cathode and can be attacked by energetic ions to removing target atoms. The removed target atoms could then be deposited in the substrate. When the target is bombarded by energetic ions, besides releasing target atoms, the secondary electron is also emitted. These electrons sustain the discharge process and play an important role in maintaining the plasma. The magnet has been introduced to keep the secondary electron in the vicinity of the target. Consequently, the probability of an electron-atom collision will increase. Therefore magnetron sputtering could be operated at a working pressure lower than with a non-magnetic one. The deposition rate of magnetron sputtering is also higher.

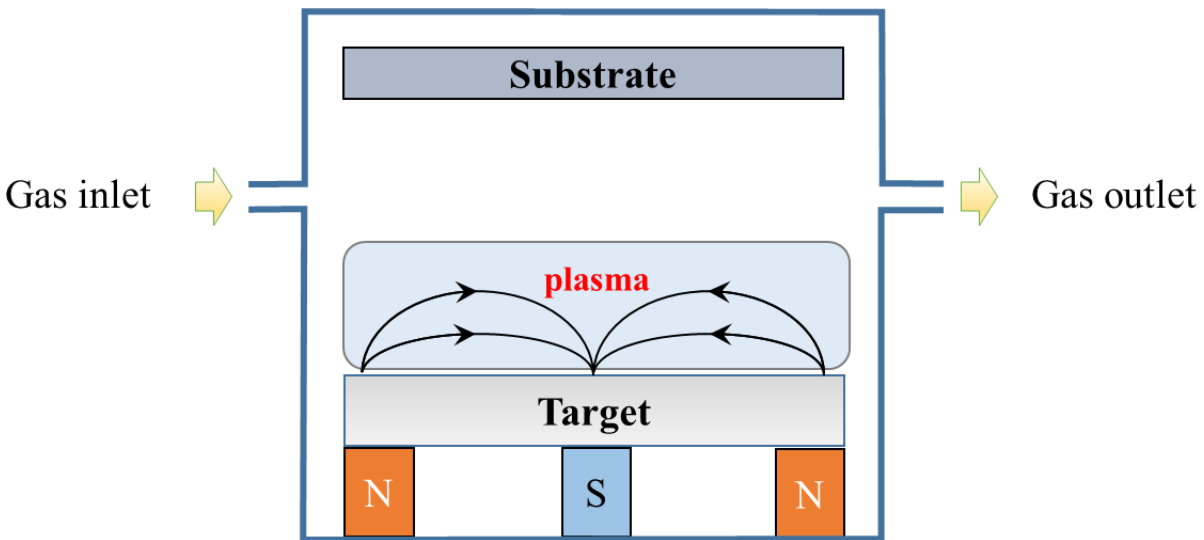


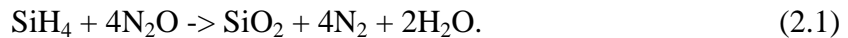
Figure 2. 1 Schematic of DC magnetron sputtering

### 2.1.2 Plasma-enhanced chemical vapor deposition (PE-CVD)

Chemical Vapor Deposition (CVD) has become an extremely popular deposition method. CVD can be used for a wide range of materials from metals, semiconductors to insulators. In general, CVD involves the formation of a thin solid film by chemical reaction of vapor phase reactants [44]. CVD is a deposition method which involves (but is not limited to) many steps

such as (1) transport of the precursors to the reactor, (2) formation of daughter molecules from these precursors, (3) diffusion of the reactants to the substrate surface, (4) reactions at the surface to form a film or nano-structure, (5) desorption of unwanted products, (6) diffusion of the unwanted products out of the substrate surface, (7) transport of the unwanted products through outlet [45]. The CVD techniques usually use precursors in the gas phase. When the gas is introduced to the reactor, it diffuses to the substrate and reactions occur to form a thin film or nano-structures. The reactions are driven in many ways, for instance by heat, by photon or by plasma [46], [47]. In many applications, a very low deposition temperature is required. Therefore, both heat and plasma are used to assist the reaction in PE-CVD to reduce the reaction temperature of a precursor. The PE-CVD that was used to deposit  $\text{SiO}_x$  is a capacitively coupled radio-frequency (RF) discharge. Plasma in the reactor is generated between 2 parallel electrodes. When a RF frequency (of 13.56 MHz) is applied between 2 electrodes the ions with a high mass cannot follow the electromagnetic field whereas the electrons with low mass can. The electrons absorb almost all the electromagnetic energy. Since electrons have higher mobility than ions, the electrons easily reach the electrodes and form a potential between electrode and the plasma edge. This potential accelerates the ions and slows down electrons resulting in a balancing out of the fluxes of positive and negative particles to the electrodes. Due to ion bombardment, surface substrate has high surface potential. This leads to the chemical reaction.

In this thesis,  $\text{SiO}_x$  thin films were deposited by PE-CVD method. A schematic of the PE-CVD used in this thesis is depicted in figure 2.2. The silane ( $\text{SiH}_4$ ) and nitrous oxide ( $\text{N}_2\text{O}$ ) were used as gas sources and  $\text{N}_2$  was used as the reaction environment. The reaction to form  $\text{SiO}_2$  has many steps and intermediate products [48], [49]. The reaction between  $\text{SiH}_4$  and  $\text{N}_2\text{O}$  to form  $\text{SiO}_2$  is illustrated as follows:



Reaction 2.1 only describes the final products of the reaction. The quality of  $\text{SiO}_x$  is influenced by many factors [50]. In this thesis, a  $\text{SiO}_x$  gate insulator was deposited at the substrate temperature of  $350^\circ\text{C}$  and a deposition temperature of  $170^\circ\text{C}$  was used for  $\text{SiO}_x$  etching stopper and passivation layer.

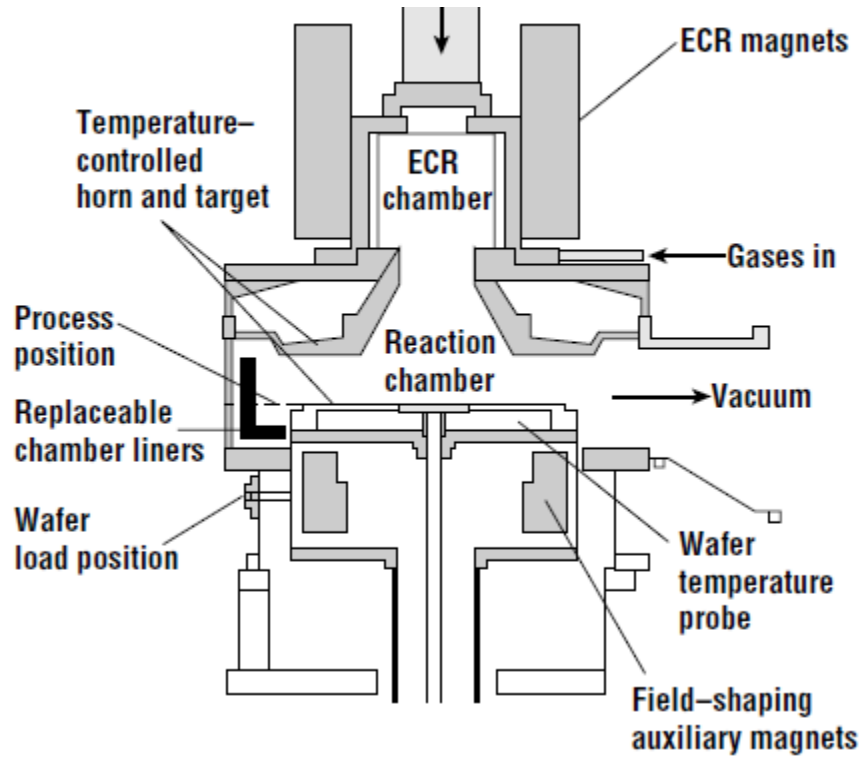


Figure 2. 2: Basic geometries of PE-CVD [45].

### 2.1.3 Inductively coupled plasma chemical vapor deposition (ICP-CVD)

Unlike the direct generated plasma in the PECVD that was presented subsection 2.1.2, the plasma in ICP-CVD is a remote plasma. The schematic of ICP-CVD is shown in figure 2.3. When an RF current is applied to the coil, an electromagnetic oscillation is generated in the coil and this is followed by generation of electric field oscillation. It heats electrons and ionizes the gas molecules. As a result, plasma is generated. Due to the plasma generation mechanism, no potential drops occur, therefore ICP does not require a high applied voltage. The ICP can generate plasma more efficiently than the capacitively coupled plasma. As a result, the inductive coupled plasma allows the system to operate at low pressure with high density plasma and little ion bombardment of the substrate surface. The ion bombardment can be easily modified by the RF chuck power without effecting the plasma density. Besides having some advantages, such as simplicity, flexibility in design, high density plasma, high efficiency, and so on, ICP-CVD also has some disadvantages - for instance dispersion of heat. During ICP CVD operation, a high current passes through and heats up the coil. Cooling the coil without creating an electrical short is a challenge. When ICP CVD working under high pressure, the plasma power will be mainly

distributed close to the coil; when this effect combines with the heat effect, the insulating wall could be compromised.

In this thesis, SiN<sub>x</sub>:F was deposited using ICP-CVD with SiF<sub>4</sub> and N<sub>2</sub> as the precursors. The reaction may have many stages but the simplest reaction can be described as follow:

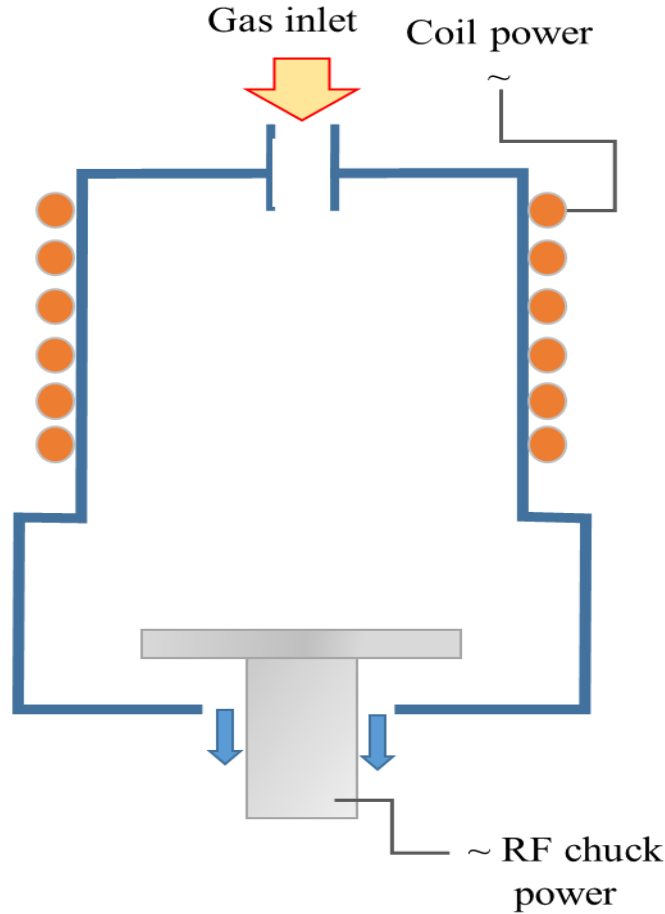


Figure 2. 3: Schematic of ICP-CVD.

#### 2.1.4 Dry-Etching

Depending on the plasma generation method that is used, dry etching can be clarified into many classes. In this thesis, an ICP-reactive ion etching (ICP-RIE) system was used to etch SiO<sub>x</sub> and IGZO. The working principle of ICP-RIE and ICP-CVD is almost the same. The main difference between them is that the gas source will react with the substrate in ICP-RIE. When the

etching gas is introduced into ICP-RIE, it will be ionized and become highly chemically reactive. Under an electric field induced by DC chuck bias, the ions bombard the substrate, chemical reaction occurs and the substrate is etched. Due to this bombardment, the substrate will be heated up. Therefore, a substrate cooling system is needed. In this work, IGZO and  $\text{SiO}_x$  will be etched by  $\text{CHF}_3$  [51].

## **2.2 Characterization techniques**

### **2.2.1 Secondary ion mass spectroscopy (SIMS)**

SIMS is a technique used for surface analysis. The working principle of SIMS is depicted in figure 2.4. When primary ions bombard the sample at the typical energies of 10-30 keV, secondary particles are released due to a sputtering process (see 2.2.1). The secondary particles can be an ion type (positive or negative charge) of atom or molecule. The ion type particles can be extracted by an electric field and then detected by mass analyzer. The SIMS can be clarified into conventional double focus (DF-SIMS) or time of flight (TOF-SIMS) depending on whether the mass analyzer is a magnetic type or a quadrupole type [52], [53]. The DF-SIMS use double focus magnetic mass spectrometers to separate the particles.

A double focus magnetic mass analyzer uses electrostatic and magnetic sector fields to separate the particles. When the secondary ion particles enter the electrostatic field, they will be forced by electrostatic forces. The radius of the particle orbit in the electrostatic field is proportional to  $mv^2/qE$ . Where  $m$ ,  $q$  and  $v$  are mass, charge and velocity of the particle respectively. Therefore, the electrostatic sector field allows us to select the particles that have the same kinetic per charge  $mv^2/2q$ . The selected particles then enter the magnetic sector field. In this magnetic field, the particles will be forced by a magnetic force. The magnetic force is dependent on the velocity of particles. Therefore, after exiting the magnetic force, the secondary ions are dispersed according to their mass/charge ratio. As a result of the electrostatic and magnetic sector fields, the secondary ions can be separated depending on their mass to charge ratio regardless of their energy.

A time of flight mass analyzer separates the ions by flight time. The velocity of an ion with a given kinetic energy depends on its mass. The secondary ion particles are accelerated in an electric field. After reaching the detector, the secondary particles are reflected by a reflector. Ions

that have higher energy will penetrate deeper in the reflector and therefore are delayed compared to those having lower energy [53]. By detecting the secondary particles at different times, the deep profile can be obtained by SIMS measurement.

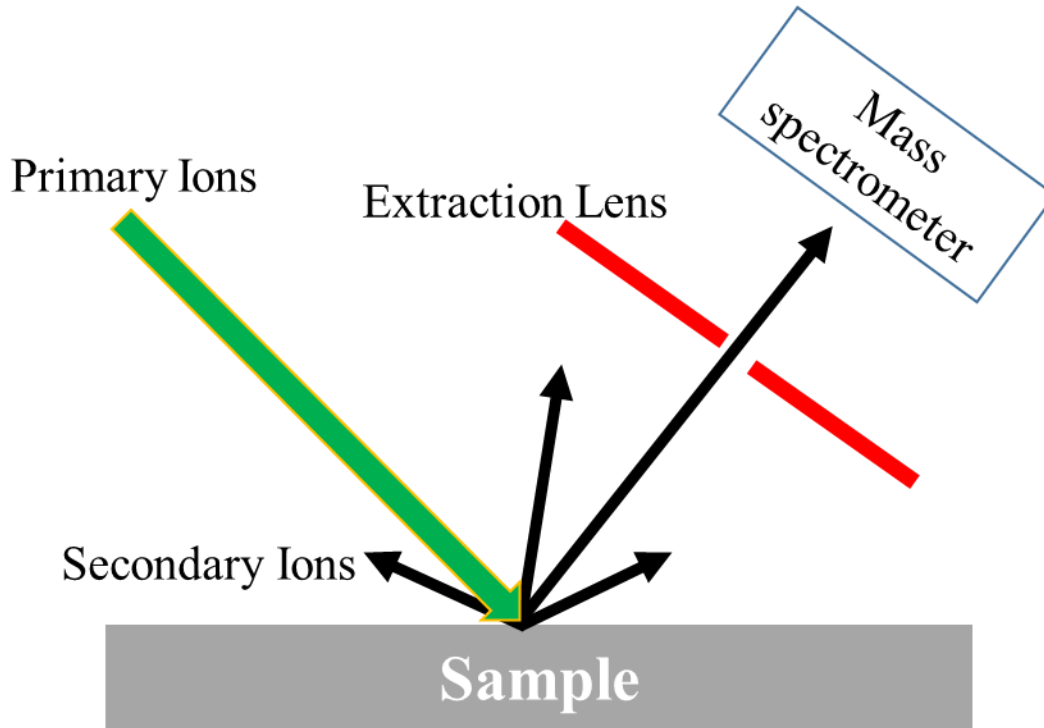


Figure 2. 4 principle of secondary ion mass spectrometry.

### 2.2.2 X-ray diffraction (XRD) and X-ray reflectivity (XRR)

X-ray diffraction (XRD) is a measurement method that is used to obtain structure information of solid materials. XRD is the most powerful method for characterizing the crystal structure of ceramics, metals, intermetallics, minerals, inorganic compound and so on [54]. The interference of the diffracted X-ray is the working principle of XRD. Figure 2.5 illustrates the working principle of XRD measurement. When an X-ray beam irradiates a sample at the incident angle of  $\theta$ , the beam will be reflected by atoms in the atomic plane. The reflected beam reflected from different atoms will have different phase. They interfere with each other following Bragg' Law. If the phase difference of the reflected waves arrives within less than one half wave-length of each other, then all reflected amplitudes will build up together. Otherwise, the reflected amplitudes will suppress each other. The correlation between the lattice constancy ( $d$ ), X-ray wave-length ( $\lambda$ ), and the incident angle ( $\theta$ ) is shown in equation 2.3:

$$2d \sin\theta = n\lambda \quad (2.3).$$

Where  $n$  is an integer number and called as the order of reflection [55]. In the XRD measurement, experiment  $\lambda$  and  $\theta$  are known values. Therefore,  $d/n$  can be calculated, so that the lattice constancy can be calculated from XRD spectrum. If the sample is in an amorphous state, the atoms in the sample are randomly distributed. As a consequence, no peak is obtained in the XRD spectrum. There are a number of XRD measurement methods, for instance in plane, out of plane... In this thesis, the  $\theta/2\theta$  XRD measurement with a Cu Ka source (18 kW) was used [56].

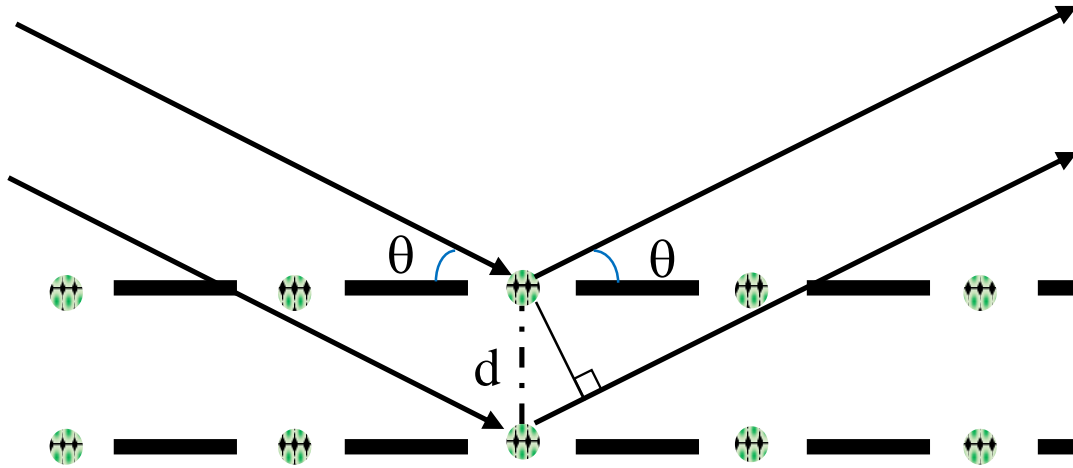


Figure 2. 5: Schematic of XRD measurement

The XRR measurement method includes monitoring the intensity of the reflected X-ray beam. The XRR measurement can be used to study a single crystalline, polycrystalline or amorphous material. It can evaluate surface roughness, film density, film thickness (from several to 1000 nm) and so on [57]. An X-ray beam with a wave length of  $\lambda$  irradiate a sample at the angle of  $\omega$  and the reflected intensity at the angle of  $2\theta$  is recorded by a detector D. Figure 2.6 represents specular reflection where the condition  $\omega = 2\theta/2$  is satisfied. Therefore the operation mode is called as  $\theta/2\theta$  mode in which the incident angle is equal to half of the angle of diffraction. The reflection at the surface and interface is due to the different reflectivity indexes or different electron density in different layers. When the incident angle is below the critical angle  $\theta_c$ , total external reflection occurs. Thin film density can be extracted from the  $\theta_c$ . The period of the interface fringes is related to the thickness of the film. On the other hand, the intensity fall in the XRR spectrum is correlated to the surface roughness [57].



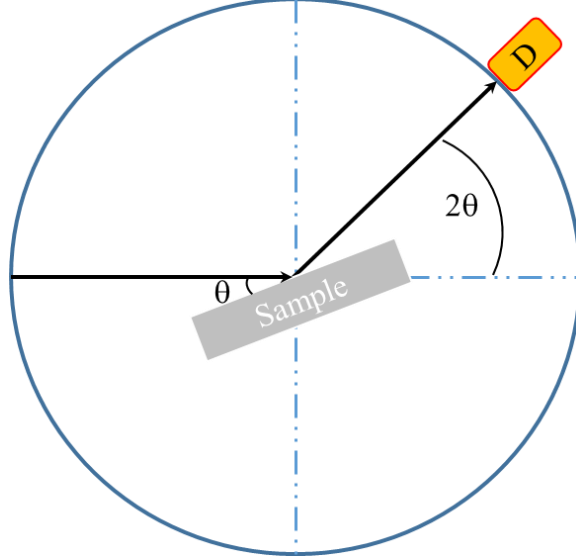


Figure 2. 6: Schematic of XRR measurement

### 2.2.3 Initial properties and reliability testing

The electrical properties and reliability testing are conducted in a shielding box. Figure 2.7 illustrates the measurement system that was used in this work. Electrical properties and reliability were evaluated using an Agilent 4155C semiconductor parameter analyzer.

The initial properties of TFT were measured using a double sweeping mode in dark. Drain voltage was set at 0.1 and 10.1 V. Gate voltage was changed from -10 to 20 V with a step of 0.2 V. Field effect mobility in linear and saturation regimes was calculated using the following formula [58]:

$$I_D^{lin} = -\mu_{lin} C_G \frac{W}{L} (V_{GS} - V_{Tlin}) V_{DS} \quad (2.4)$$

$$I_D^{sat} = -\mu_{sat} C_G \frac{W}{2L} (V_{GS} - V_{Tsat})^2 \quad (2.5)$$

Where  $C_G$  is gate insulator capacitor;  $V_{GS}$  and  $V_{DS}$  are gate-source and drain-source voltage, respectively;  $W$  and  $L$  are channel width and channel length, respectively;  $I_D^{lin}$ ,  $\mu_{lin}$ ,  $V_{Tlin}$  are drain current, field effect mobility, threshold voltage in the linear regime, respectively; and  $I_D^{sat}$ ,  $\mu_{sat}$ ,  $V_{Tsat}$  are drain current, field effect mobility, threshold voltage in the saturation regime, respectively.

A Xe lamp was used as a light source. A monochromator was used to select a monochromatic light from Xe lamp. During NBIS testing, a blue light with a wavelength of 460 nm and full width half maximum (FWHM) of 10 nm was used. The power density of stress light and gate bias stress was varied depending on the purpose of each experiment. The stress light was temporarily turned off during the transfer characteristic measurement.

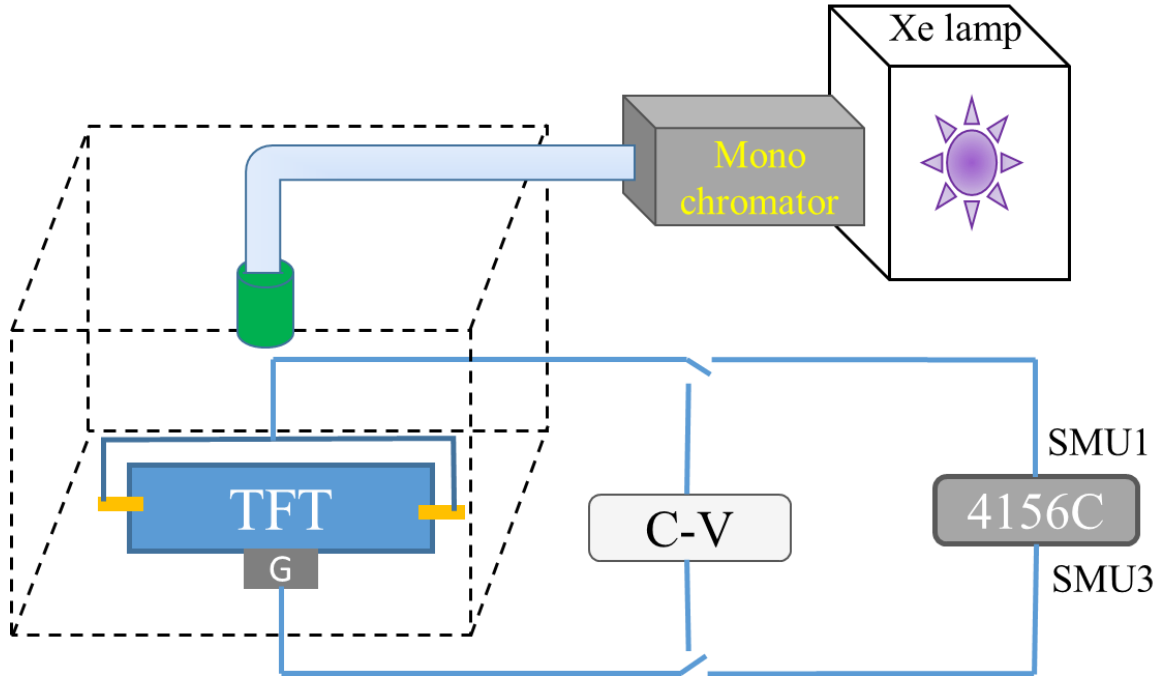


Figure 2. 7: Schematic of measurement system

#### 2.2.4 Flat band calculation and Conductance measurement method

Flat band voltage ( $V_{FB}$ ) is defined as the applied gate voltage where there is no band bending in the semiconductor and, as a result, zero net space charge in this region [59]. Flat band voltage depends on the work function between metal and semiconductor ( $\phi_{ms}$ ), the fixed charges ( $Q_f$ ) which are located very close to semiconductor/insulator interface, the net of mobile charges per unit area at the interface ( $Q_m$ ), and oxide trapped charges per unit area at the interface ( $Q_{ot}$ ). The following equation describes the relationship between flat band and  $\phi_{ms}$ ,  $Q_f$ ,  $Q_m$ ,  $Q_{ot}$ .

$$V_{FB} = \phi_{ms} - (Q_f + Q_m + Q_{ot})/C_{ox}. \quad (2.6)$$

Where  $C_{ox}$  is the gate insulator capacitor [58].  $V_{FB}$  is important in order to determine the energy level of the subgap defects. There are several methods to determine the flat-band voltage.

One method that  $V_{FB}$  can be obtained is by comparing the experimental CV curve and the theoretical curve. However, it is difficult to simulate the theoretical curve in oxide semiconductor due to its complicated doping profile. Therefore, in this work we determine the flat band voltage by plotting  $(1/C^2 - 1/C_{ox}^2)$  versus  $V$  curve. The flat band is determined as the interception of the curve with  $V$ -axis [60]. The surface potential ( $\psi_s$ ) was calculated using the equation [61], [62]:

$$\psi_s = \int_{V_{FB}}^{V_G} \left(1 - \frac{C_G}{C_{ox}}\right) dV_G \quad (2.7)$$

We investigate the PBS degradation mechanism by studying the variation in the interface trapped charge in the IGZO TFT with the PBS duration. The interface traps are donor-like or acceptor-like behavior. A donor-like interface trap is a positive charge when it locates above Fermi level; and a neutral state by capture electron when it located below Fermi level. On the other hand, an acceptor-like interface trap is a neutral state when it is located above Fermi level; and is a negative charge when it located below Fermi level. A band diagram illustrating the effect of Fermi level on the state of interface trap is shown in figure 2.8. Figure 2.8(a) shows the interface trap at the flat band condition. Figures 2.8(b) and 2.8(c) show the influence of Fermi level on the charge state of interface traps.

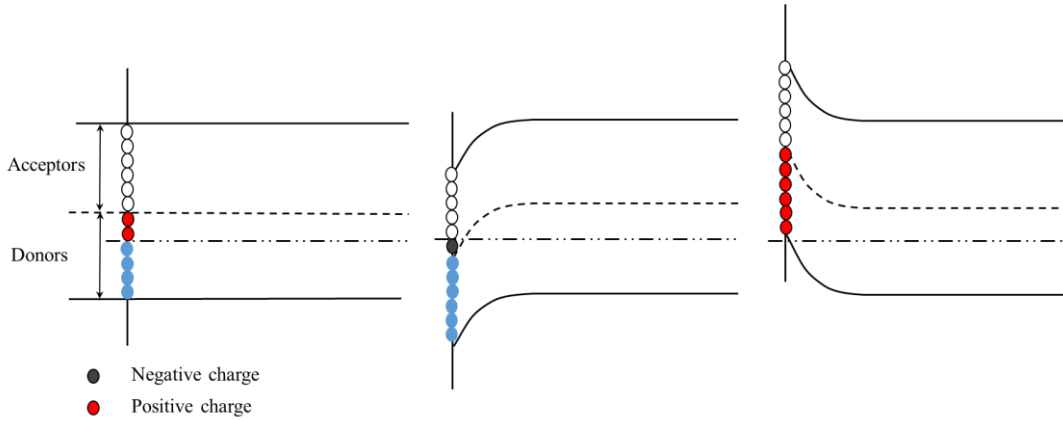


Figure 2. 8: Relation between semiconductor band diagrams and interface traps; (a) flat band condition ( $V_g = V_{FB}$ ), (b)  $V_g > V_{FB}$ , (c)  $V_g < V_{FB}$ .

Several methods can be used to evaluate the interface trap states, including low frequency (quasi-static), high frequency (Terman, Gray-Brown method), conductance, charge pumping,

DC-IV method and so on [60], [63]. The conductance method was introduced in 1965 by Nicollian [64] and is regarded as one of the most sensitive methods to determine the interface trap state ( $D_i$ ). The conductance method evaluate the  $D_i$  by measuring the equivalent parallel conductance ( $G_p$ ) of a metal oxide semiconductor as a function of bias and frequency. The conductance method can be used to determine the  $D_i$  in the depletion and weak inversion region. The equivalent circuit of an MOS structure for conductance measurement is illustrated in figure 2.9(a). It involves oxide capacitance ( $C_{ox}$ ), semiconductor capacitance ( $C_s$ ), interface trap capacitance ( $C_{it}$ ) and resistance ( $R_{it}$ ) of capture-emission of carriers due to  $D_i$ . Figure 2.9(b) shows an equivalent of circuit 2.9(a) and figure 2.9(c) shows the measurement circuit. Where  $C_p$  and  $G_p$  are given by:

$$C_p = C_s + \frac{C_{it}}{1 + (\omega\tau_{it})^2} \quad (2.9);$$

$$\frac{G_p}{\omega} = \frac{q\omega\tau_{it}D_{it}}{1 + (\omega\tau_{it})^2} \quad (2.10).$$

Where  $C_{it} = q^2D_{it}$ ,  $\omega = 2\pi f$  ( $f$  is measurement frequency),  $\tau_{it} = R_{it}C_{it}$  is the interface trap time constant and given by

$$\tau_{it} = [\vartheta_{th}\rho_s N_A \exp(-q\phi_s/kT)]^{-1} \quad (2.11).$$

Where  $\vartheta_{th}$ ,  $\rho_p$ ,  $N_A$  are thermal velocity, hole density at surface acceptor doping density. Equations 2.9 and 2.10 are used for interface traps with a single energy level. However, the traps distribute continuously in the bandgap. Therefore the capture and emission of carriers occur within a few thermal energy ( $kT/q$ ) above and below the Fermi level. Equation 2.12 takes into account the thermal effect:

$$\frac{G_p}{\omega} = \frac{qD_{it}}{2\omega\tau_{it}} \ln [1 + (\omega\tau_{it})^2] \quad (2.12).$$

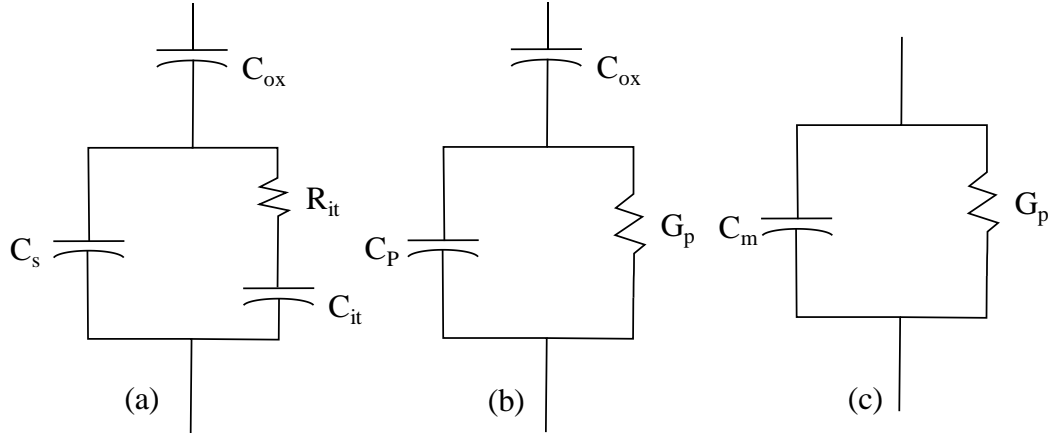


Figure 2. 9 Equivalent circuits for conductance measurement (a) metal oxide semiconductor, (b) simplified circuit, (c) measurement circuit.

### 2.3 Summary

Working principles of fabrication techniques relevant to IGZO TFT fabrication and characterization that were used in this thesis are presented. Techniques used for TFT fabrication involve DC magnetron sputtering, Plasma-Enhanced Chemical Vapor Deposition, inductively coupled plasma chemical vapor deposition and dry etching. The characterization techniques include secondary ion mass spectroscopy, X-ray diffraction, and X-ray reflectivity. The calculation method of mobility, flat band voltage and surface potential are also presented.

### ***3.1 Introduction***

InGaZnO (IGZO) has been widely accepted as a channel material for thin-film transistors (TFTs) backplanes for next generation active-matrix displays because of its excellent properties particularly transparency to visible light (bandgap of  $\sim 3.2$  eV), high electron mobility ( $5 \sim 50$  cm<sup>2</sup>/Vs), good uniformity, and low temperature fabrication [65]. Low power consumption, high frame rate and ultra-high resolution are several advantages of a display driven by an IGZO TFT array (IGZO display) relative to a display driven by an a-Si TFT array (a-Si display). Therefore, IGZO-TFTs are now used either in mobile device displays or in large size displays[31], [66]. In FPDs, a negative voltage is normally applied to the gate when the pixel is held. Besides of that the TFTs also be illuminated by the back light unit. The TFTs are worked under negative bias and illumination stress (NBIS). Therefore, the reliability of TFTs under NBIS is required for a display application. However, threshold voltage ( $V_{th}$ ) of IGZO TFT shifted negatively with the NBIS stress time [67]. The change in  $V_{th}$  induces a fluctuation in pixel brightness [68]. Therefore, the NBIS reliability is a critical issue for the FPD application. Numbers of researches relating to the NBIS instability in IGZO TFT have been reported [69]–[73]. The NBIS degradation mechanism of IGZO TFT has been extensively discussed. There are three commonly accepted reasons for the instability in IGZO TFT under NBIS: (i) hole trapping in a gate insulator (GI) [67], [74], [75]; (ii) the creation of ionized oxygen vacancies ( $V_O^+$  or  $V_O^{2+}$ ) [76]–[79]; and (iii) a creation of donor-like defects in IGZO bulk [80]. In 2009, by studying the effect of moisture on the NBIS instability in IGZO TFTs, Kwang-Hee et. al. suggested that hole trapping in the GI is the reason for the NBIS instability in the TFT. The absorbed H<sub>2</sub>O plays as midgap traps for hole generation [74]. In 2010, the donor-like defects were detected by C-V measurement [76]. Based on the results of first principles calculations [71], [81], the ionized oxygen vacancies ( $V_O^+$  or  $V_O^{2+}$ ) have been suggested as the origin of the donor-like defects. However, no direct evident has been provided to prove the suggestion. The results of hard X-ray photoelectron spectroscopy (HX-PES) [77], [82] and the photoelectron spectroscopy for chemical analysis (ESCA) measurements [53] imply that the defects were mainly generated at the back channel interface. In 2012, by extracting the flat band voltage in IGZO TFT, Jae Gwang et. al. proved that the trapping of positive charge at the front channel interface and defect

generation in the channel are reasons for the NBIS degradation in IGZO TFTs. In previous reports [67], [74]–[77], IGZO TFTs without etching-stopper (ES) and passivation layers (PS) were often used in NBIS testing. However, ES and PS layers are required to avoid environmental effects on the electrical stability of TFTs [83]–[85]. Moreover, little research relating to effect of NBIS on the hysteresis of IGZO TFTs has been reported. In this study, the hysteresis ( $V_h$ ) induced by NBIS of IGZO TFT with ES and PS layers was measured using double sweeping gate voltage mode (DSM). It was found that the hysteresis of IGZO TFT was enhanced drastically by NBIS. To investigate the mechanism of NBIS induced hysteresis, transfer characteristics measured by double sweeping gate voltage mode and by positive gate pulse mode were compared. The results suggest that trapped electrons at an IGZO/ES (back-channel) interface, trapped holes at a GI/IGZO (front-channel) interface, and donor-like states creation in an IGZO channel were possible reasons for NBIS instability of the IGZO TFTs.

### ***3.2 Experimental***

Figure 3.2(a) shows a cross sectional view of bottom-gate a-IGZO TFT. The IGZO TFTs with ES and PS layer were fabricated on a 4 inch glass substrate [86]. 50-nm-thick thin film Cr was deposited on a glass substrate by DC magnetron sputtering, and was patterned to form a gate electrode by photolithography and wet-etching. A 150-nm-thick  $\text{SiO}_x$  gate insulator (GI) was then deposited by Plasma-Enhanced Chemical Vapor Deposition (PE-CVD) at a substrate temperature of 350°C. A 45-nm-thick IGZO film was deposited on the GI by DC magnetron sputtering at a substrate temperature of 150, and was patterned to form an active channel by photolithography and dry-etching. An  $\text{Ar}/\text{O}_2$  gas flow rate of 18.7/1.3 sccm and a deposition pressure of 0.3 Pa were used for the IGZO deposition. A 200-nm-thick  $\text{SiO}_x$  etching stopper (ES) was deposited on the IGZO channel by PE-CVD at a substrate temperature of 170°C. Top contact holes were then opened by dry-etching. An Indium-Tin-Oxide (ITO) film was deposited by DC magnetron sputtering, and was patterned to form source-and-drain electrodes by dry-etching. A 200-nm-thick  $\text{SiO}_x$  passivation layer was deposited by PE-CVD at a substrate temperature of 170°C. Finally, measurement holes were opened by photolithography and dry-etching.

Before transfer characteristic measurements and reliability evaluations, the IGZO-TFTs were annealed for 1 hour in  $\text{N}_2$  ambient at 350°C. The electrical properties and reliability of the TFTs

were evaluated using an Aligent 4156C semiconductor parameter analyzer. Gate bias stresses ( $V_{st}$ ) of -20, -30 and -40 V with blue light ( $\lambda = 460$  nm) at a power density of  $0.2 \text{ mW/cm}^2$  were applied in NBIS testing. Single sweeping mode, double sweeping mode and positive gate pulse mode were used to measure the transfer characteristics of the TFTs. SWM is a transfer characteristic measurement in which gate voltage was swept a haft cycle from -10 to 20 V. On the other hand, the gate voltage was swept one cycle. The gate voltage was swept from -10 to 20 V in forward measurement and from 20 to -10 V in reverse measurement. Positive gate pulse mod is a transfer characteristic measurement method in which a positive gate pulse is applied to TFTs before every transfer characteristic measurement by double sweeping gate voltage mode. Schematic of the positive gate pulse mod is shown in figure 3.1. The threshold voltage ( $V_{th}$ ) is defined as the gate voltage at a drain current ( $I_D$ ) of 1 nA, and subthreshold swing [ $S_s = dV_g/d \log I_D$  (V/decade)], which is extracted near  $V_{th}$  region, is defined as the gate voltage required to increase  $I_D$  from 0.1 to 1 nA. The field effect mobility of IGZO TFTs was calculated using the formula 2.4.

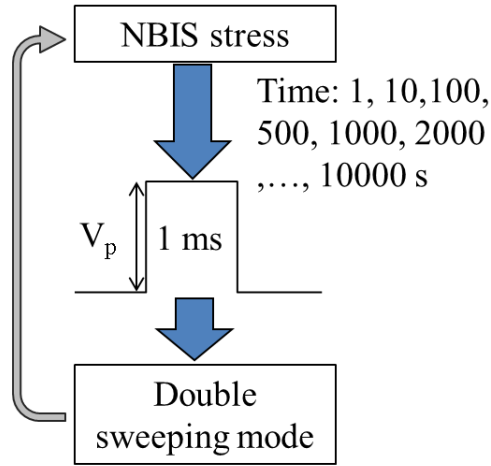


Figure 3. 1: The schematic of Positive gate pulse mode.

### 3.3 Results and Discussions

#### 3.3.1 NBIS degradation behavior

Figure 3.2(b) shows the initial transfer characteristics of TFTs. Field effect mobility in linear region was  $15.6 \text{ cm}^2/\text{V}\cdot\text{s}$ , sub-threshold swing ( $S_s$ ) value of 0.4 V/dec which was extracted from



$V_{GS}$  which required to increase the drain current ( $I_{DS}$ ) from 0.1 to 1 nA. Turn-on voltage of 1.65 V was defined by  $V_{GS}$  at  $I_{DS}$  of 1 nA, and hysteresis ( $V_h$ ) of the transfer curves was 0.4 V.

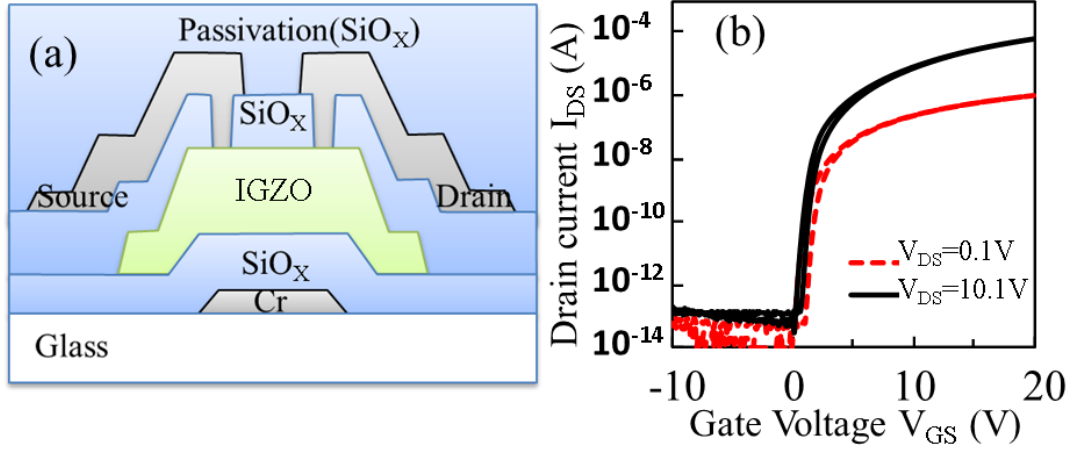


Figure 3. 2: (a) Schematic cross-sectional view and (b) initial transfer characteristics of a-IGZO TFTs.

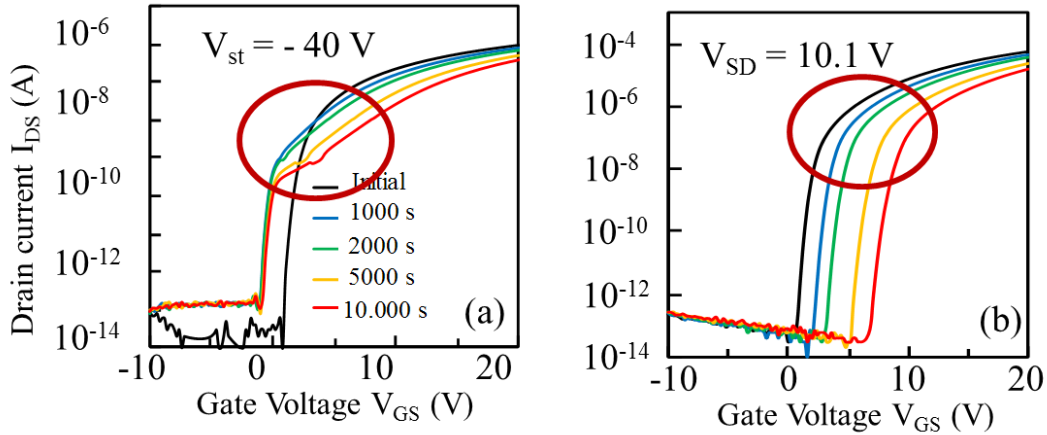


Figure 3. 3: The change in TFT transfer characteristic with NBIS duration measured by single sweeping mode (a) first time measurement ( $V_{DS} = 0.1$  V), (b) second time measurement ( $V_{DS} = 10.1$  V).

Figures 3.3(a) and 3.3(b) show the NBIS stress time dependence of TFT transfer curve, which was measured by single sweeping mode. When the NBIS stress time exceeded the certain value, the incident light was temporary turn off for the transfer characteristic measurement. The TFT transfer curve was first measured with a  $V_{DS} = 0.1$  V, following by a second time measurement with a  $V_{DS} = 10.1$  V. The result of first and second time measurement is shown in

figure 3.3(a) and 3.3(b) respectively. Figure 3.3(a) shows that the transfer characteristic was negatively shifted with Ss degradation. However, the Ss degradation vanished in the second time measurement. The transfer curves which were measured in the second time measurement parallel shifted in positive direction. These results suggested that the single sweeping mode was not fully captured the NBIS degradation behaviors. Therefore, the double sweeping mode measurement was used to measure the TFT transfer characteristic under NBIS.

Figures 3.4(a) and 3.4(b) show the transfer characteristic measured by double sweeping mode of IGZO TFT under NBS (without light illumination) and under NBIS (with light illumination), respectively. The NBIS stress time dependence of  $V_h$  is shown in figure 3.4(c). The  $V_{st}$  of -40 V were applied in both NBS and NBIS testing. The threshold voltage and hysteresis of IGZO TFTs were stable under NBS, as shown figure 3.4(a). On the other hand, it was found that  $V_h$  increased gradually from 0.4 to 8.7 V with NBIS duration, as shown in figure 3.4(c). Figure 3.4(b) shows that under NBIS, the transfer curve in forward measurement shifted negatively with Ss degradation. The Ss degradation did not obtained in reverse curves. The reverse curves parallel positively shifted.

The effect of  $V_{st}$  on NBIS degradation behaviors was also investigated. Figures 3.5(a) and 3.5(b) show the transfer characteristics, which were measured by double sweeping mode, of a-IGZO TFTs before and after  $10^4$  s NBIS with  $V_{st}$  of -20 and -40 V, respectively. The  $V_{rev}$  of the IGZO TFTs was stable under the NBIS testing with a  $V_{st} = -20$  V, the forward curve negatively shifted without Ss degradation. The parallel shift in negative direction of forward curve indicates that positive charges, which were generated in the TFT under NBIS, were trapped in the GI and/or at the GI/IGZO interface [74], [75]. These trapped positive charges could have been de-trapped when gate voltage was swept in positive region during the forward measurement. Therefore, the transfer curve hardly shifted in reverse measurements. Nevertheless, when  $V_{st}$  was increased from -20 to -40 V, (a) a positive  $V_{th}$  shift of 7.1 V without Ss degradation was observed in reverse measurement; (b) a negative  $V_{th}$  shift with Ss degradation was observed in forward measurement; and (c) the  $V_h$  at the NBIS duration of  $10^4$  s increased from 0.4 to 8.7 V. We will investigate the reason for the parallel shift in the positive direction of the reverse curve in section 3.3.2. The reasons for the negative shift with Ss degradation in forward curve and for the increasing hysteresis with NBIS duration will be clarified in section 3.3.3.

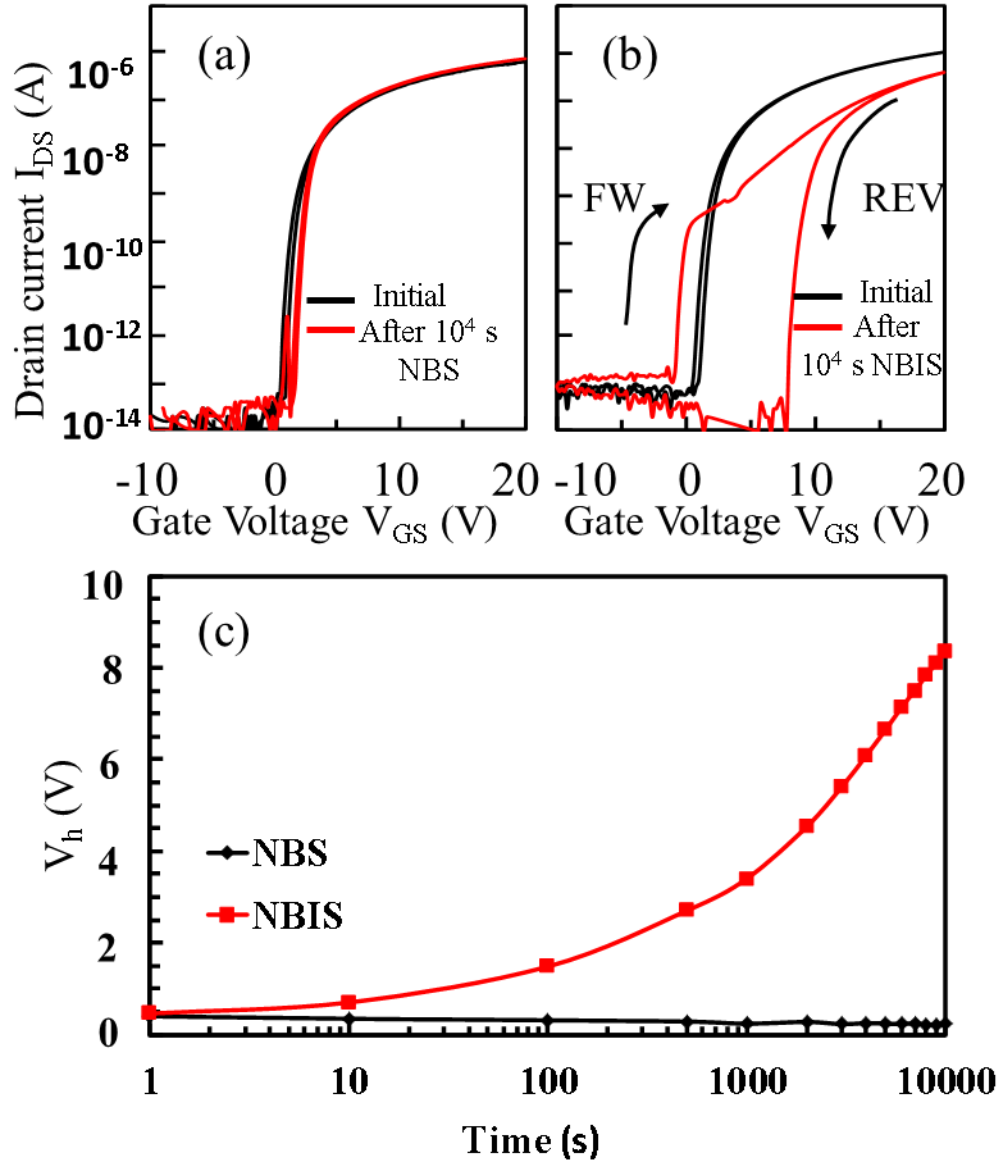


Figure 3. 4: Transfer characteristics of a-IGZO TFTs before and after (a) NBS and (b) NBIS, (c) the change of hysteresis under NBS and NBIS as a function of stress duration of  $10^4$  s.

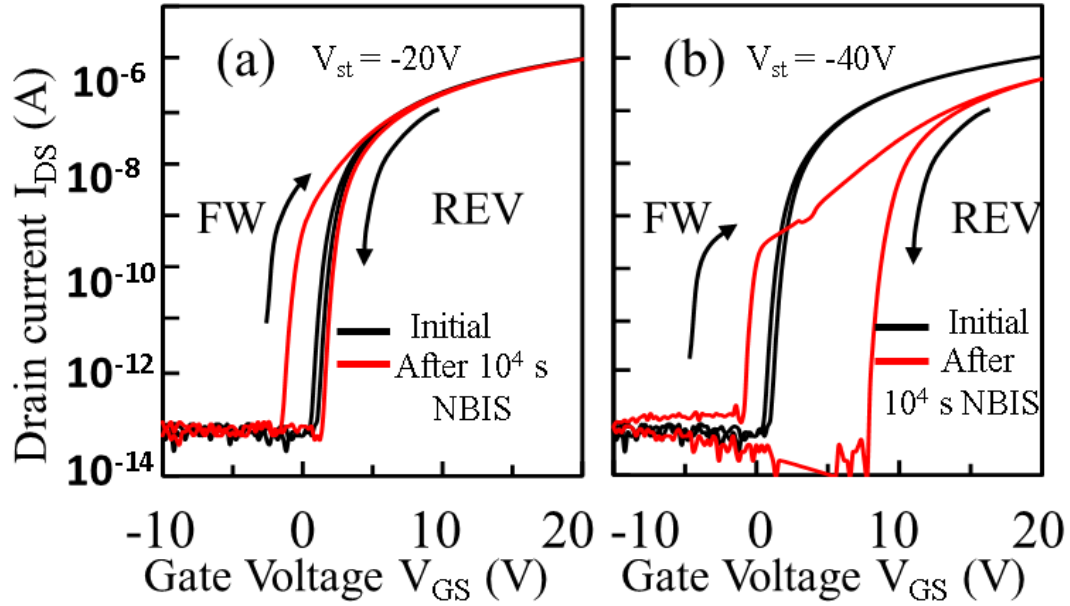


Figure 3. 5: Transfer characteristics of a-IGZO TFTs before and after NBIS (a)  $V_{st} = -20$  V, and (b)  $V_{st} = -40$  V.

### 3.3.2 Trapped electrons at the back channel interface

In order to investigate the reason for the positive  $V_{th}$  shift in reverse measurement ( $V_{rev}$ ), the effect of  $V_{st}$  on the positive shift of  $V_{rev}$  was studied. Figure 3.6(a) shows the transfer characteristics of IGZO TFTs in reverse measurement after  $10^4$  s NBIS with  $V_{st} = -20, -30$  and  $-40$  V. The reverse curves shifted positively without Ss degradation.  $\Delta V_{rev}$  steadily increased from 0.6 to 7.1 V when  $V_{st}$  was increased from  $-20$  to  $-40$  V. The change in  $\Delta V_{rev}$  with NBIS stress time was well fitted (as shown in figure 3.6(b)) to the commonly used stretched-exponential equation [87]:

$$\Delta V_{rev} = \Delta V_{rev0} \{1 - \exp[-(\frac{t}{\tau})^\beta]\},$$

where  $\Delta V_{rev0}$  is the approximate effective voltage drop across the gate insulator and channel and equals  $\Delta V_{rev}$  at infinity time,  $\tau = \tau_0 \exp(E_\tau/kT)$  represents the characteristic trapping time of carriers in which  $\tau_0$  is the thermal prefactor, thermal activation energy is given by  $E_a = E_\tau \beta$  ( $\beta$  is the stretched-exponential exponent and  $E_\tau$  is the average effective energy barrier that electrons in the a-IGZO TFT channel need to overcome to enter the insulator). The above results are consistent with those from positive bias induced instability in a-Si TFTs [87] or in a-IGZO

TFTs,[88], [89] in which the positive shift of  $V_{th}$  was mainly determined by the induced stress amplitudes, interface qualities and following a function  $\Delta V_{th} \propto (V_{st} - V_i)^\alpha$ .  $V_i$  here is the initial threshold voltage; and  $\alpha$  is a parameter associated with the interface qualities. These results suggest that electron trapping may be one reason for the parallel shift in positive direction of the reverse curve. Since negative gate bias was applied during NBIS, electrons could not have been trapped in a GI or at a GI/IGZO interface. Under a transverse electric field induced by  $V_{st}$ , electrons generated by NBIS were trapped at an IGZO/ES interface and/or in an ES. Those trapped electrons moved the conduction band maximum of the IGZO channel upward, resulting in a positive  $V_{rev}$  shift. This could also explain the dependence mentioned above of  $\Delta V_{rev}$  on  $V_{st}$ . When  $V_{st}$  was increased, the electric field at the back channel interface ( $E_b$ ), which assisted the trapping of electrons in an IGZO/ES interface or ES, also increased. Increasing  $E_b$  enhanced the trapping of electrons in an ES and/or at an IGZO/ES interface. As a result, the  $\Delta V_{rev}$  steadily increased from 0.65 to 7.14 V when  $V_{st}$  was increased from -20 to -40 V.

### 3.3.3 Positive gate pulse measurement method

The evolution of forward transfer curves of TFT under NBIS with  $V_{st}$  of -40 V is shown in figure 3.7(a). When stress time was smaller than 500 s,  $V_{th}$  obtained by forward measurement shifted negatively without Ss degradation. The parallel negative  $V_{th}$  shift indicates that holes were trapped at the GI/IGZO interface and/or in the GI. Subsequently, hump effect appeared together with Ss value degraded when stress time was greater than 500s. The appearance of hump and the degradation of Ss value indicate that defects were generated in an IGZO channel.

In order to further identify the degradation mechanisms of IGZO TFTs under NBIS in forward measurement, positive gate pulse mode with pulse width of 1 ms and pulse height of 10 V was used. Figure 3.7(b) shows the change in transfer characteristics of the TFTs after  $10^4$  s NBIS measured by double sweeping mode (without positive gate pulse (w/o P)) and positive gate pulse mode (with positive gate pulse). When the positive gate pulses were applied,  $V_h$  after  $10^4$  s NBIS decreased and the “hump” effect in forward curves disappeared. Figures 3.7(c) and 3.7(d) respectively show  $V_h$  and Ss value in forward curve, which were measured with and without the positive gate pulse, as a function of NBIS time, respectively. There was no difference in  $V_h$  measured with and without positive gate pulse when stress time was smaller than 500 s. However,  $V_h$  measured by positive gate pulse mode was smaller than that measured by double

sweeping mode when stress time was larger than 500 s. The results are shown in figure 3.7(c). This behavior was similar to that for  $S_s$  values, as shown in figure 3.7(d). When positive gate pulse was applied, the degradation of  $S_s$  was suppressed, even for NBIS stress time exceeding  $10^3$  s. This result suggests that the defects, which were observed in forward measurement, nearly vanished when positive gate pulse was applied prior to transfer characteristic measurement. This result could be explained as follows: The positive gate pulse induced an accumulation of electrons in an IGZO channel. The defects spontaneously captured the accumulated electrons and as a result become stable. Based on the results of our previous study [78], the defects here could be ionized types of oxygen vacancies ( $V_O^+$  or  $V_O^{2+}$ ). These cations would have been neutralized by capturing electrons. As a consequence, the hysteresis decreased from 8.7 to 6.4 V and the disappearance of hump in forward curve, as shown in figure 3.7(b).

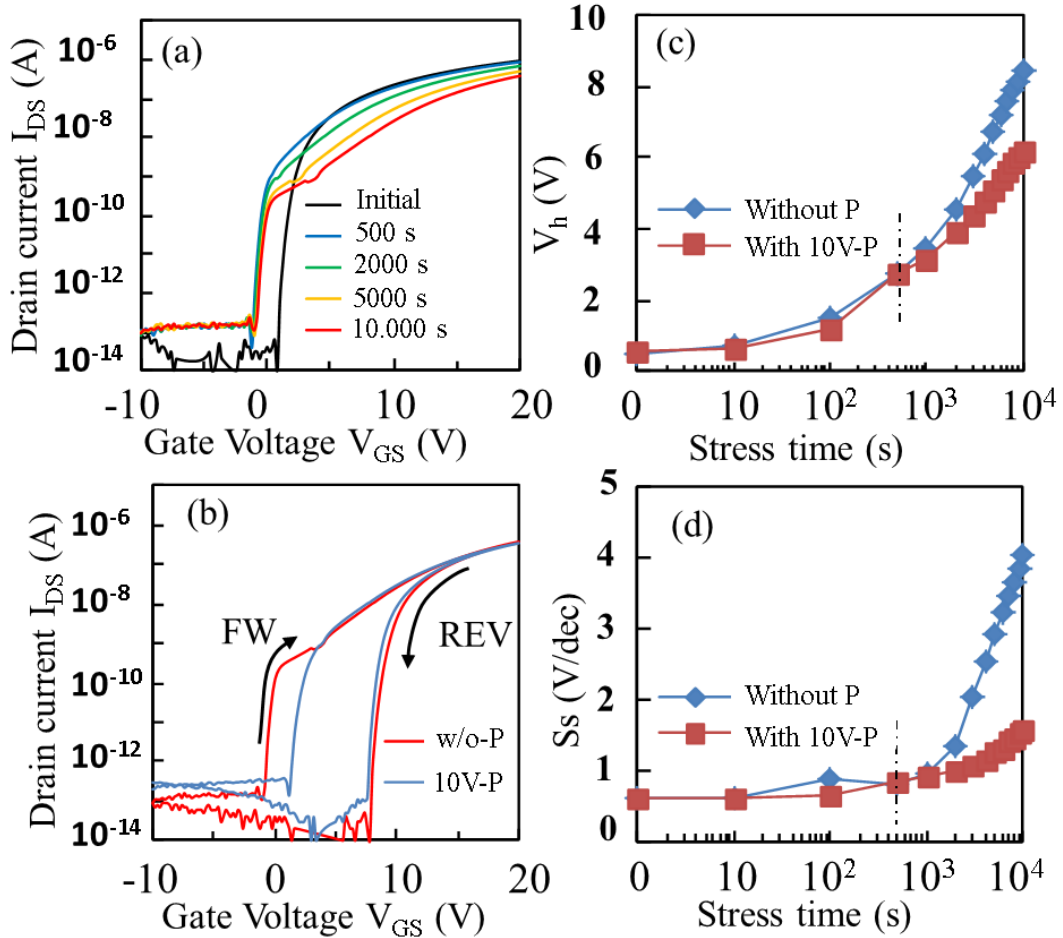


Figure 3. 6: (a) Change in transfer characteristics under NBIS with  $V_{st} = -40$  V in forward measurement, (b) Transfer characteristic of TFTs without and with 1 ms - 10 V positive gate pulse after NBIS of  $10^4$  s, the change of (c) hysteresis and (d)  $S_s$  value as a function.

Figure 3.7(a) shows that on-current degraded with NBIS stress time. To identify the reason for this on-current degradation, the dependence of the extracted mobility on NBIS stress time was considered. Figure 3.8 shows the change in linier field effect mobility with NBIS duration. The mobility – gate voltage curve was parallel shifted to the positive direction. This result implies that the on-current shown in figure 3.7(a) did not relate to the degradation of the mobility. One plausible reason for the on current degradation is the positive shift of  $V_{th}$ . In other word, the trapped electron at the back channel interface decreased electron concentration in IGZO channel.

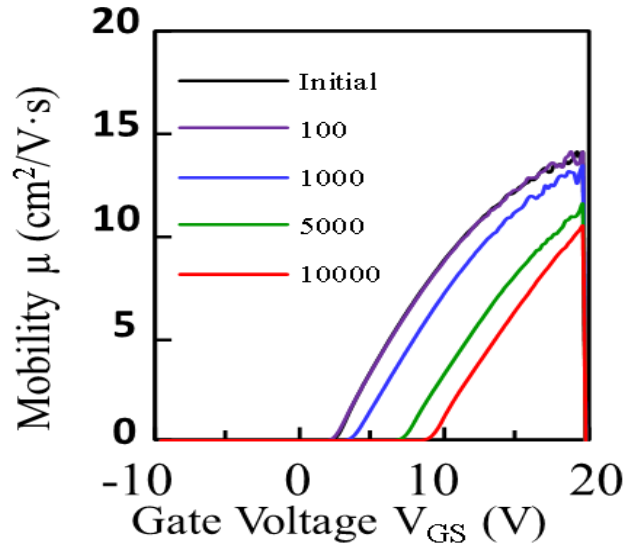


Figure 3. 7: The change in field-effect mobility with NBIS duration

#### 3.3.4 Effects of pulse height and pulse width on hysteresis

The effect of pulse width and of pulse height on the transfer characteristic of the IGZO-TFT after  $10^4$  s NBIS stress is shown in figure 3.9(a) and 3.9(b), respectively. When the gate pulse height/width of 5 V/1 ms was applied, the Fermi level moved upward but did not reach the highest energy level of the donor-like defects; hence the defects were not completely stabilized. As a result, hysteresis decreased from 8.7 to 7.5 V, but Ss degradation still observed in the forward curve. Nevertheless, when gate pulse height was increased to 15 V, the Fermi level exceeded the donor-like defects energy. Most of the generated defects captured the accumulated electrons, as a consequence, these defects became stabilized. Therefore, the hysteresis further decreased to 4.6 V the Ss degradation disappeared in forward curve. The high voltage positive

gate pulse also assisted hole de-trapping from the GI or GI/IGZO interface. Consequently, hysteresis of IGZO TFTs further decreased, as shown in figure 3.9(a). The effect of gate pulse width on the hysteresis of an IGZO TFT is shown in figure 3.9(b). The hysteresis of the IGZO-TFT decreased from 8.4 to 0.9 V when a positive gate pulse with pulse high of 10 V and pulse width of 25 s was applied. One plausible reason for the further decrease in the hysteresis when the long positive gate pulse was applied was that positive gate pulse assisted hole de-trapping from the GI or the GI/IGZO interface. It should be noted that, as shown in figure 3.9(a) and 3.9(b), the  $V_{rev}$  was the same with positive gate pulse and without. This result implies that the trapped electrons at the back channel interface did not de-trap when a positive gate voltage was applied. This mean that the trapped electrons at the back channel interface did not participate in the hysteresis induced by NBIS. Hence, the donor-like defect generation/stabilization in the IGZO channel and hole trapping/de-trapping in a GI were causes of NBIS induced hysteresis in IGZO TFTs.

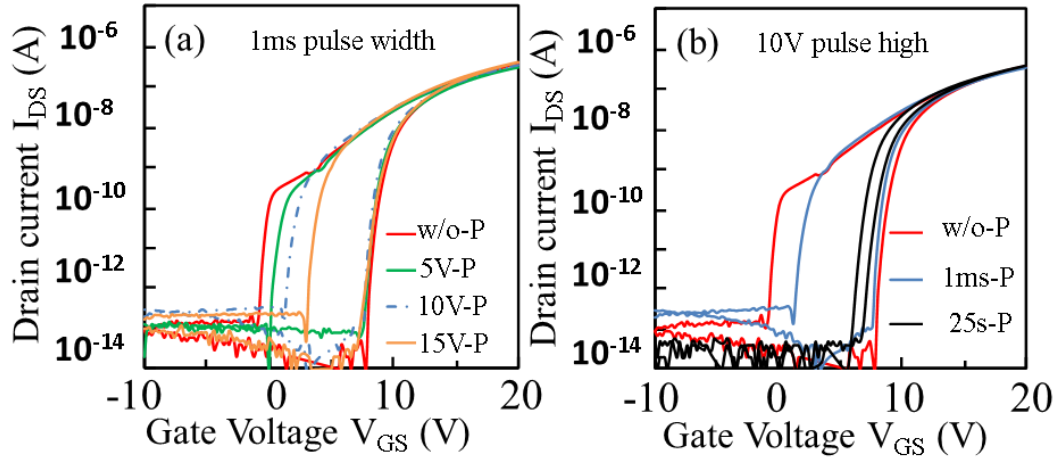


Figure 3. 8: Transfer characteristic of TFTs after NBIS of  $10^4$  s (a) without and with 1 ms pulse width and 5, 10, 15 V pulse high positive of gate pulse, (b) without and with 1 ms and 25 s pulse width and 10 V pulse high of positive gate pulse.

### 3.3.5 The NBIS degradation mechanism

Based on the discussions above, we propose a new degradation mechanism of a-IGZO TFTs under NBIS, which is illustrated in figure 3.10. At the early state of NBIS, the trapped holes in the GI or at the GI/IGZO interface were the main factor causing negative shift of transfer curves in forward measurement. These trapped holes were de-trapped during forward measurement;



thus, transfer curves in reverse measurement hardly changed. Subsequently, when the NBIS stress time was increased, electrons were trapped in an ES or at the ES/IGZO interface, inducing a positive shift of threshold voltage in the reverse measurement. In addition, donor-like defect generation occurred together with positive charge trapping in the GI or at the GI/IGZO interface. Therefore, negative shift of transfer curve with hump was observed in forward measurement. We infer that hole trapping/de-trapping in the GI or at the GI/IGZO interface and donor-like defect generation/stabilization caused NBIS induced hysteresis and hump in forward measurement.

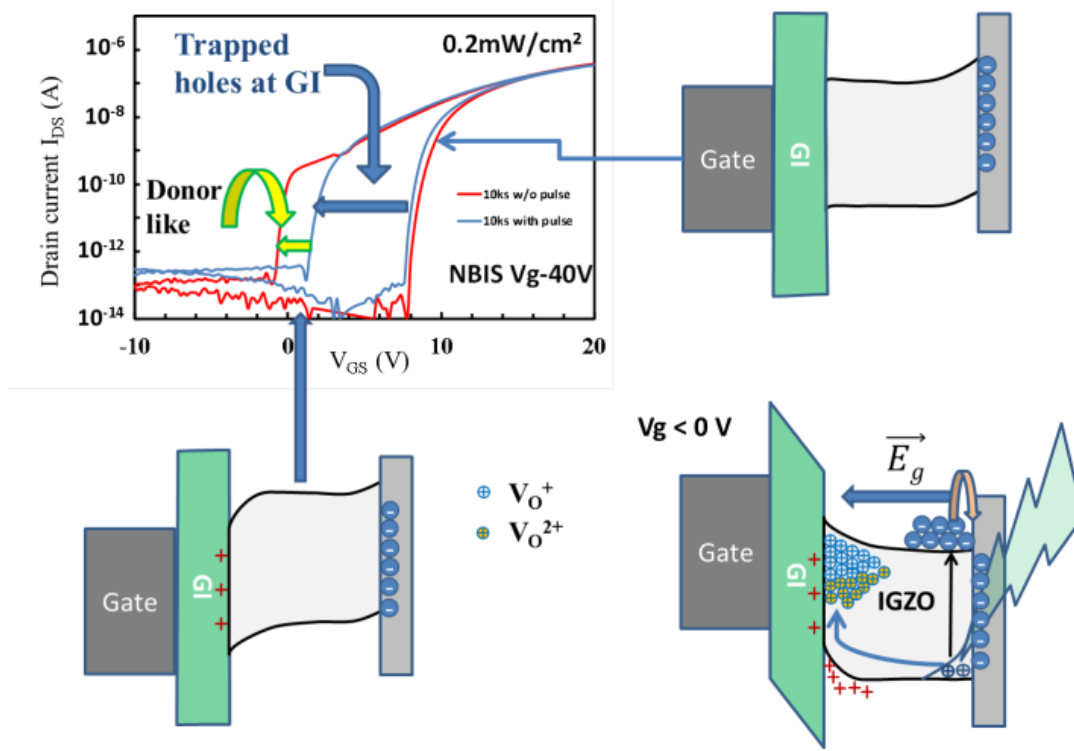


Figure 3. 9: Schematics band diagrams of degradation mechanism under NBIS.

### 3.4 Summary

In this chapter, we proposed a new measurement method, named as positive gate pulse mode, to investigate the NBIS degradation mechanism of IGZO TFT. It was found that a single sweeping mode did not fully capture the NBIS degradation behaviors in IGZO TFT. Therefore, a double sweeping mode was conducted. Transfer curve measured by double sweeping mode show that reverse curve positively shifted during NBIS. The dependence between threshold voltage in reverse curve and NBIS duration followed the exponential equation. These results indicate that electron trapping at the back channel interface was a caused of the NBIS instability in IGZO TFT.

The trapped electrons at the back channel interface induced a positive shift in reverse curve. Results measured by double sweeping mode indicate that in the future work to improve reliability of IGZO TFTs, the quality of the back channel interface should be considered. Forward curve shown the negative shift with an  $S_s$  value degradation. This results implies that the defect generation in the channel and of the hole trapping in the GI are reasons for the negative shift with an  $S_s$  degradation in the forward curve. The positive gate pulse mode was used to clarify the reasons for the forward curve degradation. The pulse width and pulse height for the positive gate pulse mode measurement were optimized to quantitative analysis effect of the hole trapping and the defects generation on the NBIS instability in IGZO TFT. Using positive gate pulse measurement method, we found that the hole trapping was the main cause of the forward curve degradation in the TFT under NBIS test. Therefore, reducing hole trapping in the GI will have strong impact on further work to improving the NBIS reliability. These results suggest that positive gate pulse mode is an effective and meaningful measurement method to quantitative analysis effect of the trapped hole and defect generation on the NBIS reliability of IGZO TFT.

### 4.1 Introduction

As we presented in chapter 3, there are three possible reasons for NBIS instability in IGZO TFTs: (i) hole trapping in a gate insulator (GI) [74], [75], (ii) donor-like defect generation in the IGZO channel [76]–[78], and (iii) electron trapping at a back channel interface [70], [90]. In this chapter, we will discuss about methods to reduce the defect generation in IGZO TFT under NBIS testing. Results of XPS measurement have been indicated that the defect generation could be reduced by annealing IGZO TFTs in a high pressure water vapor [91], high pressure O<sub>2</sub> [92], wet O<sub>2</sub> [93], hydrogen environment [94]. An AlO<sub>x</sub>, SrO<sub>x</sub> passivation layer could be used to suppress deep subgap defects in the IGZO channel [77], [95]. In this study, we investigate the effect of IGZO deposition temperature on the defect generation in the TFT channel under NBIS. However, The NBIS degradation mechanism of IGZO TFT is very complicate as mentioned above. Therefore, it is difficult to clearly identify the effect of a fabrication/treatment condition on the defect generation and on hole trapping. On the other hand, unlike a-Si TFT, the NBIS degradation mechanism in IGZO TFT is not consistent. It depends on the TFT structure [96], the IGZO composition [97] and the fabrication process[72]. Therefore, a quantitative analysis effect of hole trapping and of donor-like defect generation on the NBIS instability is essential in the work to improve oxide TFT stability.

Capacitance-voltage measurement is usually used to detect defect generation in the IGZO channel[79], [98]. Subthreshold voltage swing [ $S_s = dV_g/d \log I_D$  (V/decade)] could also be used to estimate the total number of generated defects ( $\Delta N_{\text{defect}}$ ) using the equation:

$$\Delta N_{\text{defect}} = (C_i/q)[q \log(e) \Delta S_s / (KT) - 1]. \quad (4.1)$$

The threshold voltage shift induced by generated defects ( $\Delta V_{\text{defect}}$ ) can be calculated using the following equation:

$$\Delta V_{\text{defect}} = q \Delta N_{\text{defect}} / C_i \quad (4.2)$$

where  $C_i$  is gate capacitance per unit area,  $q$  is the elementary charge,  $K$  is the Boltzmann constant and  $T$  is the absolute temperature (K). However, to the best of our knowledge, there is no direct method for separately measuring of hysteresis induced by trapped hole in a gate

insulator ( $\Delta V_{\text{hole}}$ ) and hysteresis induced by defect generation in a channel ( $\Delta V_{\text{defect}}$ ). In this chapter, we used our developed measurement method, referred to in chapter 3 as positive gate pulse mode, which can estimate  $\Delta V_{\text{hole}}$  and  $\Delta V_{\text{defect}}$ . We found that IGZO deposition temperature strongly affects defect generation in the channel under NBIS.

## 4.2 Experimental

Figure 4.1(e) shows the cross sectional view of a bottom-gate top-contact IGZO-TFT which was fabricated on a glass substrate. The fabrication process of IGZO TFT was the same as one, which is presented in chapter 3, exception for the channel deposition temperature. In this work, A 45-nm-thick IGZO film was deposited on the GI by DC magnetron sputtering at a substrate temperature of room temperature (TFT-1), 150 (TFT-2), and 220°C (TFT-3). An Ar/O<sub>2</sub> gas flow rate of 18.7/1.3 sccm and a deposition pressure of 0.3 Pa were used for the IGZO deposition.

Before transfer characteristic measurements and reliability evaluations, the IGZO-TFTs were annealed for 1 hour in N<sub>2</sub> ambient at 350°C. An Aligent 4156C semiconductor parameter analyzer was used to evaluate electrical properties and reliability of the TFT and was controlled by an Agilent VEE program. The transfer characteristic of IGZO-TFTs with a channel width/length of 50/20  $\mu\text{m}$  were measured using double sweeping mode and positive gate pulse mode [70]. The positive gate pulse not only stabilizes the generated defects but also assists hole de-trapping from the GI. Therefore, the pulse width was set at 1 ms, and the pulse height was determined by  $V_{\text{th}}$  in reverse measurement ( $V_{\text{rev}}$ ) of the TFT after 10<sup>4</sup> s NBIS in order to stabilize the generated defects, and to reduce hole de-trapping from the GI.

## 4.3 Results and Discussions

### 4.3.1 Effects of IGZO deposition temperature on the initial properties

Figures 4.1(a), 4.1(b) and 4.1(c) show the transfer characteristics of TFT-1, TFT-2 and TFT-3, respectively.  $S_s$  values of all TFTs fluctuated between 0.38 and 0.42 V/decade. However, electron mobility decreased from 17.14 to 12.19 cm<sup>2</sup>/Vs and  $V_{\text{th}}$  decreased from 3.41 to 1.98 V when the deposition temperature of the IGZO channel was increased from RT to 220°C. The correlation between electron mobility,  $V_{\text{th}}$  and IGZO deposition temperature is shown in figure 4.1(d). Hall measurement of the IGZO thin film showed that when IGZO deposition temperature was increased from RT to 220°C, carrier concentration increased from  $-7 \times 10^{18}$  to  $-3 \times 10^{19}$  cm<sup>-3</sup>,

resulting in the decrease in  $V_{th}$  mentioned above. It is known that carrier mobility in an IGZO films

increases with carrier concentration due to the potential barrier, which located in vicinity of conduction band edge, can be overcome [40], [65]. However, our results show that the mobility decreases when carrier concentration increases. In order to investigate the reason, 100 nm IGZO film was deposited on high conductive Si substrate at RT and 220°C. The composition and hydrogen content in an IGZO film were evaluated using the secondary ion mass spectrometry (SIMS) measurement. Figures 4.2(a) and 4.2(b) show the composition distribution and hydrogen profile in an IGZO film deposited at RT and 220°C respectively. Results of SIMS measurement show that In, Ga, O did not depend on the IGZO deposition temperature. However, hydrogen concentration in the IGZO film deposited at 220°C was higher than that in the films deposited at RT. The increasing hydrogen concentration in the IGZO films with deposition temperature is consistent with the deposition temperature dependence of the carrier concentration in IGZO and  $V_{th}$  mentioned above. On the other hand, it was reported that hydrogen plays not only as a shallow donor [99] but also as a scattering center in the conduction path [100], [101]. Therefore, the carrier scattering induced by hydrogen is one possible reason for the decrease in carrier mobility mentioned above. The free hydrogen and hydrogen contained compounds in a sputtering chamber and in a sputtering target can act as the sources for hydrogen in IGZO film [102], [103]. It has been reported that the diffusion coefficient [102] and solubility [104] of hydrogen increase with temperature. As a result, the hydrogen contain in the IGZO film deposited at 220°C was higher than that deposited at RT.

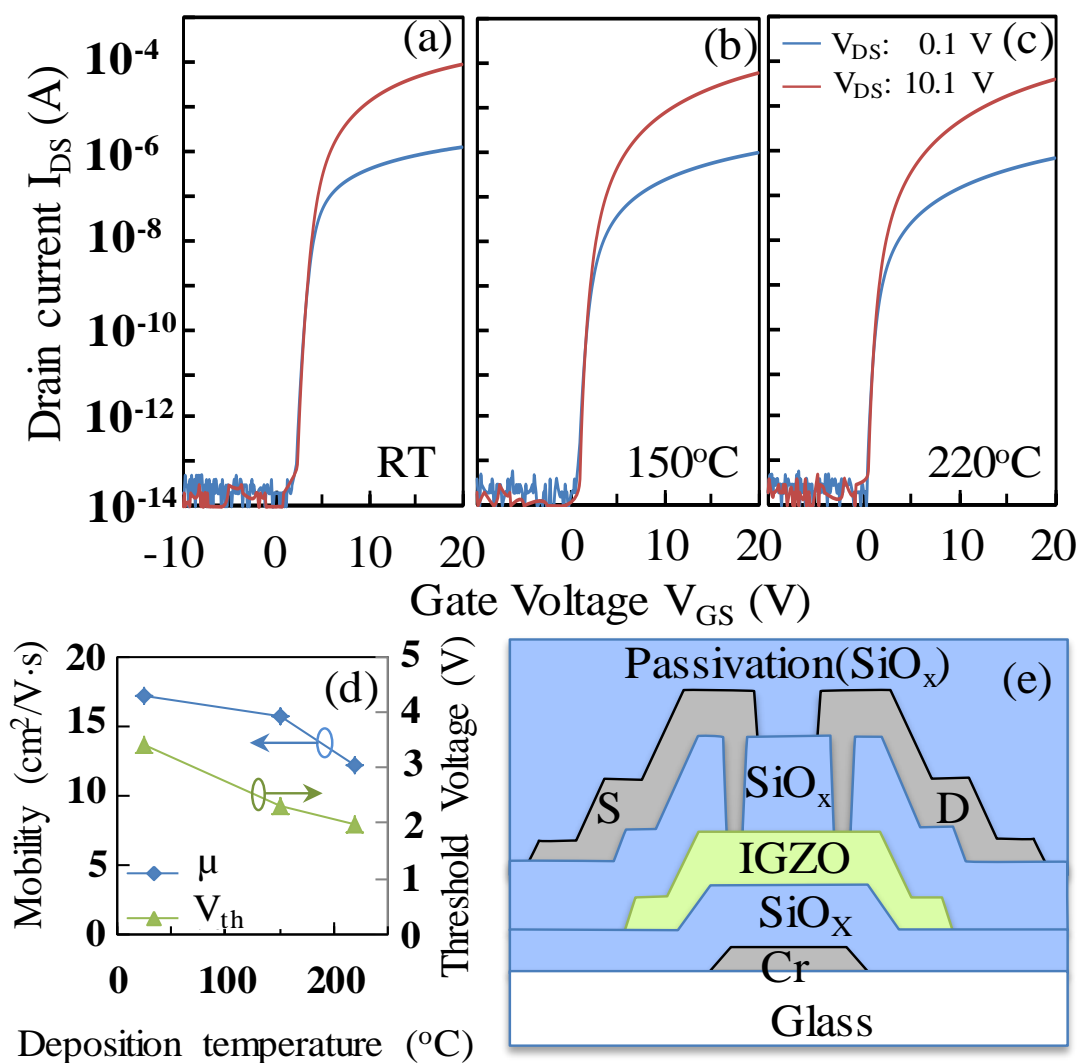


Figure 4. 1 Transfer characteristic of (a) TFT-1, (b) TFT-2, (c) TFT-3, (d) correlation between electron mobility, threshold voltage and IGZO deposition temperature, and (e) cross section view of IGZO-TFT.

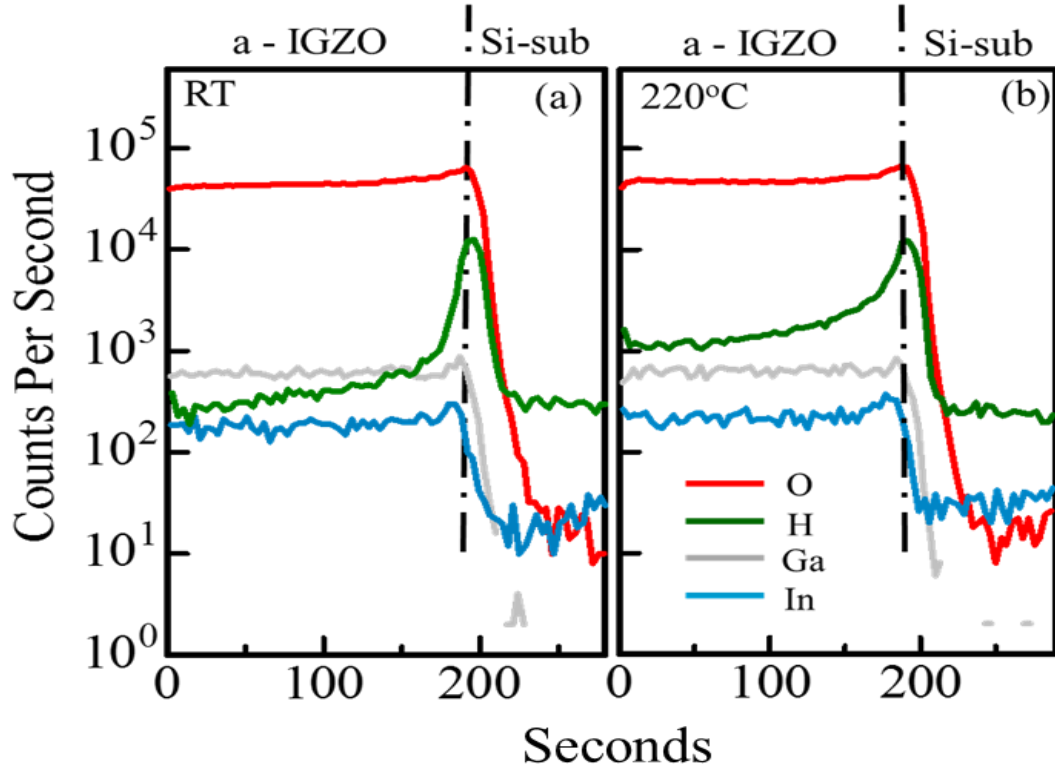


Figure 4. 2: The SIMS profile of hydrogen, Indium, gallium and oxygen in 100nm IGZO film deposited at (a) RT, (b) 220°C.

#### 4.3.2 Quantitative effects of IGZO deposition temperature on the hole trapping and defect generation in IGZO TFT under NBIS

The transfer characteristics measured using DSM and PGPM from TFT-1, TFT-2 and TFT-3 after  $10^4$  s NBIS are shown in figure 4.3(a), 4.3(b) and 4.3(c) respectively. Figures 4.3(d), 4.3(e) and 4.3(f) display the duration of  $V_h$  measured from TFT-1, TFT-2 and TFT-3 using DSM and PGPM. In forward curve measured by DSM, (1) “hump” appeared, (2) the reverse curve shifted positively and the “hump” in forward curve disappeared in reverse curve, (3) a hysteresis increased and (4) on current decreased.

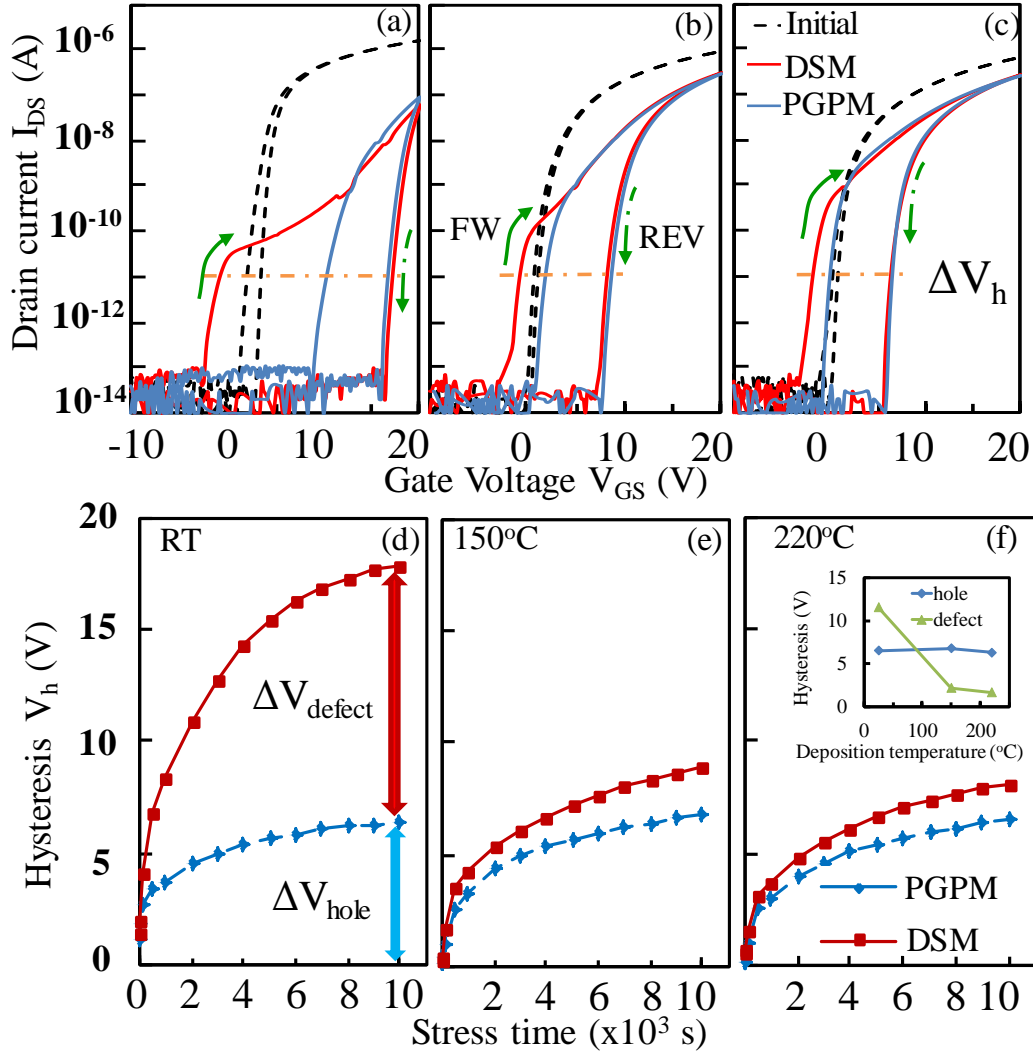


Figure 4. 3: Transfer characteristic of (a) TFT-1, (b) TFT-2, (c) TFT-3 after  $10^4$  s NBIS measured using double sweeping mode and positive gate pulse mode, and duration of hysteresis detected using double sweeping mode and positive gate pulse mode in (d) TFT-1, (e) TFT-2, (f) TFT-3 under NBIS (Inset shows dependence of  $\Delta V_{defect}$  and  $\Delta V_{hole}$  on IGZO deposition temperature)

As we reported in ref [105] and discussed in chapter 3, the electron trapping at the back channel interface causes the positive shift in the reverse curve without mobility degradation. Therefore, the on-current degradation is due to positive shift of  $V_{th}$  rather than mobility degradation in the TFT. Figures 4.3(a), 4.3(b), and 4.3(c) show that the on current degradation in TFT is proportional to the positive shift in reverse curve. These results strongly support the



hypotheses that the electron trapping at a back channel interface is a reason of a positive shift in reverse curve and of on current degradation. As we discussed in chapter 3, the “hump” in forward curve is caused by the defect generation in the IGZO channel under NBIS. Defect generation/stabilization in the IGZO channel and hole trapping/de-trapping in the GI induce hysteresis in the TFT under NBIS. The defect generation could be stabilized and the hole trapping in a GI could be de-trapped during forward measurement. As a result, the reverse curve shifted without Ss degradation in positive  $V_g$  direction. As shown in figures 4.3(a), 4.3(b) and 4.3(c), hysteresis measured using DSM dramatically decreased from 17.9 to 9.0 V when the IGZO deposition temperature was increased from RT to 150°C. When the deposition temperature was further increased from 150°C to 220°C, hysteresis decreased slightly from 9.0 to 8.1 V. In order to investigate reasons for this difference in hysteresis between TFT-1, TFT-2 and TFT-3, it is essential to quantify the effect of hole trapping and of defect generation on hysteresis.

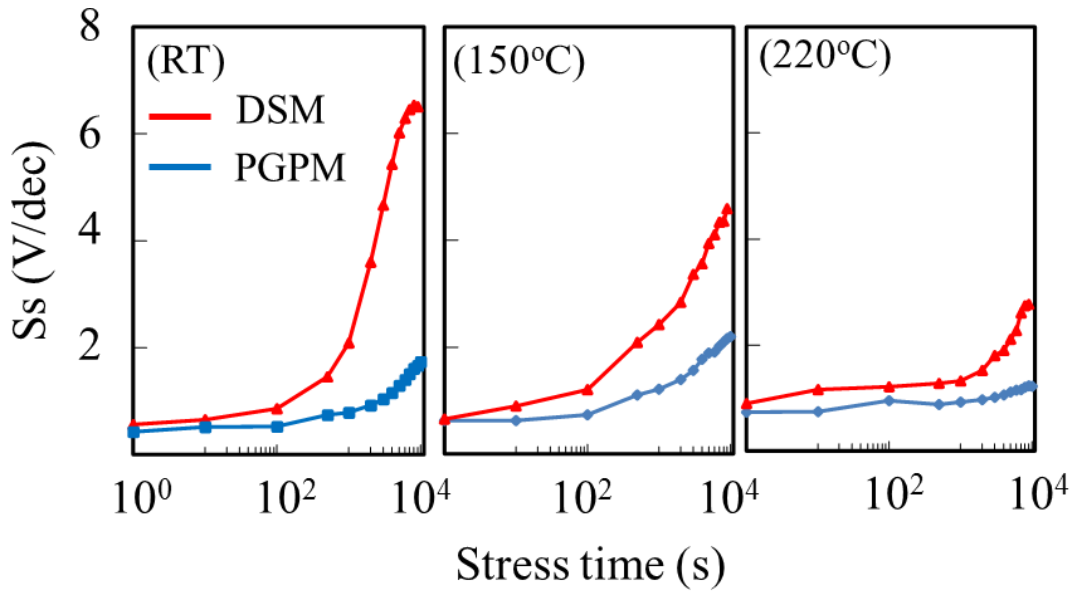


Figure 4. 4: The NBIS stress time dependence of subthreshold swing for different IGZO deposition temperature.

In this study, we used PGPM to measure hysteresis induced by trapped holes ( $\Delta V_{\text{hole}}$ ) in a GI. After positive gate pulse was applied to the TFT, the Ss value in all TFTs did not degrade and “hump” disappeared and as shown in figure 4.3(a), 4.3(b) and 4.3(c). Figure 4.4 show the change Ss values, which were measured by double sweeping mode and positive gate pulse mode, with the NBIS stress time. The Ss value measured by positive gate pulse mode did not degraded. This results indicate that the generated defects were stabilized. As we discussed in the previous report

[70], a short positive gate pulse induces an electron accumulation in the IGZO channel. The generated defects become stable by spontaneously capturing the accumulated electrons. Therefore, the hysteresis detected using positive gate pulse mode was induced by trapped holes in a GI. As shown in inset figure 4.3(f), even though hystereses measured using double sweeping mode were different and strongly dependent on IGZO deposition temperature, hystereses measured from TFT-1, TFT-2 and TFT-3 using PGPM were not substantially different. Since the energetic bombardment of negative oxygen ion, which was accelerated by the applied electric field between the substrate and the target in DC magnetron sputtering, would be the reason for the GI/channel interface damage [106], [107]. In this work, all TFTs were fabricated under the same conditions exception for IGZO deposition temperature, it is reasonable to assume that the qualities of SiO<sub>x</sub> GIs are similar for all TFTs. On the other hand, it is also well established that trapped carriers in a GI are mainly determined by gate bias stress and GI quality [87], [88]. At the same gate voltage stress and at similar GI quality, the hole trapping in GIs are approximately equal for all TFTs. As a result, hystereses measured using positive gate pulse mode from TFT-1, TFT-2 and TFT-3 were almost identical. Since the measurement results show remarkable agreement with the theory predicted results; positive gate pulse mode can be used for an estimation of  $\Delta V_{\text{hole}}$  in the IGZO TFT under NBIS.

As mentioned above, hole trapping in a GI and defect generation in the IGZO channel are the causes of hysteresis in IGZO TFT under NBIS. Therefore,  $V_{\text{defect}}$  can be calculated using the formula:

$$\Delta V_{\text{defect}} = \Delta V_{\text{h}} - \Delta V_{\text{hole}}. \quad (4.3)$$

As shown in figure 4.3(d), 4.3(e) and 4.3(f),  $\Delta V_{\text{defect}}$  decreased significantly from 11.5 to 2.2 V when the IGZO deposition temperature was increased from RT to 150°C. However, when the IGZO deposition temperature was further increased to 220°C,  $\Delta V_{\text{defect}}$  decreased slightly from 2.2 to 1.7 V as shown in inset figure 4.3(f). These results imply that a high deposition temperature of the IGZO channel reduced defect generation in the TFT under NBIS. No direct evidence has been presented that the creation of ionized oxygen vacancies defect is the cause of the NBIS degradation mechanism [79]. However, we have reported previously that generated defects under NBIS were stabilized by captured electrons [70] and were drifted by lateral electric field [108]. Chowdhury et al have reported that double-donor was created in the IGZO channel

during NBIS [79]. These results strongly suggest that the creation of ionized oxygen vacancies ( $V_O^+$ ,  $V_O^{2+}$ ) is one of the reasons for TFT degradation under NBIS. Therefore, one plausible reason for the decrease in  $\Delta V_{\text{defect}}$  observed here is a reduction in oxygen vacancies in the IGZO channel. Calculation results indicated that hydrogen can passivate  $V_O$  resulting in improve NBIS stability of IGZO-TFT [109]. The passivated  $V_O$  could be reactivated by annealing at a temperature higher than 200°C. However, in this work, before evaluation of electrical properties and reliability, IGZO-TFTs were annealed at 350°C. Therefore, the correlation between hydrogen in the IGZO channel and NBIS reliability of TFT is not clear at present.

To investigate the relation between film density and defect generation in the IGZO channel under NBIS, X-ray reflectivity (XRR) measurement was performed. Figures 4.5(a) and 4.5(b) respectively show the XRR data and XRD spectra of IGZO thin films deposited at different temperatures. Figure 4.5(a) shows that the critical angle for total reflection ( $\theta_c$ ) of the IGZO film deposited at 220°C was higher than that of the films deposited at RT and 150°C. The film density of the IGZO film deposited at RT was 6.0 g/cm<sup>3</sup>. When the deposition temperature was increased from RT to 150 and 220°C, the IGZO film density increased from 6.0 to 6.4 and 6.5 g/cm<sup>3</sup> respectively. It has been reported that the densification of IGZO film reduced bulk defects above Fermi-level in the TFT channel [110]. However, this result also indicates that the densification of the IGZO film reduces bulk defects below Fermi-level in the TFT channel as well. The XRD spectra in figure 4.5(b) shows that the amorphous IGZO film was obtained when the film was deposited below 100°C. When the deposition was further increased, the peak at  $2\theta \sim 25$  deg appeared in the XRD spectra. This indicates that, an IGZO film was started to crystallize. A nanocrystalline IGZO thin film was obtained. This result explained for the increasing the film density mentioned above. When the IGZO deposition temperature was increased from RT to 150°C, the IGZO film changed from amorphous state to nanocrystalline state. As a result, the film density dramatically increased from 6.0 to 6.4 g/cm<sup>3</sup>. However, when the deposition temperature was increased from 150°C to 220°C, the structure of IGZO thin film did not considerable change. Consequently, the film density slightly increased from 6.4 to 6.5 when the deposition temperature was increased from 150°C to 220°C.

The results of the film characterizes measurements (XRD, XRR) and of NBIS reliability evaluation using positive gate pulse mode indicates that increasing the channel density or using

nanocrystalline IGZO as a channel could inhibit the defect generation in IGZO TFT under NBIS. As a result, the stability of IGZO TFT under NBIS could be improved.

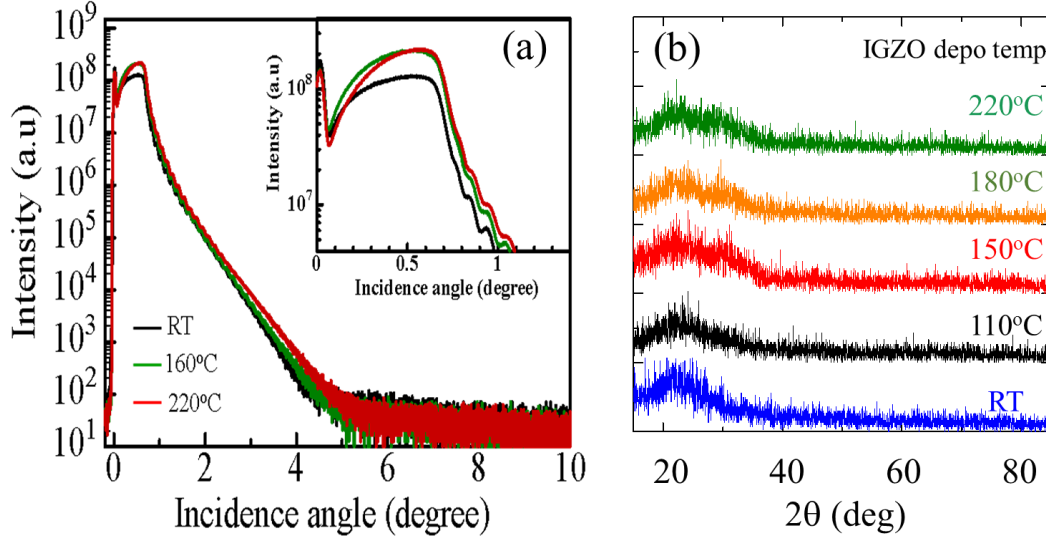


Figure 4. 5:(a) XRR data, (b) XRD spectra of IGZO thin films deposited at different temperatures.

In the discussion above, we discussed about the effect of the channel density on the defect generation in IGZO TFT under NBIS. From now on, we will investigate the effect of the channel density on the electron trapping at the back channel interface. As shown in figure 4.3(a), 4.3(b) and 4.3(c),  $V_{rev}$  of TFT-1, TFT-2 and TFT-3 were 18.2, 9.6 and 7.9 V, respectively. Since trapped electrons at the back channel interface caused the positive shift in  $V_{rev}$  [70], a large positive  $V_{rev}$  shift in TFT-1 after  $10^4$  s NBIS indicates that the back channel interface in TFT-1 was less well formed than those in TFT-2 and TFT-3. It is known that higher sputtering temperature increases mobility of adatom on the surface, resulting in higher film density and lower weak-bonding in the film. The weak bonding could have been broken to form the oxygen vacancy defects by ion bombardment during ES deposition. Therefore, the oxygen vacancy defects in TFT-1, which were created by ES deposition process, were higher than those in TFT-2 and TFT-3. This result could also explain the dependence of  $\Delta V_{defect}$  on IGZO deposition temperature mentioned above. We would like to note that separating  $\Delta V_{hole}$  and  $\Delta V_{defect}$  from  $\Delta V_h$  is valuable for further progress in the work to improve NBIS reliability of IGZO TFTs. In the case of TFT-3, after  $10^4$  s NBIS, since  $\Delta V_{hole}$  was 6.5 V while  $\Delta V_{defect}$  was only 1.7V, the

contribution of  $\Delta V_{\text{hole}}$  to the hysteresis was 80 percent. Therefore, in future work to improve the NBIS reliability of this TFT, reducing  $\Delta V_{\text{hole}}$  has stronger effect than reducing  $\Delta V_{\text{defect}}$ .

#### 4.3.3 Effect of stress temperature on the NBIS stability of IGZO TFT

As we investigated in previous section, the trapped holes in the GI contributed 80 % of the hysteresis instability in IGZO TFT under NBIS. Therefore, a reduction of the hole trapping in the IGZO TFT under NBIS will significantly improve the NBIS reliability of IGZO TFT. Increase the potential barrier for hole trapping at the GI/IGZO interface is a simple way to reducing the trapped hole. However, it is difficult to evaluate the energy barrier for hole trapping if the effects of trapped holes and generated defects on the NBIS instability were not separated.

In this section, we will use PGPM to separate the effects of trapped holes and of generated defects on the NBIS instability. The potential barrier for hole trapping in at the GI/IGZO interface will be calculated by studying the effect of stress temperature on IGZO TFT (TFT-3) under NBITS. Figures 4.6(a), 4.6(b), and 4.6(c) respectively display TFT-3 transfer characteristics after  $10^4$  s NBITS measured using DSM and PGPM at stress temperatures of RT, 35 and 50°C. The durations of the hystereses in TFT-3, which were measured by DSM and PGPM at the different stress temperatures, are shown in figure. 4.6(d), 4.6(e) and 4.6(f). Both  $\Delta V_{\text{hole}}$  and  $\Delta V_{\text{defect}}$  increased with stress temperature. However, stress temperature had a greater enhancement effect on  $\Delta V_{\text{hole}}$  than on  $\Delta V_{\text{defect}}$ . After  $10^4$  s NBIS,  $\Delta V_{\text{hole}}$  increased from 6.5 to 9.6 V and  $\Delta V_{\text{defect}}$  increased from 1.7 to 2.9 V when the stress temperature was increased from RT to 50°C as shown in inset figure 4.6(e). The  $\Delta V_{\text{hole}}$  - stress time curves at different temperatures were well fitted to the commonly used stretched-exponential equation [87]

$$\Delta V_{\text{hole}} = \Delta V_{\text{hole0}} \left\{ 1 - \exp \left[ - \left( \frac{t}{\tau} \right)^\beta \right] \right\}$$

where  $\Delta V_{\text{hole0}}$  is the approximate effective voltage drop across the gate insulator and equals  $\Delta V_{\text{hole}}$  at infinity time,  $\tau = \tau_0 \exp (E_\tau / kT)$  represents the characteristic trapping time of carriers in which  $\tau_0$  is the thermal pre-factor, thermal activation energy is given by  $E_a = E_\tau \beta$  ( $\beta$  is the stretched-exponential exponent and  $E_\tau$  is the average effective energy barrier that electrons in the a-IGZO TFT channel need to overcome to enter the insulator). Insert figure 4.6(f) shows characteristic trapping time and stretched-exponential exponent as a function of reciprocal stress

temperature. The calculated average effective energy barrier ( $E_{\tau}$ ) was 0.39 eV. The average effective energy  $E_{\tau}$  depends strongly on fabrication conditions and the GI/IGZO interface property.

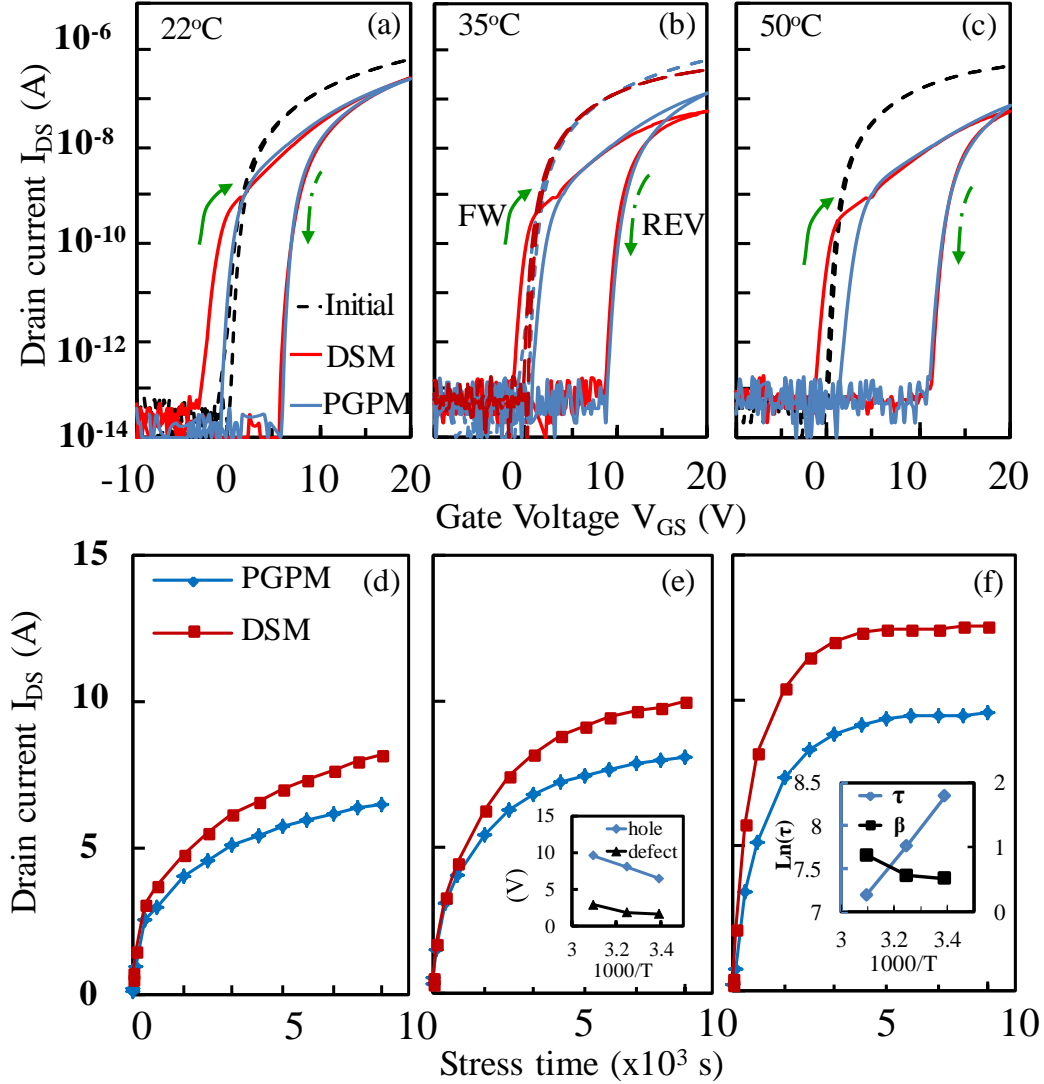


Figure 4. 6: Transfer characteristics of TFT-3 after  $10^4$  s NBITS at different temperatures (a)

RT, (b) 35°C, and (c) 50°C. The durations of TFT-3 hysteresis under NBIS at difference temperatures (d) RT, (e) 35°C (Inset shows dependence of  $\Delta V_{\text{defect}}$  and  $\Delta V_{\text{hole}}$  on NBITS stress temperature), and (f) 50°C (Inset shows the value of  $\beta$  and  $\ln(\tau)$  as a function of NBITS stress temperature).

#### **4.4 Summary**

In this chapter, the double sweeping mode and positive gate pulse mode were used to quantitative analysis the effects of hole trapping and of defect generation on the NBIS instability in IGZO TFT. The positive gate pulse mode and double sweeping mode were used to separately measure  $\Delta V_{\text{hole}}$  and  $\Delta V_{\text{defect}}$ . XRD and XRR was used to evaluate the influence of deposition temperature on structure and film density of IGZO channel. SIMS was used to estimate effects of deposition temperature on composition of IGZO channel. It was found that the density of IGZO channel and the relative hydrogen concentration was increased with IGZO deposition temperature. An amorphous IGZO film was obtained when the deposition temperature was lower than 150°C. The nano-crystalline IGZO film was obtained when the deposition temperature was higher than 150°C. The reliability of IGZO TFT under NBIS improved with the deposition temperature of IGZO channel. We also found that the densification of the IGZO channel reduced bulk defects below Fermi level in the channel, resulting in the reduction of hysteresis in IGZO TFT under NBIS. The densification of the channel also reduced the damage at the back channel interface which was a result of the etching stopper deposition process. As a consequence, the electron trapping at the back channel interface was reduced. The effects of stress temperature on the reliability of IGZO TFT under NBITS was also investigated. Stress temperature (in NBITS test) had a stronger effect on the hole trapping in a GI than on the defect generation in the IGZO channel. The time dependence of  $\Delta V_{\text{hole}}$  was well fitted to the commonly used stretched-exponential equation at different stress temperatures. As a result of separating  $\Delta V_{\text{hole}}$  and  $\Delta V_{\text{defect}}$  work, the average effective energy barrier of 0.39 eV was calculated. The effective energy barrier for hole trapping is an importance information for the work to improve the NBIS reliability because as discovered in chapter 3, the hole trapping is the dominant reason for the NBIS instability.

### ***5.1 Introduction***

In chapter 4 we considered the effect of channel on the NBIS reliability of IGZO TFT. The positive gate pulse mode and double sweeping mode were used to quantitatively analyze the effects of hole trapping and of defect generation on the NBIS instability in IGZO TFT. The results imply that increasing the film density of IGZO channel reduces the defect generation and as a consequence, improve the NBIS stability. Since IGZO is a chemically reactive material, the electrical properties and reliability of IGZO TFT are strongly affected by the post-fabrication process. In this chapter, we will study the effects of etching stopper deposition condition on the NBIS reliability of IGZO TFT.

It has been reported that the back channel interface quality strongly affects the initial properties and reliability of IGZO TFTs. In 2010, Y.Shinhyuk et. al. reported that the subthreshold swing and NBIS reliability was significantly improved by using Plasma-Enhanced Atomic Layer Deposition (PEALD) derived  $\text{AlO}_x$  as a passivation layer [111]. By studying the effects of device configuration on NBIS reliability, Jang.Y.K et. al showed that a TFT with etch stopper configuration has better electrical properties and NBIS reliability than a TFT with channel etch configuration. The TEM image of the back channel interface illustrated that the back channel interface in etch stopper type TFT was better than that in back channel etch type TFT. The etching stopper has been introduced to prevent the plasma induced damage and suppress the formation of interfacial by products onto the IGZO layer during the patterning process of source and drain electrodes [112]. In 2011 Kenji Nomura et. al. reported that the NBIS reliability of IGZO TFT was significantly improved by using a  $\text{Y}_2\text{O}_3$  passivation layer [77]. The reduction of near valence band maximum state at the back channel interface was suggested as a reason for the NBIS stability improvement. To reduce the damage at the back channel interface that is induced by post fabrication process, an organic material (CYTOP) has been used as a passivation layer [113]. Time of flight secondary ion mass spectroscopy (TOF SIMS) has been conducted to investigate the channel film composition. It has been found that the In, Ga, Zn ion intensity was relatively smaller and hydrogen ion intensity was higher at the back channel interface of the  $\text{SiO}_x$  passivated TFT [113]. However, there was no difference in the relative ion



intensity ratio between bulk and back channel interface in the CYTOP passivated TFT. As a result, the electrical properties and reliability of the CYTOP passivated TFT significantly improved. In 2013, cathode luminescence (CL), ultraviolet photoelectron spectroscopy (USP) measurement showed that the band bending surface was observed at the back channel [114]. However, due to the lack of a measurement method that can separate the effect of hole trapping and defect generation on the NBIS instability, the effect of back channel interface on the hole trapping and on the defect generation was not quantifiable. On the other hand, as we discussed in chapter 3, the trapped electron at the back channel interface is a reason for the NBIS instability in IGZO TFT. In this chapter, we will investigate the effects of the back channel interface on the defect generation and on electron trapping at the back channel interface. The quality of back channel interface was varied by the PE-CVD plasma power of SiO<sub>x</sub> etching stopper (ES) deposition.

## **5.2 Experimental**

Bottom-gate top-contact type a-IGZO TFT was fabricated on a glass substrate following the process described in chapter 3, with the exception of etching stopper deposition condition. A plasma power of SiO<sub>x</sub> etching stopper deposition in this experiment was varied as 40 W (TFT-1), 50 W (TFT-2) and 55 W (TFT-3). A light intensity of 0.2 mW/cm<sup>2</sup> with a wavelength of 460 nm and a gate bias voltage of -40 V was applied in NBIS test. DSM and PGPM were used to measure the transfer characteristic of a-IGZO TFT.

## **5.3 Results and Discussions**

### *5.3.1 Effects of ES deposition conditions on the initial properties*

Figures 5.1(a), 5.1(b), and 5.1(c) show the transfer characteristics of TFT-1, TFT-2 and TFT-3, respectively. The initial properties of 3 TFTs are listed in table 5.1. S<sub>s</sub> values of all TFTs fluctuated between 0.35 and 0.38 V/decade. However, electron mobility increased from 11.6 to 13.2 cm<sup>2</sup>/V·s and V<sub>th</sub> decreased from 2.8 to 2.1 V when the plasma power of the etching stopper deposition process was increased from 40 to 55 W. The decrease in V<sub>th</sub> that was observed with the additional plasma power indicates that carrier concentration in the channel was increased with the plasma power of etching stopper deposition process. The hydrogen and oxygen vacancy (V<sub>O</sub>) are known as the electron supplier in IGZO material. As we mentioned in chapter 4, hydrogen not only acts as a donor in IGZO but also as a carrier scattering point. Therefore,

carrier mobility will decrease when the concentration of hydrogen in IGZO increases. In this experiment, the carrier concentration and mobility increased when the plasma power of etching stopper deposition process was increased. Therefore, the reason for the decreasing  $V_{th}$  and increasing carrier mobility could be an increasing  $V_O$  in the channel. Since IGZO has a conducting path located about 0.03-0.1 eV above  $E_C$ , mobility in IGZO will increase when the carrier concentration increases [39], [40].

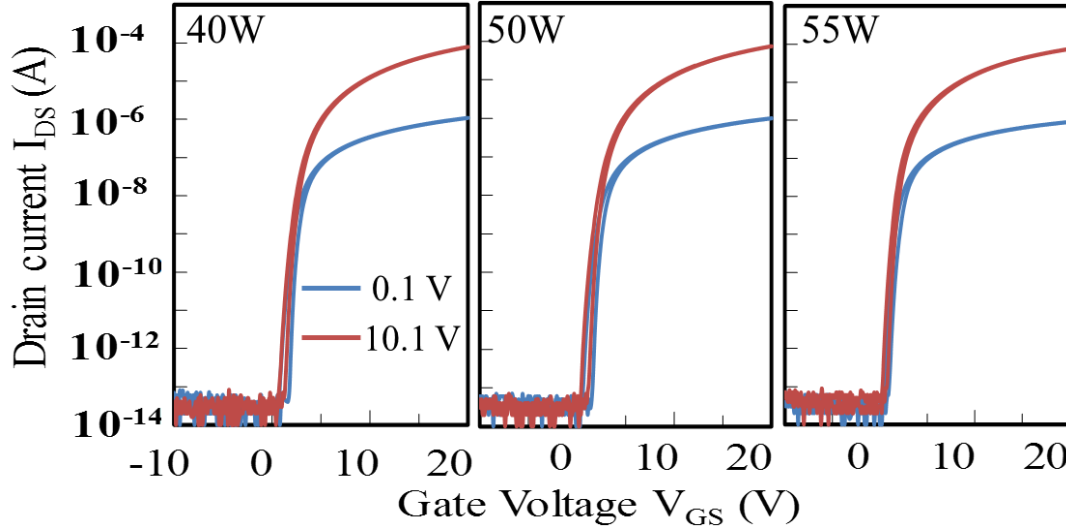


Figure 5. 1: Transfer characteristic of (a) TFT-1, (b) TFT-2, (c) TFT-3.

Table 5. 1: Summary the electrical properties of TFT-1, TFT-2, TFT-3 at the initial state.

ES deposition power	S.S (V/dec)	$V_{th}$ (V)	$\mu$ (s/V•cm)
<b>40W (TFT-1)</b>	0.38	2.8	11.6
<b>50W (TFT-2)</b>	0.38	2.4	12.5
<b>55W (TFT-3)</b>	0.35	2.1	13.2

### 5.3.2 Quantitative Effects of ES deposition conditions on NBIS stability of IGZO TFT

Figures 5.2(a), 5.2(b), and 5.2(c) respectively show the transfer characteristics of TFT-1, TFT-2, and TFT3, which were measured by single sweeping mode and positive gate pulse mode at NBIS stress time of  $10^4$  s.  $\Delta V_{rev}$  of TFT-1, TFT-2, and TFT-3 after  $10^4$  s NBIS was 2.4, 7.5, 13.6 V, respectively. The positive shift in the reverse curve enhanced with the plasma power. As

discussed in chapter 3 and chapter 4, the electron trapping at the back channel interface caused a positive shift in reversed curve. Therefore, the enhancement of the positive shift, which is shown in figure 5.2(a), 5.2(b), and 5.2(c), implies that the back channel in TFT-3 was less well formed than that in TFT-1. This suggests that the etching stopper deposition condition, particularly in the plasma power of etching stopper deposition process, strongly affected the quality of the back channel interface.

We also used positive gate pulse mode and double sweeping mode to quantitatively analyse the effects of the plasma power of etching stopper deposition process on the hole trapping and defect generation in IGZO TFT under NBIS. Figures 5.2(c), 5.2(d), and 5.2(e) represent the hysteresis induced by trapped holes at the front channel interface and by generated defects in the channel. The hysteresis induced by the generated defects increased from 0.9 to 3.3 V when the plasma power was increased from 40 to 50 W. The hysteresis induced by the generated defects was further increased to 4.7 V when the plasma power was raised to 55 W. These results suggest that etching stopper deposition conditions had a strong impact on defect generation in IGZO TFTs under NBIS. As we pointed out in the last paragraph, increasing the plasma power reduced the quality of back channel interface. Therefore, the increasing hysteresis induced by the generated defects implies that there is a strong correlation between back channel interface qualities and defect generation in IGZO TFT under NBIS. In other words, by separating the effects of hole trapping and defect generation on the NBIS induced hysteresis, we confirmed that the defects were mainly generated at the back channel interface. The etching stopper deposition conditions not only influence defect generation in the channel but also electron trapping at the back channel interface. Therefore, in the work to improve the NBIS stability, the etching stopper deposition condition needs to be optimized.

In spite of the hysteresis induced by generated defects, the hysteresis induced by trapped holes at the front channel interface was 2.9 V regardless of the plasma power of etching stopper deposition process. The energetic bombardment of negative oxygen ion, which was accelerated by the applied electric field between the substrate and the target in DC magnetron sputtering, was found to be the reason for the GI/channel interface damage [106], [107]. In this work, the gate insulator and channel in all TFT was deposited under the same conditions. Therefore, the qualities of IGZO/GI interface are assumed to be the same for all TFTs. On the other hand, it is

also well established that trapped carriers at the front channel interface are mainly determined by gate bias stress and the front channel interface quality [87], [88]. At the same gate voltage stress and IGZO/GI interface quality, the hole trapping at front channel interface are approximately equal for all TFTs. As a result, hystereses measured using positive gate pulse mode from TFT-1, TFT-2 and TFT-3 were almost identical. Since the measurement results are in good agreement with the theoretically predicted results; positive gate pulse mode can be used for an estimation of  $\Delta V_{\text{hole}}$  in the IGZO TFT under NBIS. This result and the result shown in chapter 4 are evidence that the positive gate pulse mode and double sweeping mode can be used to accurately quantitatively analyse the effect of hole trapping and of defect generation on the NBIS instability in IGZO TFT.

#### ***5.4 Summary***

In this chapter, double sweeping mode and positive gate pulse mode were used to investigate the effects of plasma power of etching stopper deposition process on the NBIS instability in IGZO TFT. It was found that the plasma power of etching stopper deposition process strongly affected the initial characteristics and NBIS reliability of IGZO TFTs. The field effect mobility of IGZO TFT increased but TFT threshold voltage decreased with the plasma power of etching stopper deposition process. The NBIS reliability improved when the plasma power was increased. The plasma power of PECVD in etching stopper deposition process created some damage at the back channel interface. Under NBIS, the defects were mainly generated at the back channel interfaces and defect generation could be controlled by the etching stopper deposition conditions. The results in this chapter further our thesis that hole trapping at the front channel interface is the main cause of the NBIS instability in IGZO TFT. Therefore, in following chapter we will discuss the hole trapping mechanism and the method to significantly improve the NBIS stability of IGZO TFT.

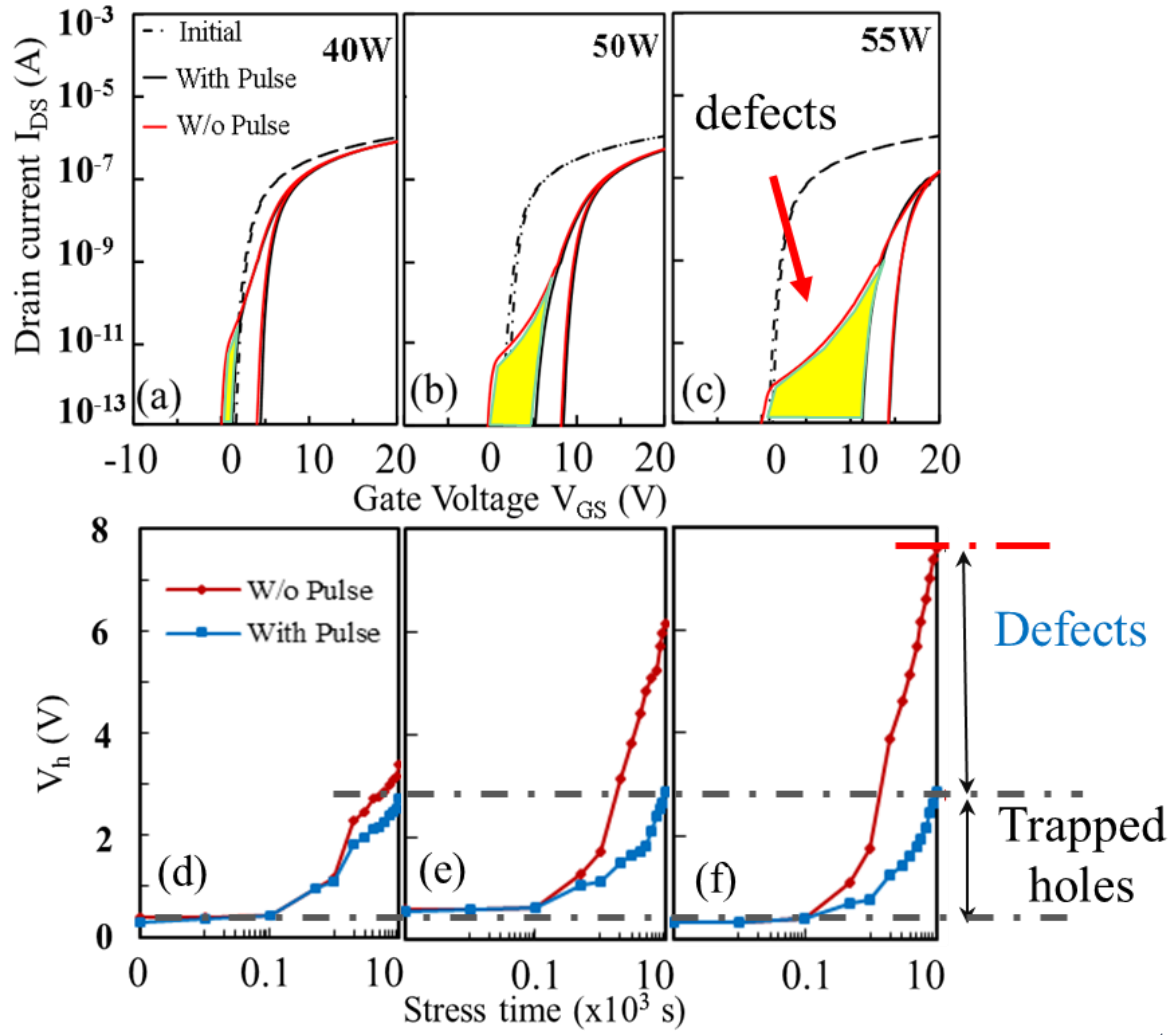


Figure 5. 2: Figure 4. 7: Transfer characteristic of (a) TFT-1, (b) TFT-2, (c) TFT-3 after  $10^4$  s NBIS measured using double sweeping mode and positive gate pulse mode, and duration of hysteresis detected using double sweeping mode and positive gate pulse mode in (d) TFT-1, (e) TFT-2, (f) TFT-3 under NBIS

### **6.1 Introduction**

As we discussed in previous chapters, the trapped holes in gate insulator [67], [74], [75], [90], the generated ionized oxygen vacancies ( $V_o^+$ ,  $V_o^{2+}$ ) and created defects in the channel are widely accepted as reasons for the NBIS instability [76]–[80], [105]. To date, material approach has been applied to improve the NBIS stability. The trapped holes could be reduced by a GI material which has high hole trapping barrier such as  $SiO_x$  or  $AlO_x$  [115]. A  $TiO_2$  film which acts as hole carrier blocking layer was also used to inhibit the hole trapping [116]. High pressure water [91], [92], wet  $O_2$  annealing [93],  $Y_2O_3$  passivation layer [77]... have been used to passivate  $V_O$  defects. However, suppressing  $V_O$  defects in amorphous IGZO remains a challenge due to high density of state of  $V_O$  defects in IGZO. Therefore, a new approach is needed to achieve highly reliability IGZO TFT under NBIS. To do that, the detail of the NBIS degradation mechanism is required to be investigated. In this chapter, the NBIS degradation mechanism was clarified by investigating the effect of negative pulse duration in AC gate bias and of incident light intensity on the NBIS degradation behavior. Based on a investigated hole generation mechanism, a control algorithm was proposed to improve the NBIS stability.

### **6.2 Experimental**

Bottom-gate top-contact IGZO TFTs with a channel width/length of 800  $\mu m$ /160  $\mu m$  were fabricated on a glass substrate. Detail of the fabrication process is shown in figure 6.1. 50-nm-Cr gate electrodes were deposited on the substrate by DC-sputtering and then patterned by wet-etching. A stack 160-nm- $SiNx:F$ /50-nm- $SiO_x$  GI was deposited by Inductively Plasma-Enhanced Chemical Vapor Deposition (ICP-CVD)/Plasma-Enhanced Chemical Vapor Deposition (PE-CVD), respectively. 45-nm-IGZO channels were deposited on the GI by DC-sputtering and then patterned by dry-etching. A 200-nm- $SiO_x$  etching-stopper was subsequently deposited by PE-CVD. 50-nm Indium Tin Oxide (ITO) source/drain electrodes were deposited by DC-sputtering and then patterned by dry-etching. A 200-nm- $SiO_x$  passivation layer was then deposited by PE-CVD. After that the devices were annealed for 1 hour in  $N_2$  ambient at 350°C. The electrical properties and reliability of IGZO TFT were evaluated using an Agilent 4156C semiconductor

analyzer. A gate bias stress of -30 V with blue light ( $\lambda = 460$  nm) at a power density of 0.2 mW/cm<sup>2</sup> was applied in NBIS testing.

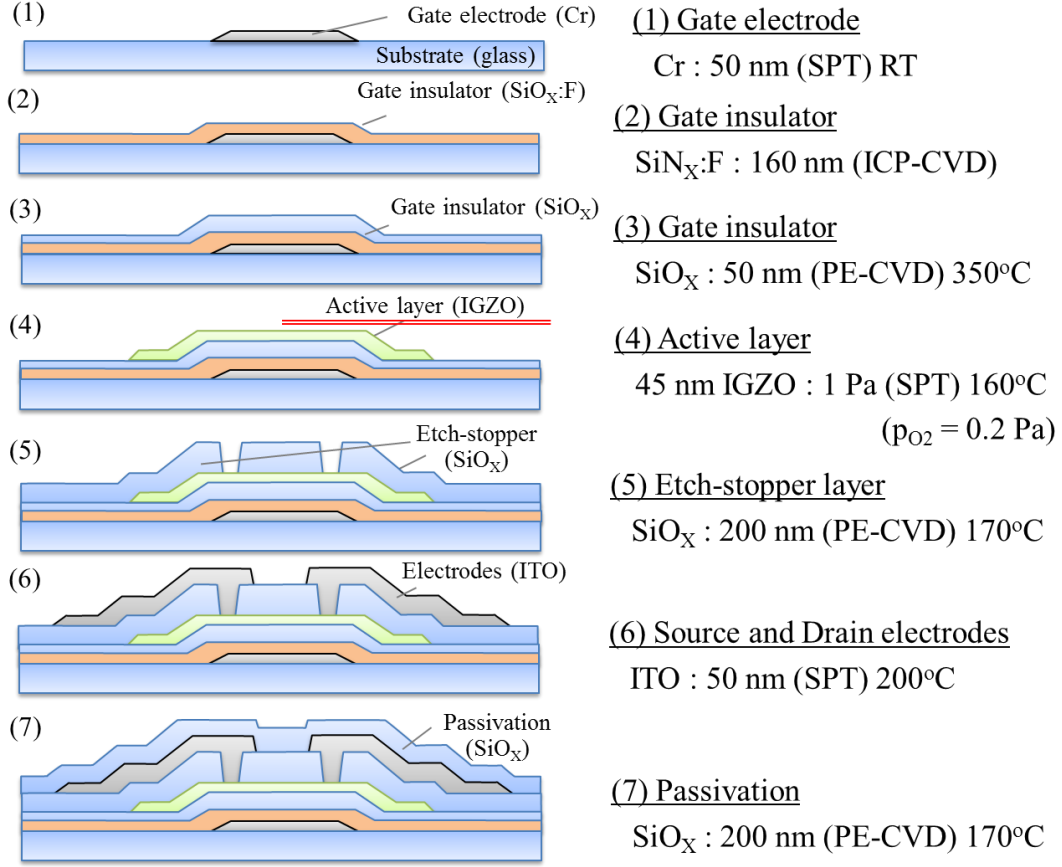


Figure 6. 1: Fabrication process of IGZO TFTs with a SiN<sub>x</sub>:F/SiO<sub>x</sub> gate stack layer

## 6.3 Results and Discussions

### 6.3.1 Effects of Positive gate pulse on the NBIS stability of IGZO TFT

Figure 6.2 shows the initial transfer characteristic ( $I_D - V_G$ ) of IGZO TFT measured by double sweeping mode at a drain voltage  $V_D$  of 0.1 and 10.1 V. The linear mobility was ~19 cm<sup>2</sup>/Vs. Threshold voltage ( $V_{th}$ ) of ~6 V is defined as the gate voltage at drain current  $I_D = 1$  nA. Subthreshold swing (Ss value) of ~0.2 Vdec<sup>-1</sup> is defined as the gate voltage required to increase  $I_D$  from 0.1 to 1 nA. Hysteresis ( $V_h$ ) is defined as the difference in  $V_{th}$  between forward ( $V_{fw}$ ) and reverse ( $V_{rev}$ ) sweeps. The  $V_h$  at initial state was 0.2 V.

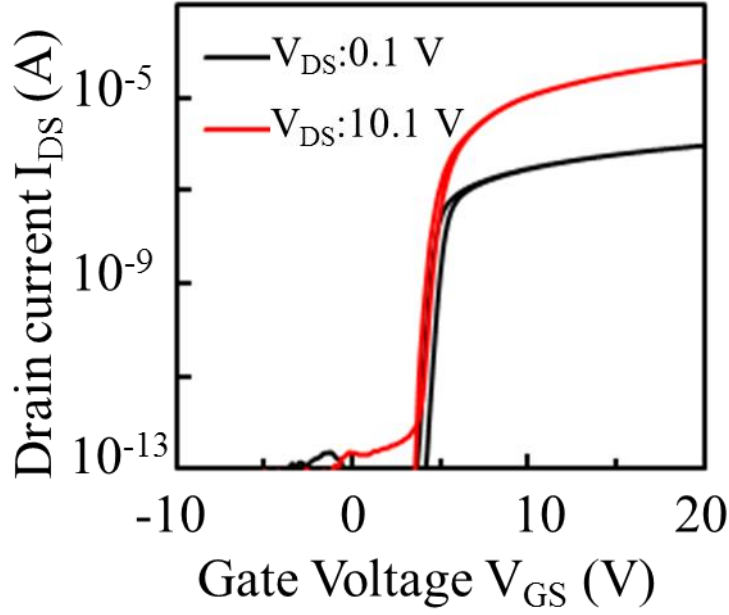


Figure 6. 2: Initial transfer characteristic of IGZO TFT with stack gate insulator

Figure 6.3(a) shows the change in the TFT's transfer characteristics as measured by the single sweeping mode under DC-NBIS. The transfer curve shifted -4.3 V (in negative direction) with Ss degradation. The Ss degradation indicates that the defects were created in the TFT. To further investigate the reason for this negative shift in transfer curve, a positive gate pulse mode (PGPM) was conducted [90], [105]. The PGPM is a transfer characteristic measurement method in which a positive gate pulse is applied to the TFT prior to transfer characteristic measurements. As we discussed in previous report [105], a positive gate pulse not only stabilizes the created defects but also detraps holes from the GI. Therefore, in order to stabilize the created defects and to minimize the hole detrapping from the GI, a positive gate pulse with a pulse width of 1 ms and a pulse high of 10 V was chosen. Figure 6.3(b) shows the change in the TFT's transfer characteristics measured by PGPM as a function of the NBIS duration. The transfer characteristics measured by the PGPM negatively shifted without Ss degradation. Based on the results of our previous work [78], [105], the created defects are the ionized types of oxygen vacancies ( $V_O^+$ ,  $V_O^{2+}$ ). The positive gate pulse causes electron to accumulate in the channel. The  $V_O^+$ ,  $V_O^{2+}$  are simultaneously stabilized by capturing the accumulated electrons. As a result, the Ss value did not degrade in the transfer curve measured by PGPM. As a consequence of the  $V_O^+$ ,  $V_O^{2+}$  stabilization, trapped holes in the GI caused a negative shift in the transfer curve as measured by PGPM. The threshold voltage shift ( $\Delta V_{th}$ ) at  $10^4$  s DC-NBIS measured by PGPM



was -3.6 V. The results and discussions above indicate that the trapped holes in the GI and created defects ( $V_O^+$ ,  $V_O^{2+}$ ) in the TFTs are reasons for the  $V_{th}$  instability in the IGZO TFT under DC-NBIS. It also shows that  $\Delta V_{th}$  at the DC-NBIS duration of  $10^4$  s increased from -4.3 to -3.6V when the positive gate pulse was applied prior to transfer characteristic measurement. This mean that the NBIS stability in IGZO TFT improved by applying a positive gate pulse. This improvement in the NBIS stability is caused by the defect stabilization.

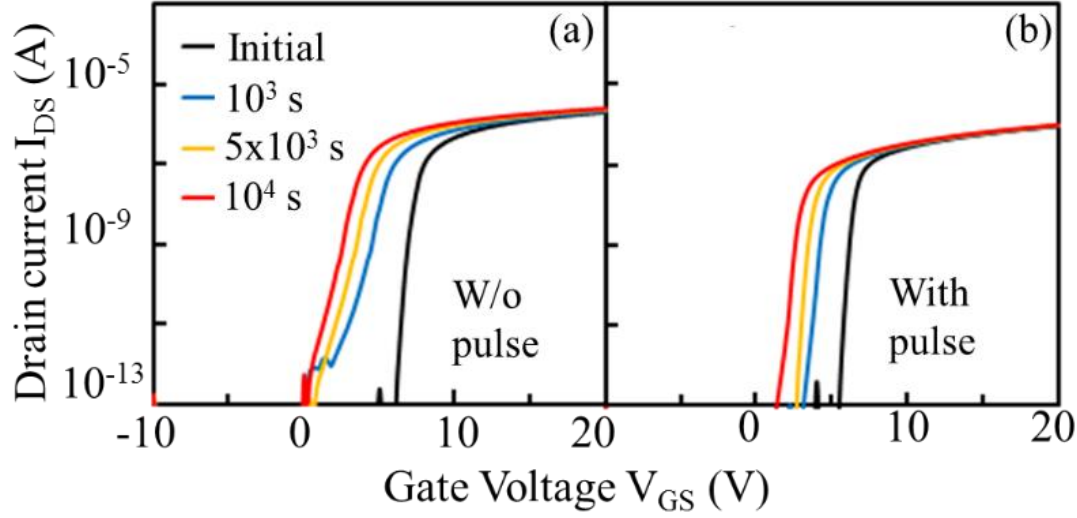


Figure 6. 3: Change in transfer characteristic of IGZO TFT under DC-NBIS measured by (a) single sweeping mode, and (b) positive gate pulse mode.

In order to further investigate the influences of the positive gate pulse on the NBIS stability, -30 V negative gate and 10 V positive gate pulse high was alternatively applied as a gate bias stress (AC-NBIS). The positive gate pulse width was fixed as 1 ms. The negative gate pulse width was varied from 100 s to 1000 s. Table 6.1 shows gate bias conditions which were applied in AC-NBIS testing. The stress time for AC-NBIS is defined as a total negative gate pulse duration. Figures 6.4(a)-6.4(d) show the change in IGZO TFT's transfer characteristic in under AC-NBIS with a negative gate pulse width of 100, 200, 250, 500 s, respectively. In all cases, the transfer characteristic shifted negatively without a considerable change in the  $S_s$  value. This result implies that trapped holes in the GI are the main cause of the shift in TFT's transfer characteristic under AC-NBIS. Figure 6.4(e) shows the AC-NBIS stress time dependent of  $\Delta V_{th}$  for different gate bias conditions. The dependence of  $\Delta V_{th}$  at the AC-NBIS stress time of  $10^4$  s on the negative gate pulse width is shown in figure 6.4(f). The  $\Delta V_{th}$  slightly decreased from -0.6 to -0.7 V when the negative gate pulse width was increased from 100 to 200 s. However, when

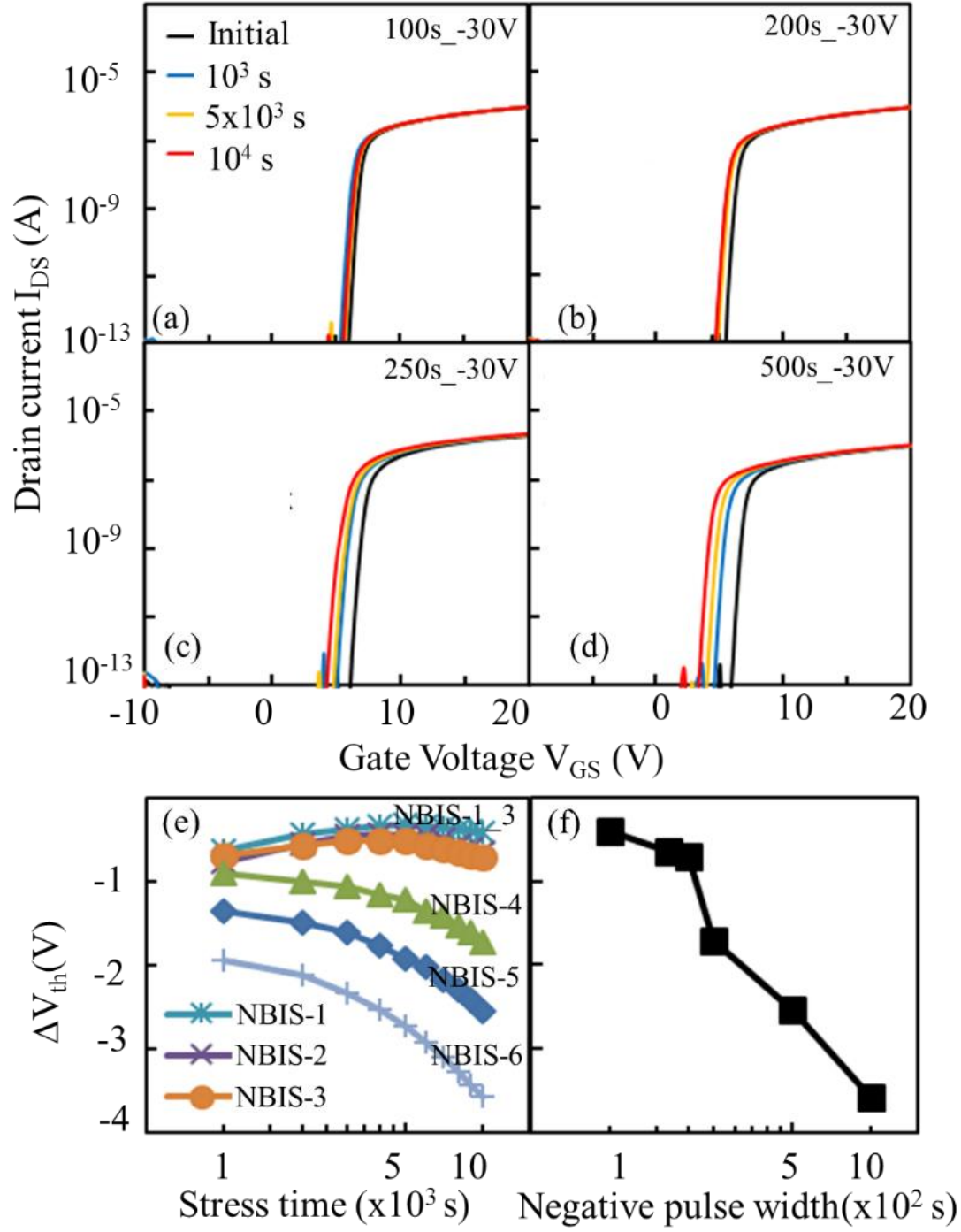


Figure 6. 4: Change in transfer characteristic under AC-NBIS with different gate bias condition; (a) NBIS-1, (b) NBIS-3, (c) NBIS-4, (d) NBIS-5. (e) the stress time dependence of  $\Delta V_{th}$  under NBIS, (f) the  $\Delta V_{th}$  at the AC-NBIS duration of  $10^4 s$  as a function of negative pulse width.

the negative gate pulse width was further increased to 250 s, the  $\Delta V_{th}$  rapidly decreased to -1.7 V. Figure 6.4(f) shows that a linear relationship between  $\Delta V_{th}$  at the AC-NBIS stress time of  $10^4$  s and logarithmic of the negative pulse width was observed. When the negative gate pulse width was varied from 100 to 200 s, the slope of  $\Delta V_{th} - \log(\text{pulse width})$  was -1. The slope increased to -3.1 when the negative gate pulse width was varied from 250 to 1000 s. This result suggests that the hole trapping barrier reduced when the negative pulse width exceeded 250 s. In previous report [75], the reliability of IGZO TFT under 25 kHz-AC-NBIS has been investigated. Cheng et. al. has suggested that due to low hole mobility in IGZO, the duration of negative gate voltage in the 25 kHz-AC gate bias stress does not provide enough time for holes to drift to the front channel interface. As a result, the TFT was stable under the 25 kHz-AC-NBIS. However, in this work the IGZO TFTs were almost stabled even though a negative gate pulse width of 200 s was used. This negative gate period may provide enough time for the holes to drift to the front channel interface. Therefore, the low hole mobility in IGZO is not enough for explain the results shown in figure 6.4(e) and 6.4(f).

### 6.3.2 Hole generation mechanism

In order to clarify the reasons that the positive gate pulse improved the gate bias illumination stress stability, we compared the transfer characteristics measured at the DC-NBIS stress time of 200 and 250 s. Figures 6.5(a) and 6.5(b) illustrate TFT's transfer characteristics measured by single sweeping mode (without applying the positive gate pulse) at a light intensity of  $0.2 \text{ mW/cm}^2$  and the DC-NBIS duration of 200 and 250 s, respectively. The TFT transfer characteristics measured by PGPM (with applying the positive gate pulse) at the stress time of 200 and 250 s are shown in figure 6.5(c) and 6.5(d), respectively. All transfer curves measured by SSM shifted negatively with an Ss degradation. The Ss degradation indicates that the  $V_O^+$ ,  $V_O^{2+}$  defect was generated. When the positive gate pulse was applied, the transfer curve recovered to the initial state in the case of DC-NBIS duration of 200 s, as shown in figure 6.5(c). This result suggests that, the  $V_O^+$ ,  $V_O^{2+}$  defects, which can be stabilized by the positive gate pulse [105], are the reason for the negative shift in transfer curve after 200 s DC-NBIS. The density of the trapped holes in the GI after 200 s DC-NBIS was not sufficient to effect the  $V_{th}$ . As a consequence, the IGZO TFT was almost stable under AC-NBIS, as shown in figure 6.4(a) and 6.4(b). By contrast, figure 6.5(d) shows that the transfer curve measured at the NBIS duration of

250 s shifted -0.3 V when the positive gate pulse was applied. This result indicates that the density of the trapped holes in the GI increased dramatically when the NBIS duration was further increased to 250 s. Consequently, the  $\Delta V_{th}$  at the AC-NBIS duration of  $10^4$  s rapidly decreased from -0.7 to -1.7 V when the negative pulse width was increased from 200 to 250 s, as shown in figure 6.4(f).

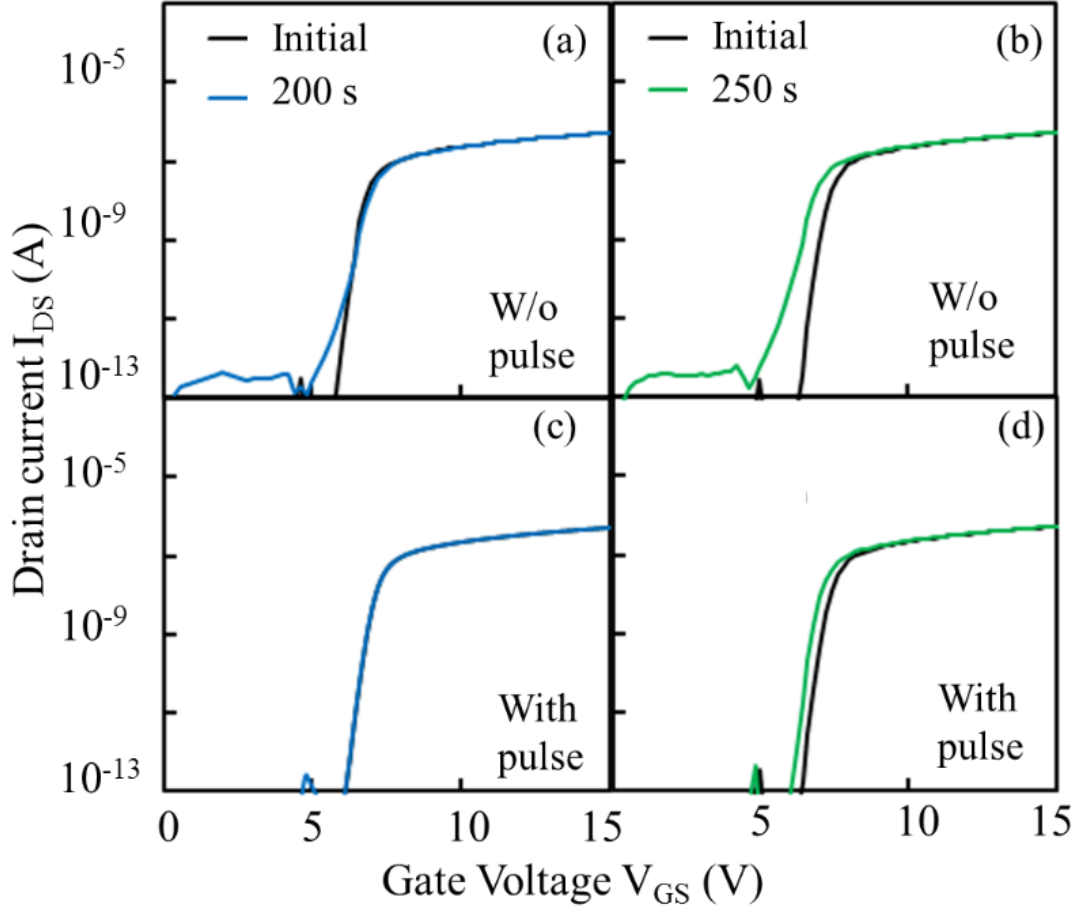


Figure 6. 5: The transfer characteristic of IGZO TFT measured before applying the positive gate pulse at light intensity of  $0.2 \text{ mW/cm}^2$  and the DC-NBIS duration of (a) 200 s, (b) 250 s. The transfer characteristic of the IGZO TFT measured after applying the positive gate pulse at the DC-NBIS duration of (a) 200 s, (b) 250 s.

In order to investigate the reason for that the density of trapped holes dramatically increased when the NBIS duration reached 250s, the effect of light intensity on the  $\Delta V_{th}$  at the stress time of 250 s was investigated. The light intensity was varied from  $0.1$  to  $0.4 \text{ mW/cm}^2$ . Figures 6.6(a) and 6.6(b) illustrate the TFT's transfer characteristics measured by SSM at the light intensity of  $0.1$  and  $0.4 \text{ mW/cm}^2$ , respectively. The TFT's transfer characteristics measured by PGPM at the

light intensity of 0.1 and 0.4 mW/cm<sup>2</sup> are shown in figure 6.6(c) and 6.6(d), respectively. When the light intensity was set as 0.1 mW/cm<sup>2</sup>, the transfer curve measured without applicant of the positive

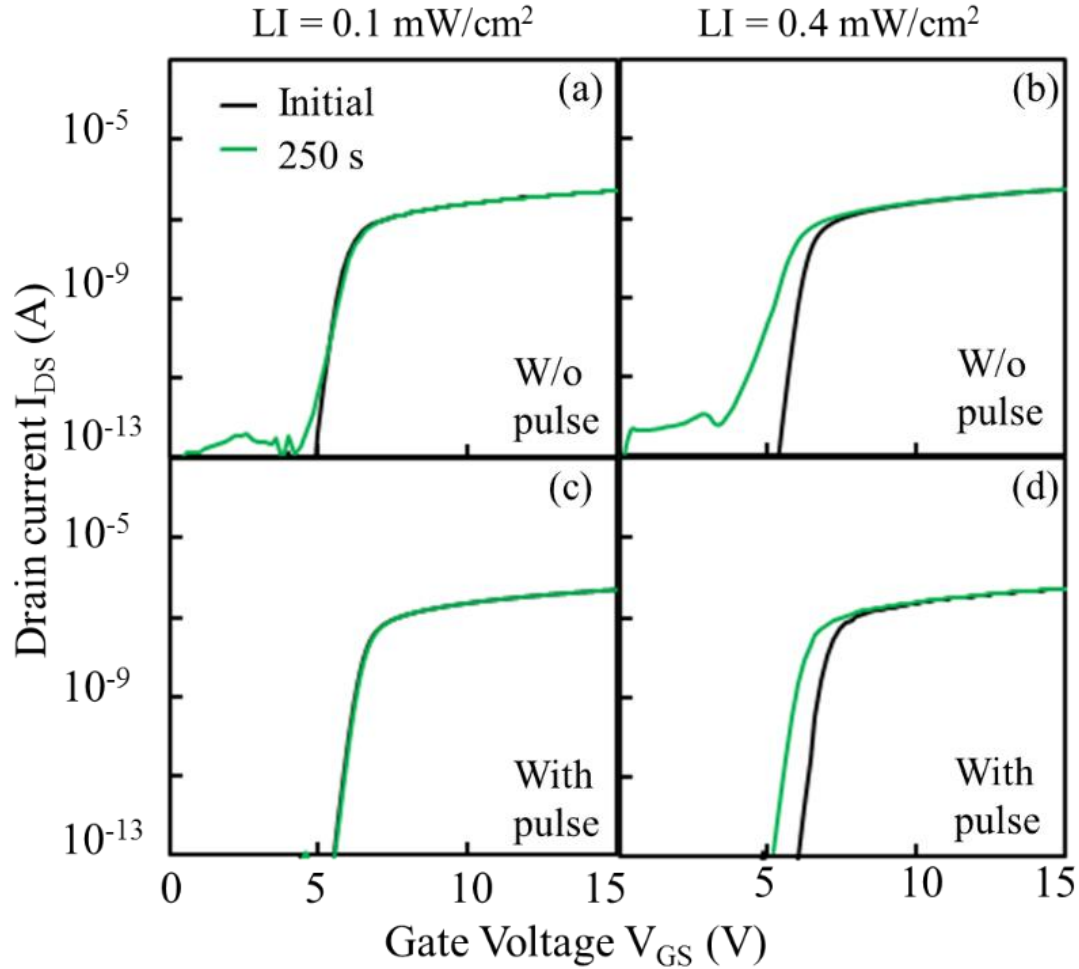


Figure 6. 6 The transfer characteristic of IGZO TFT at the DC-NBIS duration of 250 s measured before applying the positive gate pulse with a light intensity of (a) 0.1 mW/cm<sup>2</sup>, (b) 0.4 mW/cm<sup>2</sup>. The transfer characteristic of the IGZO TFT at the DC-NBIS duration of 250 s measured after applying the positive gate pulse with a light intensity of (a) 0.1 mW/cm<sup>2</sup>, (b) 0.4 mW/cm<sup>2</sup>.

gate pulse was shifted slightly. The Ss degraded at the drain current below 10 pA. The transfer curve recovered to the initial state when the positive gate voltage was applied, as shown in figure 6.6(c). This indicates that the number of trapped holes in the GI could be negligible. When the light intensity was increased to 0.4 mW/cm<sup>2</sup>, the negative shift in the transfer curve measured by SSM enhanced. The Ss degraded at the drain current below 10 nA. This result suggests that the

energy distribution of  $V_O^+$ ,  $V_O^{2+}$  increased, to a level closer to the conduction band minimum ( $E_C$ ). When the positive gate voltage was applied prior to transfer characteristic measurement, the Ss degradation vanished.  $\Delta V_{th}$  of -0.8 V was observed. The  $\Delta V_{th}$  measured by PGPM decreased from -0.3 to -0.8 V when the light intensity was increased from 0.2 to 0.4 mW/cm<sup>2</sup>, as shown in figure 6.5(d) and 6.6(d). This result indicates that the trapped holes in the GI not only depend on the negative gate voltage duration but also depend on the incident light intensity.

The influences of negative gate pulse width and of incident light intensity on trapped holes in the GI suggest the presence of a hole trapping process in the TFT under NBIS, which is shown in figure 6.7. The hole trapping process includes 2 steps: hole generation in the channel and hole injection into the GI. At the early stage of NBIS, the blue incident light ( $h\nu = 2.7$  eV) excites electrons from  $V_O$  defects (located about 2.3 eV from  $E_C$ ) to conduction band [38], [82], [108], [117], and generates  $V_O^+$ ,  $V_O^{2+}$ , as shown in figure 6.7(a). The  $V_O^+$ ,  $V_O^{2+}$  act not only as the donor-like defects but also as the midgap trap states. The incident photon then induces an optical excitation of electron from the valence band maximum to the midgap trap states, and generates free hole. The generated holes are accumulated at the front channel interface and injected to the GI under a negative gate bias stress. The detail of hole generation is illustrated in figure 6.7(b). The hole generation mechanism suggests that number of generated holes not only depends on the light intensity but also on the DOS of midgap trap states ( $V_O^+$ ,  $V_O^{2+}$ ). At the early stages, the generated hole density is low due to low emission rate of deep states in IGZO [118]. The hole trapping is limited by the hole generation step, resulting in the slope of -1 shown in figure 2(f). On the other hand, when NBIS duration was increased, the DOS of  $V_O^+$ ,  $V_O^{2+}$  exponentially increased. The probability of  $V_O^+$ ,  $V_O^{2+}$  capturing the excited electron also dramatically increased. Therefore, the hole trapping process is limited by the hole injection step, resulting in the slope of -3.1 shown in figure 6.4(f). The hole generation mechanism implies that a reduction in DOS of the midgap trap states can reduce the trapped holes in the GI, resulting in an improvement in the NBIS stability. The DOS of midgap trap states can be reduced either by suppressing deep subgap defects[77], [92], [96], by inducing recombination centers in channel (material approach)[119] or by control algorithm, as shown in this work (the driving approach). The discussions above also imply that the reliability of IGZO TFT can be significantly improved when the display is working at a high frame rate. Long refresh time is an advantage of IGZO display. However, the results of this work suggest that the long refresh time reduces the stability of IGZO display. In

order to improve the NBIS reliability and reduce the power consumption of the IGZO displays, an optimal refresh time is required.

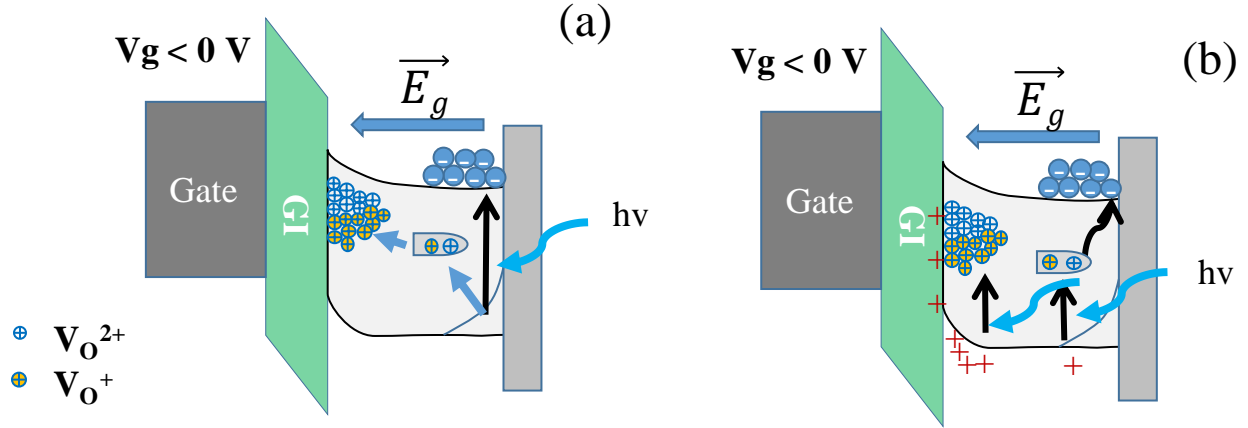


Figure 6. 7: (a) the defect generation mechanism, (b) the hole generation mechanism

## 6.4 Summary

This chapter presents a method to improve the NBIS reliability of IGZO TFT. The degradation behavior and the degradation mechanism of IGZO TFT under AC- and DC-NBIS were investigated. Effects of the negative pulse width and of light intensity on the NBIS reliability were also examined. The NBIS reliability significantly improved when either the negative pulse width was reduced or intensity of the stress light was decreased. A linear relationship between  $\Delta V_{th}$  at the AC-NBIS stress time of  $10^4 \text{ s}$  and logarithmic of the negative pulse width was observed. When the negative gate pulse width was varied from 100 to 200 s, the slope of  $\Delta V_{th} - \log(\text{pulse width})$  was -1. The slope increased to -3.1 when the negative gate pulse width was varied from 250 to 1000 s. The hole trapping in the GI was found to be the reason for the AC-NBIS instability. The created defects act as the midgap trap state for hole generation. However, these created defects are stabilized by capturing electrons. These results suggest that the NBIS reliability of IGZO TFT can be significantly improved by increasing the frame rate of FPD. The refresh time also needs to be optimized to achieve NBIS reliability.

### **7.1 Introduction**

In FPDs, a positive voltage is applied to the gate electrode when TFT is operated at the on-state. The TFTs are worked under positive bias stress (PBS). Therefore, the reliability of TFTs under PBS is required for a display application. Even though, the reliability of IGZO TFTs under positive bias stress is not so serious problem as compared with the NBIS reliability. However, the reliability of IGZO TFT under PBS also needs improvement. The PBS reliability of IGZO TFT has gathered attention of many researchers. Trapped electrons at a front channel interface or in a gate insulator (GI) have been accepted as a reason for PBS instability in an IGZO TFT. The hole trapping mechanism has suggested due to the fact that the change in  $V_{th}$  with PBS duration was well fitted to a stress exponential equation [120], [121]. Different gate dielectric materials have been used to reduce the trapped electrons, resulting in an improvement in the PBS stability. It was reported that a  $SiO_x$  and an  $AlO_x$  GI significantly improve the PBS stability of the IGZO TFT [122], [123]. Besides the electron trapping at the front channel interface, shallow traps and deep traps have also been suggested as a possible reason for the positive threshold voltage ( $V_{th}$ ) shift in an IGZO TFT under PBS [124], [125]. The acceptor-like deep traps at 1.0 eV below the conduction band minimum were introduced to simulate experimental results [124]. A study on the activation energy of electron trapping and of detrapping (recovery process) under PBS predicted creation of deep acceptor-like defects in the TFT under PBS, but the energy level of the created defects has not yet been determined [100]. Dry, wet,  $O_2$ ,  $O_3$  annealing, hydrogen, nitrogen, fluorine treatment, and titanium metal reaction methods have been used to reduce the trap sites in the bulk or at the front channel interface [92], [94], [101], [124], [126]–[130]. Nonetheless, in our best knowledge, direct evidence for the created deep defects and the energy level of the created defects has not been reported yet. This is due to the fact that the trapped electrons at the front channel interface and the created deep defects induce the same degradation behavior in transfer and C-V characteristics. Therefore, it is difficult to distinguish the effect of the trapped electrons and of the created deep defects on the PBS instability. In this work, the conductance measurement method [131] was used to investigate the effect of the post-annealing time on PBS degradation mechanism. We found that,



stabilization of the donor-like interface defects is a reason for PBS instability of the IGZO TFT. The created deep acceptor-like interface defects were identified by the trap time constant. The energy distribution and trap time constant of the acceptor-like interface defects were also extracted. The experimental results show that the PBS stability of IGZO TFTs could be improved by increasing the post-annealing time.

## 7.2 Experimental Details

The IGZO TFT fabrication process has been described in our chapter 3. Before electrical measurement and reliability evaluation, the IGZO TFTs were annealed in N<sub>2</sub> ambient at 350°C for 1 hour (sample A1) and 5 hours (sample A2). A gate bias stress of 30 V with a grounded source and drain was applied in the PBS test. The electrical properties and reliability of IGZO TFTs were evaluated using an Agilent 4156C semiconductor parameter analyzer. The capacitance, conductance and admittance was measured using a computer controlled Agilent 4980A Precision LCR Meter at frequencies ranging from 100 Hz to 2 MHz. Schematic of the measurement is shown in figure 7.1. Threshold voltage ( $V_{th}$ ) is defined as the gate voltage at a drain current ( $I_D$ ) of 1 nA. Subthreshold swing, which is extracted near the  $V_{th}$  region, is defined as the gate voltage required to increase  $I_D$  from 0.1 to 1 nA.

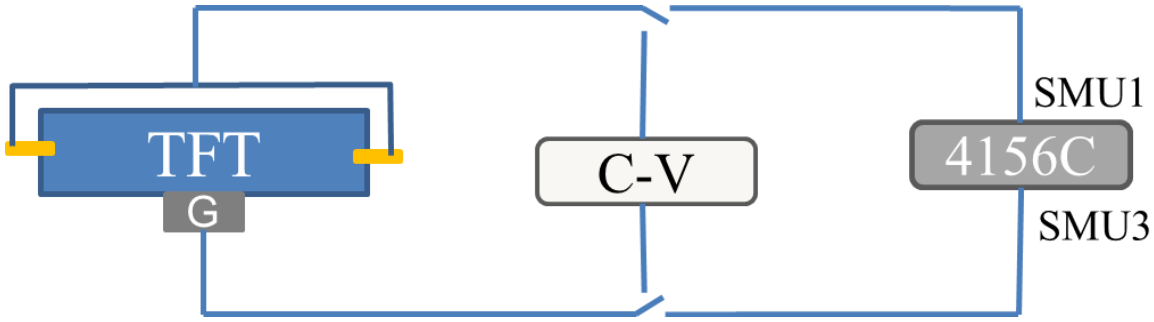


Figure 7. 1: Schematic diagram of the PBS testing and conductance measurement

## 7.3 Results and Discussion

### 7.3.1 Effect of Post-Annealing Time on Initial Transfer Characteristic and Positive Bias Stress Stability

Figure 7.2(a) and 7.2(b) show the transfer characteristics of the sample A1 and A2, respectively. The change in transfer characteristic of the sample A1 and A2 under PBS are shown in figure 7.2(c) and 7.2(d), respectively.  $V_{th}$  of ~1.3 V, mobility of ~12 cm<sup>2</sup>/Vs, and Ss

value of  $\sim 0.1 \text{ Vdec}^{-1}$  were not considerably different between sample A1 and A2. This result indicates that the front channel interface quality of sample A1 is similar to that of sample A2. The effect of post-annealing time on the initial properties of IGZO TFTs can be negligible. In spite of the initial properties, PBS reliability of the IGZO TFT considerably improved with the post-annealing time, as shown in figure 7.2(c) and 7.2(d). When the post-annealing time was increased from 1 to 5 hrs,  $\Delta V_{th}$  after  $10^4$  s PBS reduced from 4.3 to 3.5 V. In order to investigate the causes of this PBS reliability improvement, the density of state (DOS) of the front channel interface ( $D_i$ ) with the PBS duration was evaluated. Low-high capacitance voltage measurement is one of the most popular techniques for analyzing semiconductor/insulator interface properties [127], [132]. However, these capacitance based extraction methods cannot provide the properties of defects such as trap time constant, capture cross section. Therefore, it is difficult to distinguish the defects which have overlapping energy distribution. In this work, the conduction method is chosen to extract the  $D_i$  not only because the conductance method is known as the most complete, high sensitivity, accurate method to characterize interface trap properties but also because the conductance method can provide the trap time constant of the defects [60], [64], [133]–[136].

The conductance method is based on measuring the parallel conductance of a metal insulator semiconductor as a function of gate bias and frequency. The density of interface defects and their properties can be obtained by fitting the measurement results to a theoretical model. The series resistance and bulk states could affect the measured conductance, but these factors could be taken in to account in the fitting model. In this work, we assumed that the interface traps are distributed continuously across the IGZO bandgap. Therefore, the equation describing a relationship between parallel conductance ( $G_p$ ) and frequency ( $f$ ) of the applied AC signal is [131]

$$\frac{G_p}{\omega} = \frac{qD_i}{2\omega\tau_i} \ln[1 + (\omega\tau_i)^2]. \quad (1)$$

Where angular frequency  $\omega = 2\pi f$ ,  $\tau_i$  is interface trap time constant. The  $D_i$  and  $\tau_i$  can be extracted from the peak intensity and the peak position of the  $G_p/\omega$  versus  $\omega^{-1}$  curve. The DOS of an interface trap states and the interface trap time constant can be calculated using the following formula [137]:

$$D_i = \frac{2}{qA} \frac{G_{mp}/\omega}{[(G_{mp}/\omega C_{ox})^2 + (1 - C_{mp}/C_{ox})^2]} \quad (2)$$

$$\tau_i = 2/\omega_{mp} = [v_{th}\sigma N \exp(-q\phi_s/kT)]^{-1}. \quad (3)$$

Where A is the TFT channel area;  $C_{ox}$  is the oxide gate capacitance value;  $G_{mp}$  is the conductance value of the peak;  $C_{mp}$  and  $\omega_{mp}$  respectively are capacitance and angular frequency values which correspond to the  $G_{mp}$  value;  $v_{th}$  is the thermal velocity;  $\sigma$  is the capture cross-section; N is the defect density;  $\phi_s$  is the surface potential; k is the Boltzmann's constant; and T is the absolute temperature.

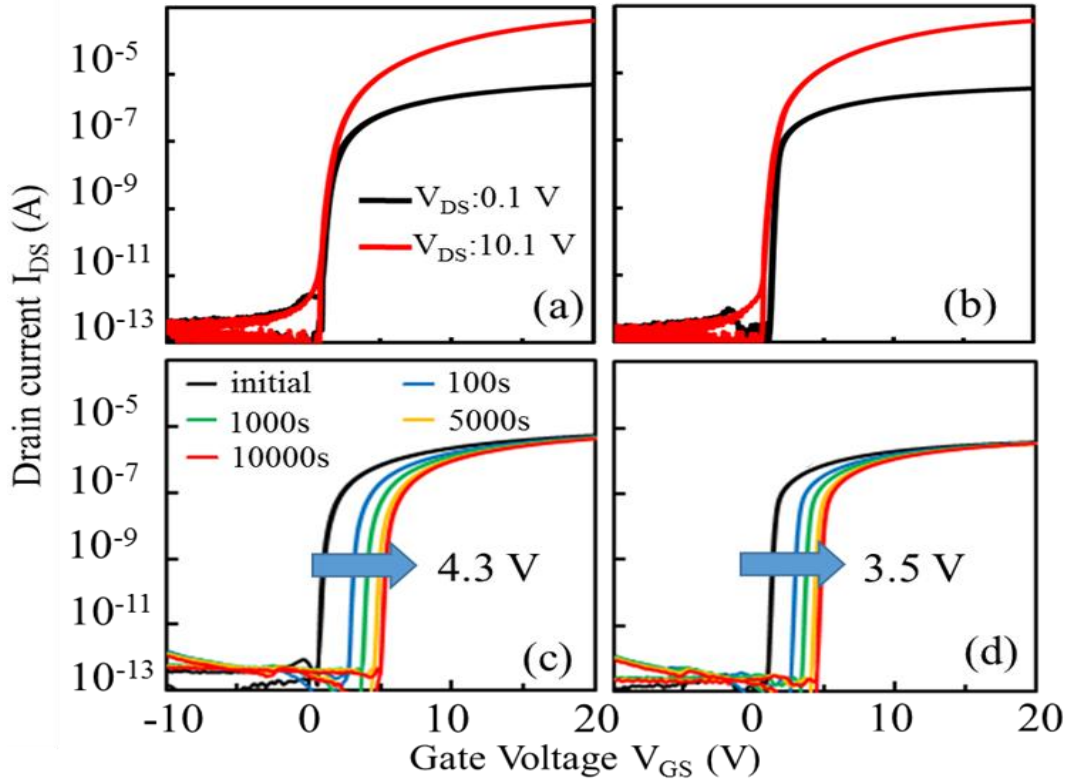


Figure 7. 2: The Initial transfer characteristic of IGZO TFT of (a) sample A1 and of (b) sample A2; change in transfer characteristic ( $V_{DS} = 0.1$  V) under PBS of (c) sample A1, and of (d) sample A2

### 7.3.2 DOS of Interface defects at the initial state

Figures 7.3(a), 7.3(b) and 7.3(c) represent the conductance characteristic,  $D_i$  and  $\tau_i$  of sample A1 at the initial state, respectively. Figures 7.3(d), 7.3(e), and 7.3(f) predict the

conductance characteristic,  $D_i$  and  $\tau_i$  of sample A2 at the initial state, respectively. The  $D_i$  interrupted at the applied DC gate voltage ( $V_g$ ) of 1.8 V as shown in figure 7.3(b), 7.3(e), similarly to  $\tau_i$  as shown in figure 7.3(c), 7.3(f). The  $\tau_i$  either exponentially depended on the applied gate voltage (represented by the orange color in the figure) or did not depend on the applied gate voltage (represented by the blue color in the figure). This suggests that those are different kind of interface defects. In order to classify the origin of the interface defects, the capacitance voltage (C-V) measurement at a frequency of 100 Hz was conducted to determine the flat band voltage. Figures 7.4(a) and 7.4(c) respectively show the C-V curve of sample A1 and of sample A2. Figures 7.4(b) and 7.4(d) represent the relationship between surface potential and gate voltage in sample A1 and in sample A2, respectively. Figures 7.3(b) and 7.3(e) show that the  $D_i$  and  $\tau_i$  were interrupted at the  $V_g$  near the flat band voltage ( $V_{FB}$ ). Therefore, the defects which locate above  $V_{FB}$  are the acceptor-like interface defects. The defects which locate below  $V_{FB}$  are donor-like interface defects. The  $D_i$  of the acceptor-like interface defects fluctuated between  $1 \times 10^{12}$  and  $1.5 \times 10^{12}$   $\text{eV}^{-1}\text{cm}^{-2}$  and distributed uniformly, as shown in figure 7.3(b) and 7.3(e). This  $D_i$  value is comparable to previous reports [138]–[141]. The  $D_i$  dispersion can be attributed to a surface potential ( $\phi_s$ ) fluctuation, which is caused by accumulated electrons at the front channel interface. The  $\tau_i$  of the acceptor-like interface defects was proportional to  $1/\exp(\sim \phi_s)$ , and this is consistent with the equation (7.3). The extracted  $D_i$  of the donor-like interface defects of the sample A1 ( $\sim 1.3 \times 10^{11}$   $\text{eV}^{-1}\text{cm}^{-2}$ ) and of the sample A2 ( $1.4 \times 10^{11}$   $\text{eV}^{-1}\text{cm}^{-2}$ ) were not considerably different as shown in figure 7.3(b) and 7.3(e). This result implies that the influence of the post-annealing time on the DOS of interface defects in the IGZO TFT was negligible. In spite of the  $\tau_i$  of the acceptor-like interface defects, figure 7.3(c), 7.3(f) show that the  $\tau_i$  of the donor-like interface defects did not depend on surface potential or Fermi level. The independence  $\tau_i$  of the donor-like interface defects on surface potential is not consistent with the equation (7.3), as in equation (7.33) the  $\tau_i$  is proportional to  $1/\exp(\sim \phi_s)$ . Therefore, the donor-like interface defects mentioned here could not only refer to the defects at the front channel interface but also refer to the donor-like defects that exist in the  $\text{SiO}_x$  GI within tunneling distances ( $< 50 \text{ \AA}$ ) of the front channel interface [131], [142]. From here on, the

term interface defects refers to defects both at the front channel interface and in the  $\text{SiO}_x$  near interface within tunneling distances. The interface defects could electrically communicate with the channel by tunneling [143], [144]. The  $\tau_i$  could be calculated by equation [134], [145]:

$$\tau_T = \frac{1}{2K_1d} \tau_0 \exp(2K_1d) \quad (7.4)$$

Where  $d$  is the length of the electron tunnel (or distance between the front interface and the defects in the insulator),  $K_1$  is the wave vector of carriers inside insulator, and  $\tau_0$  ( $d=0$ ) is the time constant of the states at the interface. Equation 7.44 indicates that the trap time constant does not depend on surface potential. This could be explained by the independence  $\tau_i$  of the donor-like interface defects on surface potential that is shown in figure 7.3(c) and 7.3(f). Figures 7.3(c) and 7.3(f) also show that the  $\tau_i$  of the donor-like interface defects of the sample A1 ( $\sim 2 \times 10^{-7}$  s) was lower than that of the sample A2 ( $\sim 1 \times 10^{-6}$  s). This means that long time post-annealing increases the trap time constant of the donor-like interface defects. The results and discussions above also imply that the extracted  $\tau_i$  of the interface defects from conductance measurement is an important parameter for classifying the defects. The acceptor-like and the donor-like interface defects, which overlap each other near  $V_{\text{FB}}$ , could be distinguished by the  $\tau_i$ .

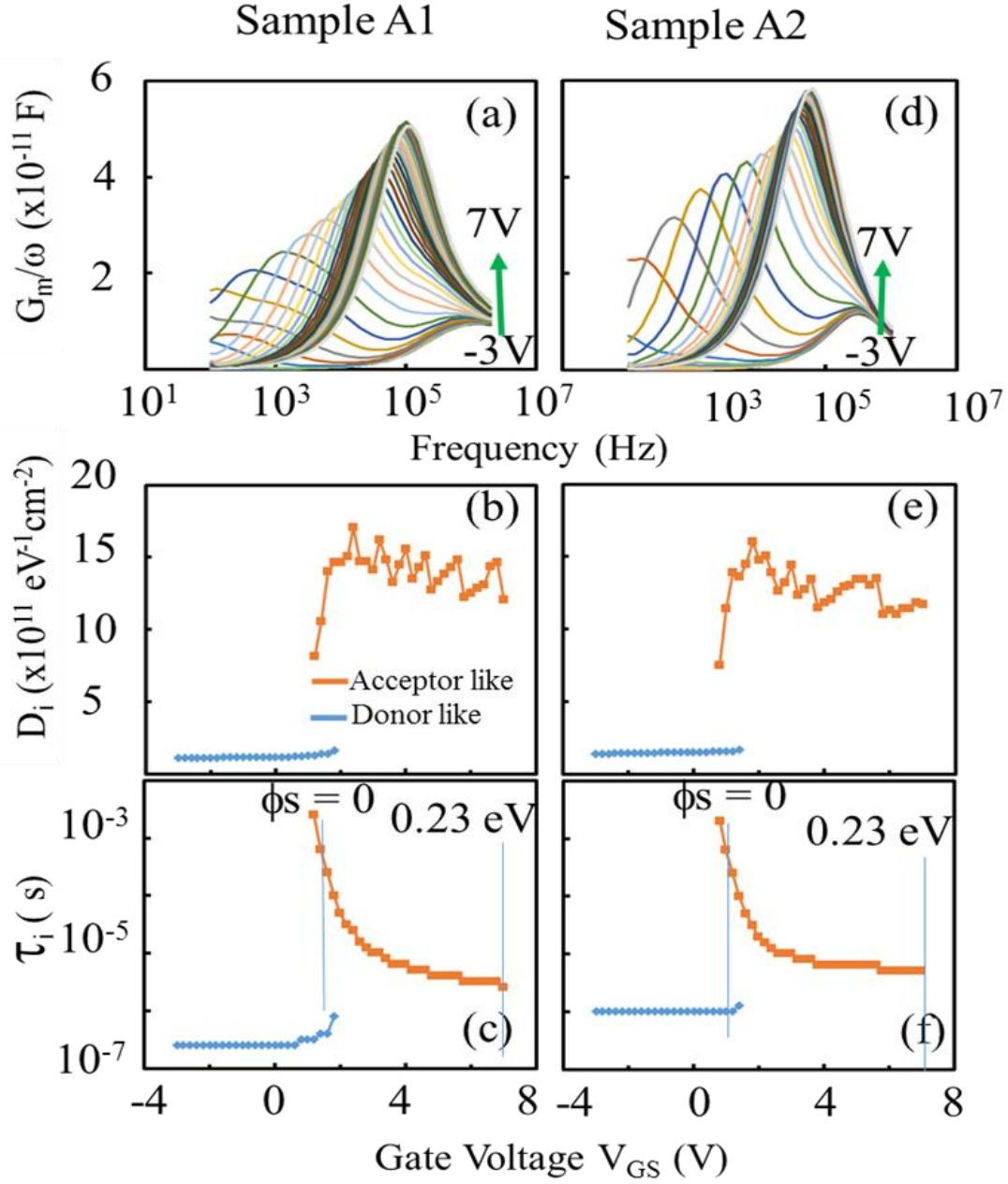


Figure 7. 3: A set of  $G_m/\omega$  versus  $f$  curves with different applied DC gate voltage for (a) sample A1, and for (d) sample A2 at initial state; the distribution of  $D_i$  as function of applied DC gate voltage for (b) sample A1, and for (e) sample A2 at initial state; the variation of  $\tau_i$  as function of applied DC gate voltage for (c) sample A1, and for (f) sample A2 at initial state.

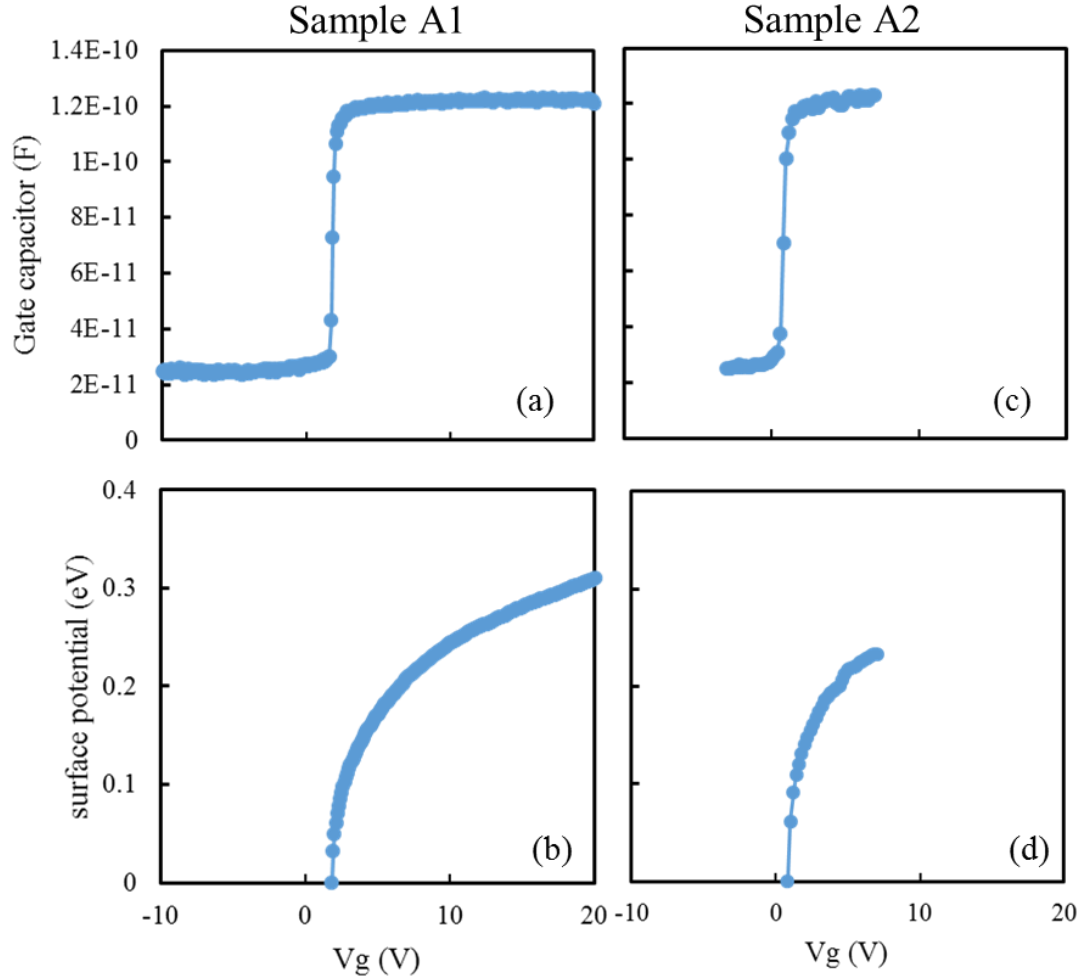


Figure 7. 4: Capacitance - gate voltage curve of (a) sample A1, of (c) sample A2 and surface potential - gate voltage relationship of (b) sample A1, of (d) sample A2.

### 7.3.3 PBS degradation mechanism of 1 hour post-annealing sample

In order to investigate the relationship between the interface defects and the positive shift in the transfer characteristic of sample A1 under PBS, conductance measurement was conducted. The flat band voltage of sample A1 after PBS stress was also extracted. Figures 7.5(a) and 7.5(c) respectively show the C-V curve of sample A1 at the PBS duration of 1000 and 5000 s. Figures 7.5(b) and 7.5(d) represent the relationship between surface potential and gate voltage in sample A1 at the PBS stress time of 1000 and 5000 s, respectively. A conductance characteristic,  $D_i$  and  $\tau_i$  of the sample A1 at the PBS stress time of 1000 s are

respectively illustrated in figure 7.6(a), 7.6(b), and 7.6(c). Figures 7.6(d), 7.6(e), and 7.6(f) show a conductance characteristic,  $D_i$  and  $\tau_i$  of the sample A1 at the PBS stress time of 5000 s, respectively. Figures 7.6(b), 7.6(b), and 7.6(e) show that the DOS of acceptor-like interface defects did not change with PBS duration. However, the donor-like interface defects disappeared with the PBS stress time. A vanishing of the donor-like defects reduced the positive charges at the front channel interface, resulting in a positive shift in the transfer curve shown in figure 7.2(c). Under PBS, the donor-like interface defects were able to capture electrons and become electrically inactive; as a consequence, the donor-like interface defects disappeared in the conductance characteristic. This result indicates that the stabilization of the donor-like interface defects is the dominant degradation mechanism in the sample A1 under PBS. The donor-like defects at the IGZO/GI interface or in GI near interface act as electron trapping centers. It is noted that the donor-like defects located near the valence band minimum are less stable than those located near the Femi level. Therefore, the donor-like defects located near the valence band minimum will be stabilized more easily.



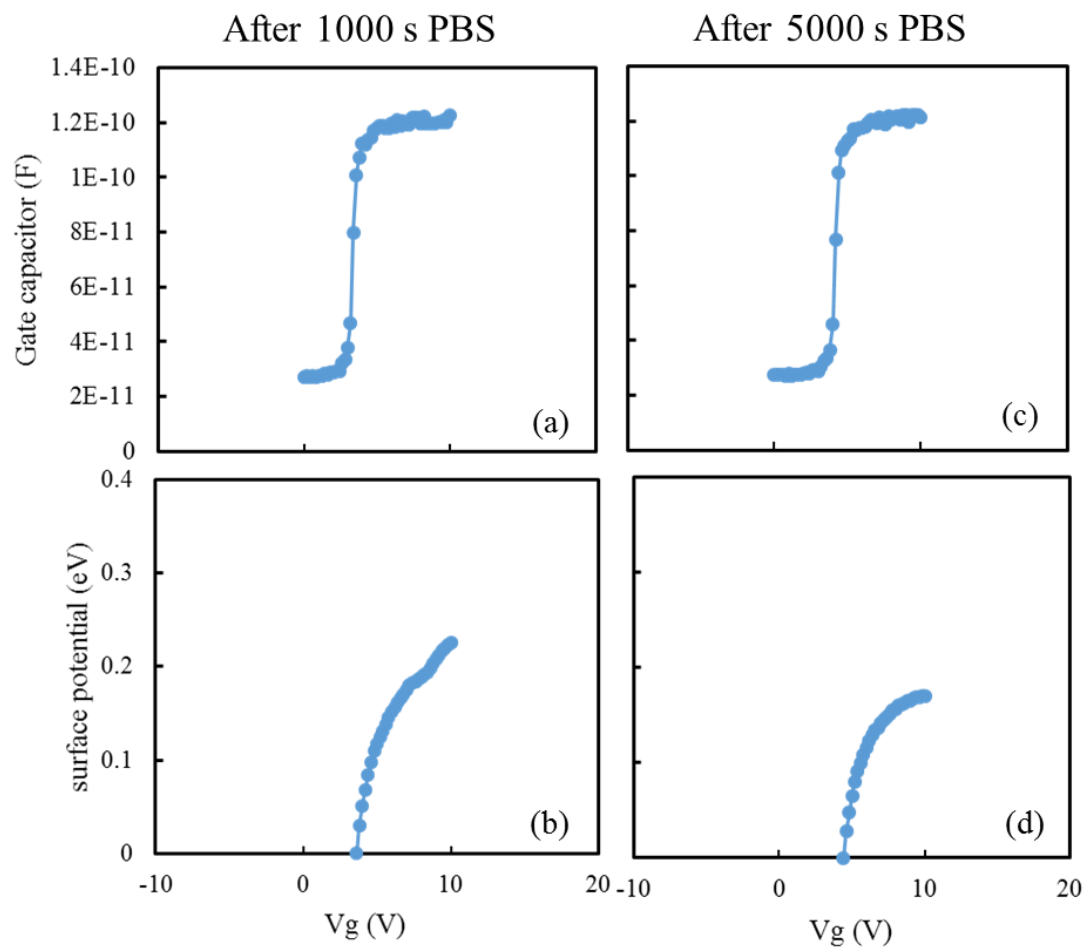


Figure 7. 5: Capacitance - gate voltage curve of sample A1 after (a) 1000 s PBS, (c) 5000 s PBS and surface potential - gate voltage relationship of sample A1 after (b) 1000 s PBS, (d) 5000 s PBS.

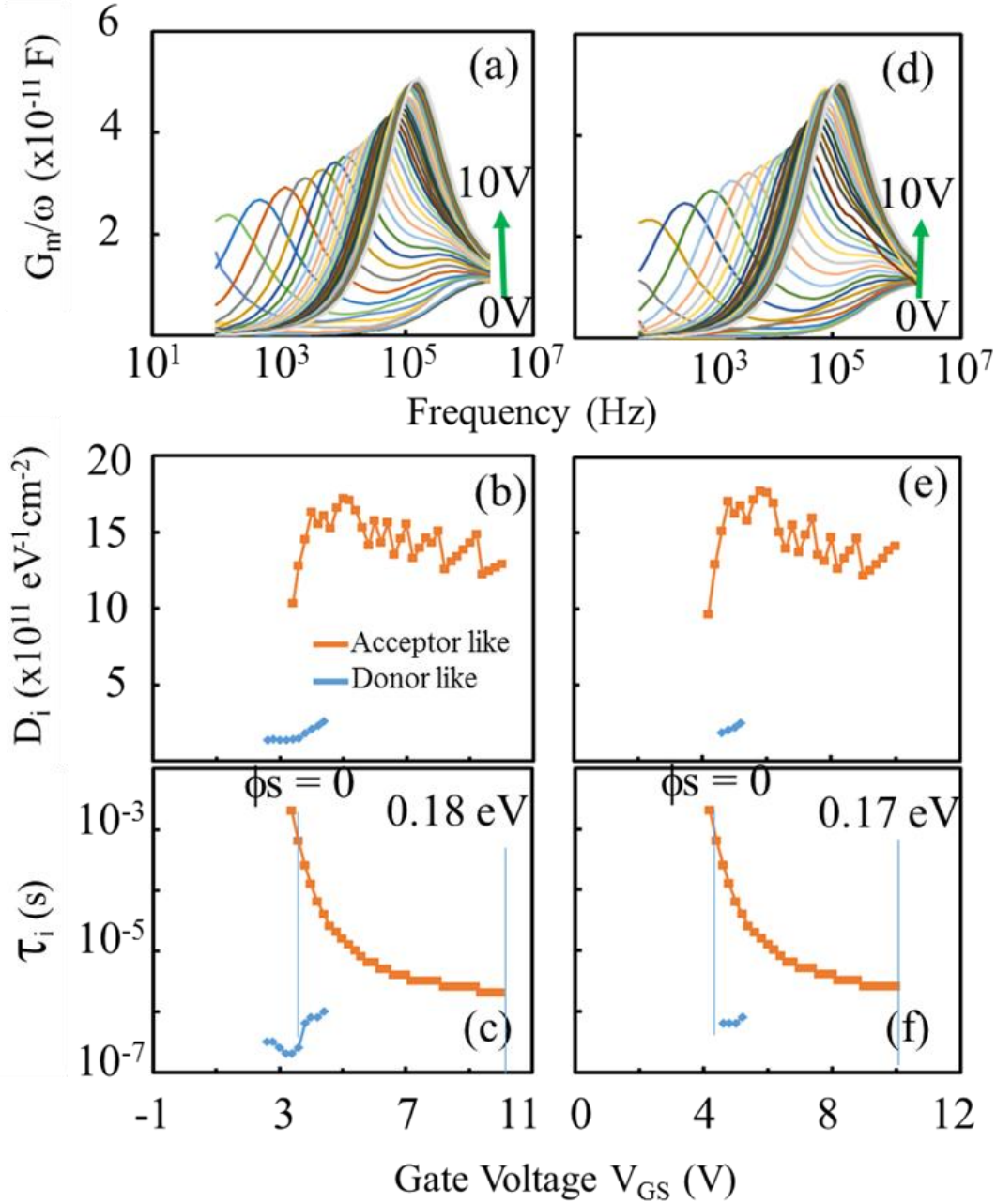


Figure 7. 6: A set of  $G_m/\omega$  versus  $f$  curves with different applied DC gate voltage for (a) sample A1 after (a) 1000 s , (d) 5000 s PBS; the distribution of (b)  $D_i$ , and (c)  $\tau_i$  as function of applied DC gate voltage in sample A1 after 1000 s PBS; the distribution of (e)  $D_i$ , and (f)  $\tau_i$  as function of applied DC gate voltage in sample A1 after 5000 s PBS.

#### 7.3.4 PBS degradation mechanism of 5 hours post-annealing sample

Figures 7.7(a) and 7.7(c) respectively show the C-V curve of sample A2 at the PBS duration of 1000 and 5000 s. Figures 7.7(b) and 7.7(d) represent the relationship between surface potential and gate voltage in sample A2 at the PBS stress time of 1000 and 5000 s, respectively. The change in  $D_i$  with the PBS duration was analyzed to investigate the reasons for the improvement in PBS stability in sample A2. Figures 7.8(a), 7.8(b) and 7.8(c) represent a conductance characteristic,  $D_i$  and  $\tau_i$  of the sample A2 at the PBS stress time of 1000 s, respectively. Figures 7.8(d), 7.4(e) and 7.8(f) depict a conductance characteristic,  $D_i$  and  $\tau_i$  of the sample A2 at the PBS stress time of 5000 s, respectively. Unlike in sample A1, the DOS of the donor-like interface defects in sample A2 slightly decreased, from  $1.4 \times 10^{11} \text{ eV}^{-1} \text{ cm}^{-2}$  at the initial state to  $1.3 \times 10^{11} \text{ eV}^{-1} \text{ cm}^{-2}$  at the PBS stress time of 5000 s, as shown in figure 7.3(e), 7.8(b) and 7.8(e). These results indicate that in sample A2, the donor-like interface defects are stable under PBS. As discussed in the previous paragraph, the donor-like interface defects are stabilized by capturing electrons. Therefore, the stability of the donor-like interface defects in the sample A2 under PBS suggests that electrons were difficult to trap at the front channel interface. In other words, long time annealing improves the electron trapping resistivity at the IGZO/SiO<sub>x</sub> interface, resulting in an improvement in PBS stability. Figures 7.3(f), 7.8(c), 7.8(f) show that the  $\tau_i$  of the donor-like interface defects also reduced, from  $\sim 1 \times 10^{-6}$  to  $6 \times 10^{-7}$  s, when PBS stress time was increased from 0 (initial state) to 5000 s. Equation (7.4) suggests that this reduction in  $\tau_i$  could be related to a reduction in the tunneling distance. As shown in figures 7.3(d), 7.8(a) and 7.8(d), the conductance characteristic at the PBS duration of 1000 and of 5000 s appeared new peaks. The distribution of  $D_i$  and  $\tau_i$  (represented by the red color) extracting from the new peaks are respectively shown in figure 7.8(b) and 7.8(c) for the PBS stress time of 1000 s and in figure 7.8(e) and 7.8(f) for the PBS stress time of 5000 s. Figures 7.8(c) and 7.8(f) show that the  $\phi_s$  dependence of  $\tau_i$  of the created defects was similar to that of the acceptor-like interface defects (represented by the orange color). This suggests that the new peaks associate with created acceptor-like defects at the front channel interface. The created acceptor-like defects locate below Fermi level and act as electron trap states at the front channel interface, resulting in a positive shift in the TFT transfer characteristic. The  $D_i$  of the created acceptor-like defects in the sample A2 at the PBS stress time of 1000 s exponentially increased from  $0.7 \times 10^{10}$  to  $7.6 \times 10^{10}$

$\text{eV}^{-1}\text{cm}^{-2}$  when the applied gate voltage was increased from 1.6 to 2.6 V, as shown in figure 7.8(b). Figure 7.8(f) shows that the  $D_i$  of the created acceptor-like defects in sample A2 at the PBS stress time of 5000 s exponentially increased from  $1.1 \times 10^{10}$  to  $1.7 \times 10^{11} \text{ eV}^{-1}\text{cm}^{-2}$  when the applied gate voltage was increased from 2.2 to 3.6 V. These results imply that the acceptor-like defect generation was the dominant degradation mechanism in sample A2 under PBS. The negative charged oxygen interstitial ( $\text{O}_i^{2-}$ ) [85], the negative charged zinc vacancy ( $\text{V}_{\text{Zn}}^{-/2-}$ ) [81], [146], the negative charged of the displaced oxygen ( $\text{O}_{\text{Zn}}^{-/2-}$ ) [81], and undercoordinated indium [147] ... are possible candidates for these acceptor-like defects in IGZO TFTs. Due to the number of possibility candidates listed above, the origin of the created acceptor-like defects is difficult to determine. However, the results of studying DOS of the interface defects in sample A2 could identify that the created acceptor-like defects in IGZO TFT under PBS locate just below Fermi level. The results of studying DOS of the interface defects in sample A1 and A2 indicated that the PBS degradation mechanism changed from a donor-like interface defects stabilization to a deep defect generation when the post-annealing time was increased.

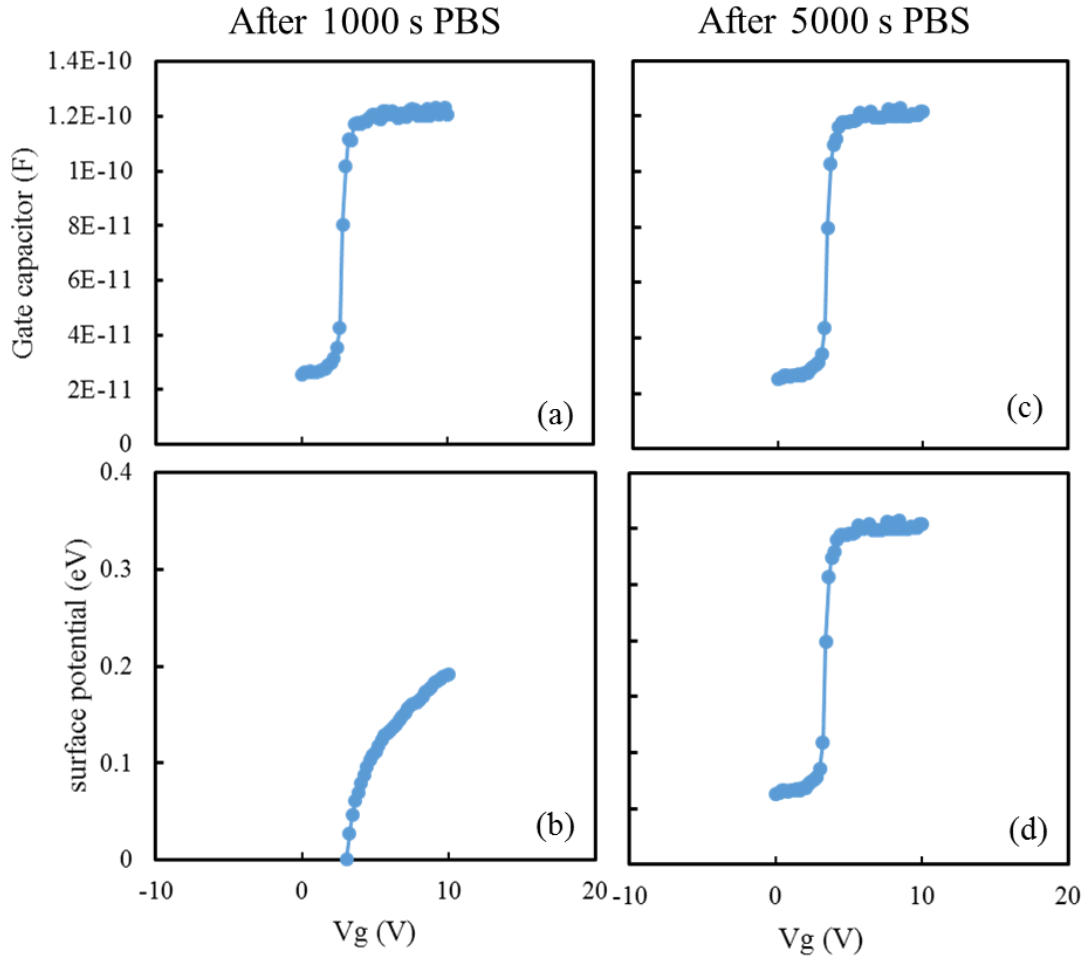


Figure 7. 7: Capacitance - gate voltage curve of sample A2 after (a) 1000 s PBS, (c) 5000 s PBS and surface potential - gate voltage relationship of sample A2 after (b) 1000 s PBS, (d) 5000 s PBS.

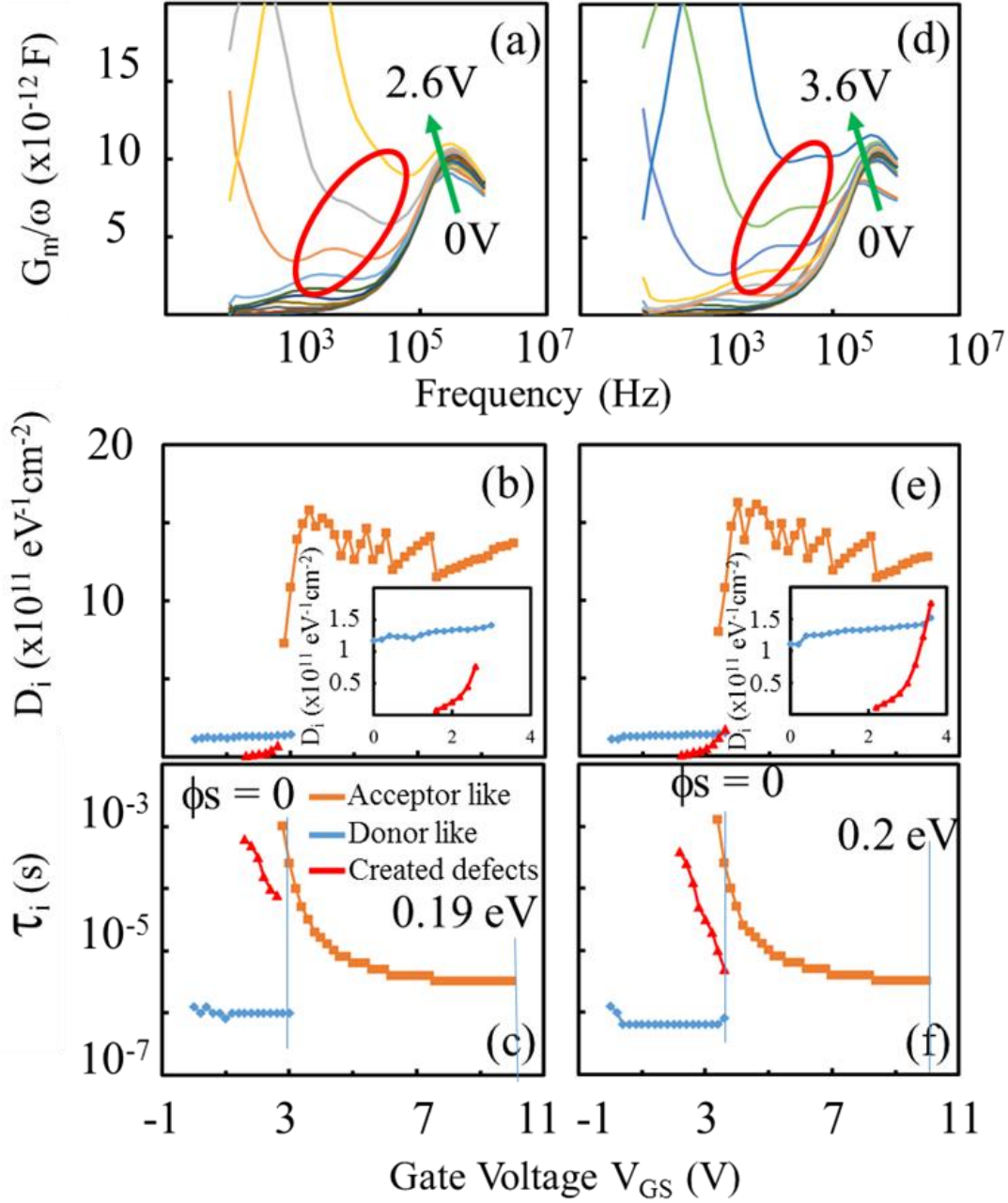


Figure 7. 8: A set of  $G_m/\omega$  versus  $f$  curves with different applied DC gate voltage for the sample A2 at PBS stress time of (a) 1000 s, and of (d) 5000 s; the distribution of (b)  $D_i$ , and (c)  $\tau_i$  as function of applied DC gate voltage in sample A2 after 1000 s PBS; the distribution of (e)  $D_i$ , and (f)  $\tau_i$  as function of applied DC gate voltage in sample A2 after 5000 s PBS; insert figure.(b) and (e) are the enlarge of the Figure. (b) and (e), respectively.

## **7.4 Summary**

This chapter discusses about the PBS degradation mechanism of the IGZO TFTs and the effect of the post-annealing time on PBS stability. The PBS reliability improved when the post annealing time was increased from 1 to 5 hours. The conductance measurement method was used to investigate the reason. The donor-like interface defects act as the electron trapping centers. The electron trapping resistance of a PECVD  $\text{SiO}_x$  was improved by increasing annealing duration. The stabilization of the donor-like defects at the front channel interface is the dominant reason for the PBS instability of the 1h post-annealing TFT. The DOS of the created deep acceptor-like interface defects in the IGZO TFT under PBS was experimentally identified in sample which has post annealing time of 5 hours. Deep acceptor-like defect generation at the IGZO/ $\text{SiO}_x$  interface is the main cause of PBS instability in the 5h post-annealing sample.

In this thesis, we investigated the NBIS and PBS degradation mechanism of IGZO TFT. The method to improve the reliability of IGZO TFT under NBIS and PBS was also proposed. A double sweeping measurement method was used to investigate the NBIS degradation mechanism. It was found that electron trapping at the back channel interface was a reason for the NBIS instability in IGZO TFT. In order to further clarify the NBIS degradation mechanism, we developed a new measurement method named as positive gate pulse mode. The positive gate pulse mode is a transfer characteristic measurement method in which a short positive gate pulse is applied to TFT prior to every transfer characteristic measurement. It was found that besides the electron trapping at the back channel interface, hole trapping at the front channel interface and defect generation in the channel were also causes of the NBIS instability in IGZO TFT. We found that the positive gate pulse mode is an effective means to quantify the effect of hole trapping and defect generation on NBIS instability in IGZO TFT. Therefore, inhibition of hole trapping and of defect generation is required to improve the NBIS stability of IGZO TFT. Initially, methods to reduce the generated defects in the channel under NBIS were discovered. It was found that defect generation was reduced by either increasing the deposition temperature of IGZO channel or decreasing the plasma PE-CVD power of the etching stopper deposition process. By quantitative analysis of the effect of hole trapping and defect generation on the NBIS instability, we found that hole trapping was the main reason for NBIS instability in IGZO TFT fabricated with a high deposition of IGZO channel. In order to reduce hole trapping at the front channel interface, we investigated hole generation in IGZO TFT under NBIS. The generated defects were found to be midgap traps for hole generation. Besides that the generated defects were also unstable. As they can be stabilized by capturing electrons, a driving method was proposed to improve the NBIS reliability in IGZO TFT.

The PBS degradation mechanism was also investigated by conductance method. We found that donor-like interface defects act as the electron trapping centers. The created deep acceptor-like interface defects in the IGZO TFT under PBS was experimentally identified. PBS reliability can be improved by increasing the post annealing time. A summary of the main results and conclusions of this thesis follows:



- I. Investigation of NBIS degradation mechanism of IGZO TFT by double sweeping mode and positive gate pulse mode, and the method to improve the NBIS reliability.
  1. A reference IGZO TFT was fabricated that had mobility of  $15.6 \text{ cm}^2/\text{Vs}$ , sub-threshold swing value of  $0.4 \text{ V/dec}$ , threshold voltage of  $1.65 \text{ V}$  and hysteresis of  $0.4 \text{ V}$ . IGZO TFT was stable under NBS, but when combined with blue light illumination, a degradation of Subthreshold swing (SS) in forward measurement, an increased in hysteresis ( $V_h$ ) and instability of threshold voltage were observed. The NBIS degradation behavior strongly depended on gate voltage stress. When  $V_{st}$  was increased from  $-20$  to  $-40 \text{ V}$ , (a) a positive  $V_{th}$  shift of  $7.1 \text{ V}$  without Ss degradation was observed in reverse measurement; the mobility – gate voltage curve shifted in parallel to the positive direction, (b) a negative  $V_{th}$  shift with Ss degradation and on current degradation was observed in forward measurement; and (c) the  $V_h$  increased from  $0.4$  to  $8.7 \text{ V}$  (after NBIS of  $10^4 \text{ s}$ ). The change in  $\Delta V_{rev}$  with NBIS stress time was well fitted to a stress exponential equation. These results imply that electron trapping at the back channel interface was a reason of the NBIS instability in IGZO TFT. The Positive Gate Pulse Mode was conducted to further clarify the NBIS degradation mechanism. The hump disappeared, and hysteresis decreased when a  $10 \text{ V} - 1 \text{ ms}$  positive gate pulse was applied. In the case of  $V_{st} = -40 \text{ V}$ , the hysteresis decreased from  $8.7$  to  $6.4 \text{ V}$ . The pulse height and pulse width also affected the NBIS degradation behavior. When a gate pulse height/width of  $5 \text{ V}/1 \text{ ms}$  was applied, the hysteresis decreased from  $8.7$  to  $7.5 \text{ V}$ , but Ss degradation was still observed in the forward curve. On the other hand when gate pulse height was increased to  $15 \text{ V}$ , the hysteresis further decreased to  $4.6 \text{ V}$ . The hysteresis also depended on the pulse width. The hysteresis of the IGZO-TFT decreased from  $8.4$  to  $0.9 \text{ V}$  when a positive gate pulse with pulse high of  $10 \text{ V}$  and pulse width of  $25 \text{ s}$  was applied. Results measured by positive gate pulse suggest that hole trapping in GI and defect generation in the channel were causes of the NBIS instability.
  2. Effect of IGZO deposition condition on the initial properties and NBIS reliability of the TFT was also investigated. The effect of IGZO deposition temperature on Ss value was negligible. However, electron mobility decreased from  $17.14$  to  $12.19 \text{ cm}^2/\text{V}\cdot\text{s}$  and  $V_{th}$  decreased from  $3.41$  to  $1.98 \text{ V}$  when the deposition temperature of the IGZO channel

was increased from RT to 220°C. Hall measurement of the IGZO thin film showed that when IGZO deposition temperature was increased from RT to 220°C, carrier concentration increased from  $-7 \times 10^{18}$  to  $-3 \times 10^{19} \text{ cm}^{-3}$ . Results of SIMS measurement suggest that the hydrogen concentration in IGZO film increased with the IGZO deposition temperature. Deposition temperature of IGZO channel also affected the NBIS reliability. The hysteresis measured using DSM dramatically decreased from 17.9 to 9.0 V and  $V_{\text{rev}}$  decreased from 18.2 to 9.6 V when the IGZO deposition temperature was increased from RT to 150°C. When the deposition temperature was further increased from 150°C to 220°C, hysteresis decreased slightly from 9.0 to 8.1 V and  $V_{\text{rev}}$  further decreased from 9.6 to 7.9 V. The quantitative analysis effect of hole trapping and of defect generation on the hysteresis show that  $V_{\text{hole}}$  was 6.5 V, regardless of the IGZO deposition temperature. However, increasing deposition temperature of IGZO channel could reduced defect generation in the TFT under NBIS.  $\Delta V_{\text{defect}}$  decreased significantly from 11.5 to 2.2 V when the IGZO deposition temperature was increased from RT to 150°C. However, when the IGZO deposition temperature was further increased to 220°C,  $\Delta V_{\text{defect}}$  decreased slightly from 2.2 to 1.7 V. XRR measurement shows that when the deposition temperature was increased from RT to 150 and 220°C, the IGZO film density increased from 6.0 to 6.4 and 6.5  $\text{g/cm}^3$  respectively. This suggests that the defect generation in IGZO TFT under NBIS could be reduced by increasing the density of the channel.

3. Plasma power of ES deposition also influenced the initial properties and NBIS reliability of IGZO TFT.  $S_s$  values of all TFTs fluctuated between 0.35 and 0.38 V/decade. However, electron mobility increased from 11.6 to 13.2  $\text{cm}^2/\text{Vs}$  and  $V_{\text{th}}$  decreased from 2.8 to 2.1 V when the plasma power of the etching stopper deposition process was increased from 40 to 55 W.  $\Delta V_{\text{rev}}$  increased from 2.4 to 13.6 V when the plasma power was increased from 40 to 55 W. The hysteresis induced by trapped holes at the front channel interface was 2.9 V regardless of the plasma power of etching stopper deposition process. In spite of the hysteresis induced by the trapped hole, the hysteresis induced by generated defects was strongly influenced by the plasma power of the ES deposition process. The hysteresis induced by the generated defects increased from 0.9 to 3.3 V when the plasma power was increased from 40 to 50 W. The

hysteresis induced by the generated defects increased further to 4.7 V when the plasma power was increased to 55 W. These results suggest that etching stopper deposition conditions had a strong impact on the defect generation in IGZO TFTs under NBIS; and the defects were mainly generated at the back channel interface.

4. When the NBIS stress time was 200 s, the transfer curve recovered to its initial state when the positive gate voltage was applied prior to the transfer characteristic measurement. However, when NBIS stress time exceeded 250 s, the transfer curve shifted negatively even though the positive gate pulse was applied. The effect of illumination light intensity on NBIS stability in IGZO TFT was also investigated. The stress voltage and stress time was remained at -30 V and 250 s, respectively. The light intensity was varied from 0.1 to 0.4 mW/cm<sup>2</sup>. These results show that the transfer curve could be recovered to its initial state when LI of 0.1 mW/cm<sup>2</sup> was applied. When the LI was increased to 0.4 mW/cm<sup>2</sup>, a greater negative shift in the transfer curve was obtained. These results suggest hole generation occurs as follow. At the early stage, the incident light excites electrons from deep trap defects to the conduction band and generated defects ( $V_O^+$  and  $V_O^{2+}$ ). The generated defects act as a midgap trap state. The incident light also excites electrons from the valence band to the midgap trap states and generates free holes. However, due to the low emission rate of deep trap defects (ref), the density of state (DOS) of midgap trap state was small when the NBIS stress time was small. As a result, the number of trapped holes at the GI can be negligible. When the NBIS stress time was increased, the DOS of midgap trap state exponentially increased. As a consequence, trapped hole at the GI dramatically increased when the NBIS stress time exceeded 250 s. This result suggests that, in order to improve NBIS stability, we should reduce the DOS of midgap trap state. As discussed above, the midgap trap state could be stabilized using a positive gate pulse. Therefore, the NBIS stability of IGZO TFT could be improved by applying a positive gate pulse alternatively to the negative gate pulse. In other words, in order to improve the NBIS stability, the display needs to be working at high frame rate and low refresh time.

## II. PBS degradation mechanism and method to improve the PBS reliability.

The effect of post annealing time on the PBS reliability was investigated.  $V_{th}$  of ~1.3 V, mobility of ~12 cm<sup>2</sup>/Vs, and  $S_s$  value of ~0.1 Vdec<sup>-1</sup> were not considerably different

between the 1 hour (A1) and 5 hours (A2) annealing samples. In spite of the initial properties, PBS reliability of the IGZO TFT considerably improved with the post-annealing time. When the post-annealing time was increased from 1 to 5 hrs,  $\Delta V_{th}$  after  $10^4$  s PBS reduced from 4.3 to 3.5 V. In order to investigate the causes of this PBS reliability improvement, the density of state (DOS) of the front channel interface ( $D_i$ ) with the PBS duration was evaluated. The conductance measurement method was used to investigate the PBS degradation mechanism of IGZO TFT. The extracted  $D_i$  of the donor-like interface defects of the sample A1 ( $\sim 1.3 \times 10^{11} \text{ eV}^{-1} \text{ cm}^{-2}$ ) and of the sample A2 ( $1.4 \times 10^{11} \text{ eV}^{-1} \text{ cm}^{-2}$ ) were not considerably different. However, the trap time constant  $\tau_i$  of the donor-like interface defects of the sample A1 ( $\sim 2 \times 10^{-7}$  s) was lower than that of the sample A2 ( $\sim 1 \times 10^{-6}$  s). This means that long time post-annealing increases the trap time constant of the donor-like interface defects. For the sample A1, the donor-like interface defects disappeared with the PBS stress time. The results indicate that the stabilization of donor-like interface defects are a reason for PBS instability. The donor-like defects, which locate at the IGZO/GI interface or in GI near interface, act as electron trapping centers. Unlike in sample A1, the DOS of the donor-like interface defects in sample A2 slightly decreased, from  $1.4 \times 10^{11} \text{ eV}^{-1} \text{ cm}^{-2}$  at the initial state to  $1.3 \times 10^{11} \text{ eV}^{-1} \text{ cm}^{-2}$  at the PBS stress time of 5000 s. The  $\tau_i$  of the donor-like interface defects also reduced, from  $\sim 1 \times 10^{-6}$  to  $6 \times 10^{-7}$  s, when PBS stress time was increased from 0 (initial state) to 5000 s. These results indicate that in sample A2, the donor-like interface defects are stable under PBS. It was also found that acceptor-like defects were generated in sample A2 under PBS. The  $D_i$  of the created acceptor-like defects in the sample A2 at the PBS stress time of 1000 s exponentially increased from  $0.7 \times 10^{10}$  to  $7.6 \times 10^{10} \text{ eV}^{-1} \text{ cm}^{-2}$  when the applied gate voltage was increased from 1.6 to 2.6 V. The  $D_i$  of the created acceptor-like defects in sample A2 at the PBS stress time of 5000 s exponentially increased from  $1.1 \times 10^{10}$  to  $1.7 \times 10^{11} \text{ eV}^{-1} \text{ cm}^{-2}$  when the applied gate voltage was increased from 2.2 to 3.6 V.

We also investigated the effects of post annealing time on the PBS stability of IGZO TFT. These results imply that when the post annealing time was increased from 1 to 5 hours, the electron trapping resistivity at the IGZO/SiO<sub>x</sub> interface was improved. This is a reason for the PBS improvement mentioned above. However, deep acceptor-like

interface defects were detected in the 5 hours post annealing sample. The defects were located just below Fermi level. This result also suggests that the PBS degradation changed from donor-like defects stabilization to deep acceptor-like defects creation.

---

## PUBLICATIONS AND ORAL PRESENTATIONS

---

- (1) **Mai Phi Hung** (*corr-auth*), Dapeng Wang, and Mamoru Furuta (*corr-auth*)/ Investigating Effect of Postannealing Time on Positive Bias Stress Stability of In–Ga–Zn–O TFT by Conductance Method/ IEEE Trans. on Electron Devices /accepted.
- (2) **Mai Phi Hung** (*corr-auth*), Dapeng Wang, Jingxin Jiang, and Mamoru Furuta/Negative Bias and Illumination Stress Induced Electron Trapping at Back-Channel Interface of InGaZnO Thin-Film Transistor/ECS Solid State Letters/Vol 3/2014.
- (3) **Mai Phi Hung** (*corr-auth*), Dapeng Wang, Tasuya Toda, Jingxin Jiang, and Mamoru Furuta/Quantitative Analysis of Hole-Trapping and Defect-Creation in InGaZnO Thin-Film Transistor under Negative-Bias and Illumination-Stress/ECS Journal of Solid State Science and Technology/Vol 3/2014
- (4) **Mai Phi Hung** (*corr-auth*), Dapeng Wang, and Mamoru Furuta (*corr-auth*)/Origins of an Improvement of Negative Gate Bias and Illumination Stress Stability in In-Ga-Zn-O Thin-film Transistor by Applying Alternative Current (AC-) Gate Bias/ECS Solid State Letters/*under review*
- (5) Dapeng Wang, **Mai Phi Hung**, Jingxin Jiang, Tasuya Toda, and Mamoru Furuta/Suppression of Degradation Induced by Negative Gate Bias and Illumination Stress in Amorphous InGaZnO Thin-Film Transistors by Applying Negative Drain Bias/Applied Materials and Interfaces/Vol 6/2014
- (6) Dapeng Wang, **Mai Phi Hung**, Jingxin Jiang, Tasuya Toda, and Mamoru Furuta/Effect of Drain Bias on Negative Bias an Illumination Stress Induced Induced Degradation in Amorphous InGaZnO Thin-Film Transistors/Japanese Journal of Applied Physics/Vol 3/2014
- (7) Mamoru Furuta, **Mai Phi Hung**, Jingxin Jiang, Dapeng Wang, Shigekazu Tomai, Hiromi Hayasaka, and Koki Yano/(Invited) Negative-Bias with Illumination Stress Induced State Creation in Amorphous InGaZnO Thin-Film Transistor/ECS Transactions/Vol 54/2013
- (8) Jingxin Jiang, Tatsuya Toda, **Mai Phi Hung**, Dapeng Wang, and Mamoru Furuta/Highly Stable Fluorine-passivated In-Ga-Zn-O Thin-Film transistors under Positive Gate Bias and Temperature Stress/Applied Physics Express/Vol 7/ 2014.

(9) Tatsuya Toda, Dapeng Wang, Jingxin Jiang, **Mai Phi Hung**, and Mamoru Furuta/Quantitative Analysis of the Effect of Hydrogen Diffusion from Silicon Oxide Etch-Stopper Layer into Amorphous In-Ga-Zn-O on Thin-Film Transistor/IEEE Transactions on Electron Devices/Vol 61/2014.

Oral Presentation:

(1) *International Display Workshops 13*. December 4-6, 2013 – Sapporo, Japan  
“Influence of Charge Trapping on Hysteresis of InGaZnO Thin-Film Transistors under Negative Bias and Illumination Stress.”

(2) *14<sup>th</sup> International Meeting on Information Display*. August 26-29, 2014 – Deagu, Korea  
“Influence of Etch-stopper Deposition on Defect Creation and Hole Trapping in IGZO-TFT under Negative Bias and Illumination Stress.”

---

REFERENCE:

---

- [1] S.-T. W. Jiun-Haw Lee, David N. Liu, *Introduction to Flat Panel Displays*. Wiley & Sons, 2008.
- [2] Barnouw Erik, *Tube of Plenty : The Evolution of American Television: The Evolution of American Television*. Oxford University Press, 1990.
- [3] S. A. Rodney Carlisle, *Scientific American Inventions and Discoveries: All the Milestones in Ingenuity--From the Discovery of Fire to the Invention of the Microwave Oven*. John Wiley & Sons, Inc., 2005.
- [4] A. Abramson, *The History of Television, 1942 to 2000*. McFarland; Paperback edition, 2007.
- [5] N. Koide, *The Liquid Crystal Display Story*. Springer Japan, 2014.
- [6] R. Williams, "Electro-optical elements utilizing an organic nematic compound," US3322485 A, 1962.
- [7] M. Orita, H. Ohta, M. Hirano, S. Narushima, and H. Hosono, "Amorphous transparent conductive oxide InGaO<sub>3</sub>(ZnO)<sub>m</sub> (m≤4): a Zn4s conductor," *Philos. Mag. Part B*, vol. 81, no. 5, pp. 501–515, May 2001.
- [8] T. Minami, H. Sonohara, S. Takata, and H. Sato, "Highly Transparent and Conductive Zinc-Stannate Thin Films Prepared by RF Magnetron Sputtering," *Jpn. J. Appl. Phys.*, vol. 33, no. Part 2, No. 12A, pp. L1693–L1696, Dec. 1994.
- [9] X. Wu, "Properties of transparent conducting oxides formed from CdO and ZnO alloyed with SnO<sub>2</sub> and In<sub>2</sub>O<sub>3</sub>," *J. Vac. Sci. Technol. A Vacuum, Surfaces, Film.*, vol. 15, no. 3, p. 1057, May 1997.
- [10] H. A. Klasens and H. Koelmans, "A tin oxide field-effect transistor," *Solid. State. Electron.*, vol. 7, no. 9, pp. 701–702, Sep. 1964.



- [11] K. Nomura, H. Ohta, A. Takagi, T. Kamiya, M. Hirano, and H. Hosono, “Room-temperature fabrication of transparent flexible thin-film transistors using amorphous oxide semiconductors.,” *Nature*, vol. 432, no. 7016, pp. 488–92, Nov. 2004.
- [12] R. L. Hoffman, B. J. Norris, and J. F. Wager, “ZnO-based transparent thin-film transistors,” *Appl. Phys. Lett.*, vol. 82, no. 5, p. 733, Jan. 2003.
- [13] B. J. Norris, J. Anderson, J. F. Wager, and D. A. Keszler, “Spin-coated zinc oxide transparent transistors,” *J. Phys. D. Appl. Phys.*, vol. 36, no. 20, pp. L105–L107, Oct. 2003.
- [14] Y.-J. Chang, D.-H. Lee, G. S. Herman, and C.-H. Chang, “High-Performance, Spin-Coated Zinc Tin Oxide Thin-Film Transistors,” *Electrochem. Solid-State Lett.*, vol. 10, no. 5, p. H135, May 2007.
- [15] H.-C. Cheng, C.-F. Chen, and C.-C. Lee, “Thin-film transistors with active layers of zinc oxide (ZnO) fabricated by low-temperature chemical bath method,” *Thin Solid Films*, vol. 498, no. 1–2, pp. 142–145, Mar. 2006.
- [16] A. Ashour, M. A. Kaid, N. Z. El-Sayed, and A. A. Ibrahim, “Physical properties of ZnO thin films deposited by spray pyrolysis technique,” *Appl. Surf. Sci.*, vol. 252, no. 22, pp. 7844–7848, Sep. 2006.
- [17] M. Furuta, T. Kawaharamura, T. Toda, and T. Hirao, “Electrical Properties of the Thin-Film Transistor With an Indium–Gallium–Zinc Oxide Channel and an Aluminium Oxide Gate Dielectric Stack Formed by Solution-Based Atmospheric Pressure Deposition,” *IEEE Electron Device Lett.*, vol. 33, no. 6, pp. 851–853, Jun. 2012.
- [18] T. Hirao, M. Furuta, H. Furuta, T. Matsuda, T. Hiramatsu, H. Hokari, M. Yoshida, H. Ishii, and M. Kakegawa, “Novel top-gate zinc oxide thin-film transistors (ZnO TFTs) for AMLCDs,” *J. Soc. Inf. Disp.*, vol. 15, no. 1, p. 17, 2007.
- [19] M.-G. Kim, M. G. Kanatzidis, A. Facchetti, and T. J. Marks, “Low-temperature fabrication of high-performance metal oxide thin-film electronics via combustion processing,” *Nat. Mater.*, vol. 10, no. 5, pp. 382–8, May 2011.

- [20] M. W. J. Prins, K. O. Grosse-Holz, G. Müller, J. F. M. Cillessen, J. B. Giesbers, R. P. Weening, and R. M. Wolf, “A ferroelectric transparent thin-film transistor,” *Appl. Phys. Lett.*, vol. 68, no. 25, pp. 3650–3652, 1996.
- [21] M. W. J. Prins, S. E. Zinnemers, J. F. M. Cillessen, and J. B. Giesbers, “Depletion-type thin-film transistors with a ferroelectric insulator,” *Appl. Phys. Lett.*, vol. 70, no. 4, p. 458, 1997.
- [22] K. Matsuzaki, H. Yanagi, T. Kamiya, H. Hiramatsu, K. Nomura, M. Hirano, and H. Hosono, “Field-induced current modulation in epitaxial film of deep-ultraviolet transparent oxide semiconductor Ga<sub>2</sub>O<sub>3</sub>,” *Appl. Phys. Lett.*, vol. 88, no. 9, 2006.
- [23] G. Frank and H. Köstlin, “Electrical properties and defect model of tin-doped indium oxide layers,” *Appl. Phys. A Solids Surfaces*, vol. 27, no. 4, pp. 197–206, 1982.
- [24] L. Wang, M.-H. Yoon, G. Lu, Y. Yang, A. Facchetti, and T. J. Marks, “High-performance transparent inorganic-organic hybrid thin-film n-type transistors,” *Nat. Mater.*, vol. 5, no. 11, pp. 893–900, Nov. 2006.
- [25] R. E. Presley, C. L. Munsee, C.-H. Park, D. Hong, J. F. Wager, and D. A. Keszler, “Tin oxide transparent thin-film transistors,” *Journal of Physics D: Applied Physics*, vol. 37, no. 20, pp. 2810–2813, 2004.
- [26] T. Hirao, M. Furuta, T. Hiramatsu, T. Matsuda, C. Li, H. Furuta, H. Hokari, M. Yoshida, H. Ishii, and M. Kakegawa, “Bottom-Gate Zinc Oxide Thin-Film Transistors (ZnO TFTs) for AM-LCDs,” *IEEE Trans. Electron Devices*, vol. 55, no. 11, pp. 3136–3142, Nov. 2008.
- [27] T. Hirao, M. Furuta, H. Furuta, T. Matsuda, T. Hiramatsu, H. Hokari, and M. Yoshida, “4.1: Distinguished Paper: High Mobility Top-Gate Zinc Oxide Thin-Film Transistors (ZnO-TFTs) for Active-Matrix Liquid Crystal Displays,” *SID Symp. Dig. Tech. Pap.*, vol. 37, no. 1, p. 18, 2006.

- [28] S.-H. K. Park, C.-S. Hwang, J.-I. Lee, S. M. Chung, Y. S. Yang, L.-M. Do, and H. Y. Chu, “4.3: Transparent ZnO Thin Film Transistor Array for the Application of Transparent AM-OLED Display,” *SID Symp. Dig. Tech. Pap.*, vol. 37, no. 1, p. 25, 2006.
- [29] H. Hosono, M. Yasukawa, and H. Kawazoe, “Novel oxide amorphous semiconductors: Transparent conducting amorphous oxides,” *J. Non. Cryst. Solids*, vol. 203, no. 7, pp. 334–344, 1996.
- [30] E. Fortunato, P. Barquinha, and R. Martins, “Oxide semiconductor thin-film transistors: a review of recent advances,” *Adv. Mater.*, vol. 24, no. 22, pp. 2945–86, Jun. 2012.
- [31] T. Kamiya, K. Nomura, and H. Hosono, “Present status of amorphous In–Ga–Zn–O thin-film transistors,” *Sci. Technol. Adv. Mater.*, vol. 11, no. 4, p. 044305, Aug. 2010.
- [32] Y. Shigesato and D. C. Paine, “Study of the effect of Sn doping on the electronic transport properties of thin film indium oxide,” *Appl. Phys. Lett.*, vol. 62, no. 11, p. 1268, Mar. 1993.
- [33] S. Jeong, Y.-G. Ha, J. Moon, A. Facchetti, and T. J. Marks, “Role of gallium doping in dramatically lowering amorphous-oxide processing temperatures for solution-derived indium zinc oxide thin-film transistors,” *Adv. Mater.*, vol. 22, no. 12, pp. 1346–50, Mar. 2010.
- [34] S. Parthiban and J.-Y. Kwon, “Role of dopants as a carrier suppressor and strong oxygen binder in amorphous indium-oxide-based field effect transistor,” *J. Mater. Res.*, vol. 29, no. 15, pp. 1585–1596, 2014.
- [35] H. Hosono, “Ionic amorphous oxide semiconductors: Material design, carrier transport, and device application,” *J. Non. Cryst. Solids*, vol. 352, no. 9–20 SPEC. ISS., pp. 851–858, 2006.
- [36] T. Kamiya, K. Nomura, M. Hirano, and H. Hosono, “Electronic structure of oxygen deficient amorphous oxide semiconductor a-InGaZnO 4- x : Optical analyses and first-principle calculations,” *Phys. Status Solidi*, vol. 5, no. 9, pp. 3098–3100, Jul. 2008.

- [37] a. Thakur, H. Yoo, S.-J. Kang, J. Y. Baik, I.-J. Lee, H.-K. Lee, K. Kim, B. Kim, S. Jung, J. Park, and H.-J. Shin, "Effects of Substrate Temperature on Structural, Electrical and Optical Properties of Amorphous In-Ga-Zn-O Thin Films," *ECS J. Solid State Sci. Technol.*, vol. 1, no. 1, pp. Q11–Q15, Jan. 2012.
- [38] S. Sallis, K. T. Butler, N. F. Quackenbush, D. S. Williams, M. Junda, D. a. Fischer, J. C. Woicik, N. J. Podraza, B. E. White, a. Walsh, and L. F. J. Piper, "Origin of deep subgap states in amorphous indium gallium zinc oxide: Chemically disordered coordination of oxygen," *Appl. Phys. Lett.*, vol. 104, no. 23, p. 232108, Jun. 2014.
- [39] T. Kamiya, K. Nomura, and H. Hosono, "Origins of High Mobility and Low Operation Voltage of Amorphous Oxide TFTs: Electronic Structure, Electron Transport, Defects and Doping," *J. Disp. Technol.*, vol. 5, no. 7, pp. 273–288, Jul. 2009.
- [40] A. Takagi, K. Nomura, H. Ohta, H. Yanagi, T. Kamiya, M. Hirano, and H. Hosono, "Carrier transport and electronic structure in amorphous oxide semiconductor, a-InGaZnO<sub>4</sub>," *Thin Solid Films*, vol. 486, no. 1–2, pp. 38–41, Aug. 2005.
- [41] T. Kamiya, K. Nomura, and H. Hosono, "Present status of amorphous In–Ga–Zn–O thin-film transistors," *Science and Technology of Advanced Materials*, vol. 11, no. 4. p. 044305, 2010.
- [42] K. Wasa, M. Kitabatake, and H. Adachi, *Thin Films Material Technology : Sputtering of Compound Materials*. Norwich, NY, USA: Springer-Verlag Berlin Heidelberg, 2004.
- [43] P. . Kelly and R. . Arnell, "Magnetron sputtering: a review of recent developments and applications," *Vacuum*, vol. 56, no. 3, pp. 159–172, 2000.
- [44] A. C. Jones and M. L. Hitchman, *Chemical Vapour Deposition: Precursors, Processes and Applications*. Royal Society of Chemistry, 2009.
- [45] S. A. Campbell, *Fabrication engineering at the micro and nanoscale*, 3rd ed. New York (N.Y.): Oxford University Press, 2008.

- [46] M. J. Hampden-Smith and T. T. Kodas, “Chemical vapor deposition of metals: Part 1. An overview of CVD processes,” *Chem. Vap. Depos.*, vol. 1, no. 1, pp. 8–23, Jul. 1995.
- [47] Y. Numasawa, K. Yamazaki, and K. Hamano, “ Photo-Chemical Vapor Deposition of Silicon Nitride Film by Direct Photolysis ,” *Jpn. J. Appl. Phys.*, vol. 22, no. Part 2, No. 12, pp. L792–L794, 1983.
- [48] N. Gherardi, S. Martin, and F. Massines, “ A new approach to  $\text{SiO}_2$  deposit using a  $\text{N}_2\text{-SiH}_4\text{-N}_2\text{O}$  glow dielectric barrier-controlled discharge at atmospheric pressure,” *J. Phys. D*, vol. 33, p. L104, 2000.
- [49] X. Li, E. Xin, L. Chen, J. Shi, and J. Zhang, “Effect of etching stop layer on characteristics of amorphous IGZO thin film transistor fabricated at low temperature,” *AIP Adv.*, vol. 3, no. 3, p. 032137, 2013.
- [50] M. F. Ceiler, “Plasma-Enhanced Chemical Vapor Deposition of Silicon Dioxide Deposited at Low Temperatures,” *Journal of The Electrochemical Society*, vol. 142, no. 6. p. 2067, 1995.
- [51] N. R. Rueger, “Role of steady state fluorocarbon films in the etching of silicon dioxide using  $\text{CHF}_3$  in an inductively coupled plasma reactor,” *Journal of Vacuum Science & Technology A: Vacuum, Surfaces, and Films*, vol. 15, no. 4. p. 1881, 1997.
- [52] T. Stephan, “TOF-SIMS in cosmochemistry,” *Planet. Space Sci.*, vol. 49, no. 9, pp. 859–906, 2001.
- [53] *Principles and Practice of Analytical Techniques in Geosciences*. Royal Society of Chemistry, 2014.
- [54] B. D. Cullity and S. R. Stock, *Elements of X-ray Diffraction*. 2001.
- [55] P. P. Ewald, *Fifty Years of X-Ray Diffraction: Dedicated to the International Union of Crystallography on the Occasion of the Commemoration Meeting in Munich July 1962*. Springer Science & Business Media, 2012.

- [56] I. Kojima and B. Li, “Structural characterization of thin films by X-ray reflectivity,” *Rigaku J.*, vol. 16, no. 2, pp. 31–42, 1999.
- [57] M. Yasaka, “X-ray thin-film measurement techniques,” *V. X-ray reflectivity Meas. Rigaku J.*, vol. 26, no. 2, pp. 1–9, 2010.
- [58] S. M. Sze and K. K. Ng, *Physics of Semiconductor Devices*. 2006.
- [59] D. A. Neamen, *Semiconductor physics and devices: basic principles*. 1992.
- [60] D. K. Schroder, *Semiconductor Material and Device Characterization: Third Edition*, 3th ed. New Jersey: John Wiley & Sons, Inc., 2005.
- [61] P. Migliorato, M. Seok, and J. Jang, “Determination of flat band voltage in thin film transistors: The case of amorphous-indium gallium zinc oxide,” *Appl. Phys. Lett.*, vol. 100, no. 7, p. 073506, 2012.
- [62] M. Kimura, M. Furuta, Y. Kamada, T. Hiramatsu, T. Matsuda, H. Furuta, C. Li, S. Fujita, and T. Hirao, “Extraction of Trap Densities in ZnO Thin-Film Transistors and Dependence on Oxygen Partial Pressure During Sputtering of ZnO Films,” *IEEE Trans. Electron Devices*, vol. 58, no. 9, pp. 3018–3024, Sep. 2011.
- [63] A. Neugroschel, C. T. Sah, K. M. Han, M. S. Carroll, T. Nishida, J. T. Kavalieros, and Y. Lu, “Direct-current measurements of oxide and interface traps on oxidized silicon,” *IEEE Trans. Electron Devices*, vol. 42, no. 9, pp. 1657–1662, 1995.
- [64] E. H. Nicollian and a. Goetzberger, “Mos conductance technique for measuring surface state parameters,” *Appl. Phys. Lett.*, vol. 7, no. 8, pp. 216–219, 1965.
- [65] K. Nomura, H. Ohta, A. Takagi, T. Kamiya, M. Hirano, and H. Hosono, “Room-temperature fabrication of transparent flexible thin-film transistors using amorphous oxide semiconductors.,” *Nature*, vol. 432, no. 7016, pp. 488–92, Nov. 2004.
- [66] T. Kamiya and H. Hosono, “Material characteristics and applications of transparent amorphous oxide semiconductors,” *NPG Asia Mater.*, vol. 2, no. 1, pp. 15–22, Jan. 2010.

- [67] J. Shin, J. Lee, C. Hwang, S. K. Park, and W. Cheong, "Light Effects on the Bias Stability of Transparent ZnO Thin Film Transistors," *ETRI J.*, vol. 31, no. 1, pp. 62–64, 2009.
- [68] S.-H. Choi and M.-K. Han, "Effect of channel widths on negative shift of threshold voltage, including stress-induced hump phenomenon in InGaZnO thin-film transistors under high-gate and drain bias stress," *Appl. Phys. Lett.*, vol. 100, no. 4, p. 043503, 2012.
- [69] Y. J. Kim, B. S. Yang, S. Oh, S. J. Han, H. W. Lee, J. Heo, J. K. Jeong, and H. J. Kim, "Photobias instability of high performance solution processed amorphous zinc tin oxide transistors.," *ACS Appl. Mater. Interfaces*, vol. 5, no. 8, pp. 3255–61, Apr. 2013.
- [70] M. P. Hung, D. Wang, J. Jiang, and M. Furuta, "Negative Bias and Illumination Stress Induced Electron Trapping at Back-Channel Interface of InGaZnO Thin-Film Transistor," *ECS Solid State Lett.*, vol. 3, no. 3, pp. Q13–Q16, Jan. 2014.
- [71] B. Ryu, H.-K. Noh, E.-A. Choi, and K. J. Chang, "O-vacancy as the origin of negative bias illumination stress instability in amorphous In–Ga–Zn–O thin film transistors," *Appl. Phys. Lett.*, vol. 97, no. 2, p. 022108, 2010.
- [72] J. S. Jung, K. S. Son, K.-H. Lee, J. S. Park, T. S. Kim, J.-Y. Kwon, K.-B. Chung, J.-S. Park, B. Koo, and S. Lee, "The impact of SiN[sub x] gate insulators on amorphous indium-gallium-zinc oxide thin film transistors under bias-temperature-illumination stress," *Appl. Phys. Lett.*, vol. 96, no. 19, p. 193506, 2010.
- [73] T. Fung, C. Chuang, K. Nomura, H. D. Shieh, H. Hosono, and J. Kanicki, "Photofield- effect in amorphous In- Ga- Zn- O (a- IGZO) thin- film transistors," *J. Inf. Disp.*, vol. 9, no. 4, pp. 21–29, Dec. 2008.
- [74] K.-H. Lee, J. S. Jung, K. S. Son, J. S. Park, T. S. Kim, R. Choi, J. K. Jeong, J.-Y. Kwon, B. Koo, and S. Lee, "The effect of moisture on the photon-enhanced negative bias thermal instability in Ga–In–Zn–O thin film transistors," *Appl. Phys. Lett.*, vol. 95, no. 23, p. 232106, 2009.
- [75] T.-C. Chen, T.-C. Chang, T.-Y. Hsieh, W.-S. Lu, F.-Y. Jian, C.-T. Tsai, S.-Y. Huang, and C.-S. Lin, "Investigating the degradation behavior caused by charge trapping effect under

- DC and AC gate-bias stress for InGaZnO thin film transistor,” *Appl. Phys. Lett.*, vol. 99, no. 2, p. 022104, 2011.
- [76] H. Oh, S.-M. Yoon, M. K. Ryu, C.-S. Hwang, S. Yang, and S.-H. K. Park, “Photon-accelerated negative bias instability involving subgap states creation in amorphous In–Ga–Zn–O thin film transistor,” *Appl. Phys. Lett.*, vol. 97, no. 18, p. 183502, 2010.
- [77] K. Nomura, T. Kamiya, and H. Hosono, “Highly stable amorphous In-Ga-Zn-O thin-film transistors produced by eliminating deep subgap defects,” *Appl. Phys. Lett.*, vol. 99, no. 5, p. 053505, 2011.
- [78] S. Shimakawa, D. Wang, and M. Furuta, “Photo Induced Negative Bias Instability of Zinc Oxide Thin-Film Transistors,” *Jpn. J. Appl. Phys.*, vol. 51, no. 10, p. 108003, Sep. 2012.
- [79] P. Migliorato, M. Delwar Hossain Chowdhury, J. Gwang Um, M. Seok, and J. Jang, “Light/negative bias stress instabilities in indium gallium zinc oxide thin film transistors explained by creation of a double donor,” *Appl. Phys. Lett.*, vol. 101, no. 12, p. 123502, 2012.
- [80] J. Gwang Um, M. Mativenga, P. Migliorato, and J. Jang, “Increase of interface and bulk density of states in amorphous-indium-gallium-zinc-oxide thin-film transistors with negative-bias-under-illumination-stress time,” *Appl. Phys. Lett.*, vol. 101, no. 11, p. 113504, 2012.
- [81] A. Janotti and C. G. Van De Walle, “Native point defects in ZnO,” *Phys. Rev. B - Condens. Matter Mater. Phys.*, vol. 76, no. 16, pp. 1–22, 2007.
- [82] K. Nomura, T. Kamiya, E. Ikenaga, H. Yanagi, K. Kobayashi, and H. Hosono, “Depth analysis of subgap electronic states in amorphous oxide semiconductor, a-In-Ga-Zn-O, studied by hard x-ray photoelectron spectroscopy,” *J. Appl. Phys.*, vol. 109, no. 7, p. 073726, 2011.
- [83] M. Kim, J. H. Jeong, H. J. Lee, T. K. Ahn, H. S. Shin, J.-S. Park, J. K. Jeong, Y.-G. Mo, and H. D. Kim, “High mobility bottom gate InGaZnO thin film transistors with SiO<sub>x</sub> etch stopper,” *Appl. Phys. Lett.*, vol. 90, no. 21, p. 212114, 2007.



- [84] H. Xu, L. Lan, M. Xu, J. Zou, L. Wang, D. Wang, and J. Peng, “High performance indium-zinc-oxide thin-film transistors fabricated with a back-channel-etch-technique,” *Appl. Phys. Lett.*, vol. 99, no. 25, p. 253501, 2011.
- [85] J. K. Jeong, H. Won Yang, J. H. Jeong, Y.-G. Mo, and H. D. Kim, “Origin of threshold voltage instability in indium-gallium-zinc oxide thin film transistors,” *Appl. Phys. Lett.*, vol. 93, no. 12, p. 123508, 2008.
- [86] S. Urakawa, S. Tomai, Y. Ueoka, H. Yamazaki, M. Kasami, K. Yano, D. Wang, M. Furuta, M. Horita, Y. Ishikawa, and Y. Uraoka, “Thermal analysis of amorphous oxide thin-film transistor degraded by combination of joule heating and hot carrier effect,” *Appl. Phys. Lett.*, vol. 102, no. 5, p. 053506, 2013.
- [87] F. R. Libsch and J. Kanicki, “Bias-stress-induced stretched-exponential time dependence of charge injection and trapping in amorphous thin-film transistors,” *Appl. Phys. Lett.*, vol. 62, no. 11, p. 1286, 1993.
- [88] J.-M. Lee, I.-T. Cho, J.-H. Lee, and H.-I. Kwon, “Bias-stress-induced stretched-exponential time dependence of threshold voltage shift in InGaZnO thin film transistors,” *Appl. Phys. Lett.*, vol. 93, no. 9, p. 093504, 2008.
- [89] M. E. Lopes, H. L. Gomes, M. C. R. Medeiros, P. Barquinha, L. Pereira, E. Fortunato, R. Martins, and I. Ferreira, “Gate-bias stress in amorphous oxide semiconductors thin-film transistors,” *Appl. Phys. Lett.*, vol. 95, no. 6, p. 063502, 2009.
- [90] M. P. Hung, D. Wang, T. Toda, J. Jiang, and M. Furuta, “Quantitative Analysis of Hole-Trapping and Defect-Creation in InGaZnO Thin-Film Transistor under Negative-Bias and Illumination-Stress,” *ECS J. Solid State Sci. Technol.*, vol. 3, no. 9, pp. Q3023–Q3026, Jul. 2014.
- [91] Y. Seung Rim, W. Jeong, B. Du Ahn, and H. Jae Kim, “Defect reduction in photon-accelerated negative bias instability of InGaZnO thin-film transistors by high-pressure water vapor annealing,” *Appl. Phys. Lett.*, vol. 102, no. 14, p. 143503, 2013.

- [92] K. H. Ji, J.-I. Kim, H. Y. Jung, S. Y. Park, R. Choi, U. K. Kim, C. S. Hwang, D. Lee, H. Hwang, and J. K. Jeong, "Effect of high-pressure oxygen annealing on negative bias illumination stress-induced instability of InGaZnO thin film transistors," *Appl. Phys. Lett.*, vol. 98, no. 10, p. 103509, 2011.
- [93] K. Nomura, T. Kamiya, H. Ohta, M. Hirano, and H. Hosono, "Defect passivation and homogenization of amorphous oxide thin-film transistor by wet O[sub 2] annealing," *Appl. Phys. Lett.*, vol. 93, no. 19, p. 192107, 2008.
- [94] Y. Hanyu, K. Domen, K. Nomura, H. Hiramatsu, H. Kumomi, H. Hosono, and T. Kamiya, "Hydrogen passivation of electron trap in amorphous In-Ga-Zn-O thin-film transistors," *Appl. Phys. Lett.*, vol. 103, no. 20, p. 202114, 2013.
- [95] S. Ho Rha, U. Ki Kim, J. Jung, E. Suk Hwang, S. Jun Lee, W. Jeon, Y. Woo Yoo, J.-H. Choi, and C. Seong Hwang, "Variation in the threshold voltage of amorphous-In<sub>2</sub>Ga<sub>2</sub>ZnO<sub>7</sub> thin-film transistors by ultrathin Al<sub>2</sub>O<sub>3</sub> passivation layer," *J. Vac. Sci. Technol. B Microelectron. Nanom. Struct.*, vol. 31, no. 6, p. 061205, 2013.
- [96] Y.-C. Chen, T.-C. Chang, H.-W. Li, T.-Y. Hsieh, T.-C. Chen, C.-P. Wu, C.-H. Chou, W.-C. Chung, J.-F. Chang, and Y.-H. Tai, "The suppressed negative bias illumination-induced instability in In-Ga-Zn-O thin film transistors with fringe field structure," *Appl. Phys. Lett.*, vol. 101, no. 22, p. 223502, 2012.
- [97] G. H. Kim, B. Du Ahn, H. S. Shin, W. H. Jeong, H. J. Kim, and H. J. Kim, "Effect of indium composition ratio on solution-processed nanocrystalline InGaZnO thin film transistors," *Appl. Phys. Lett.*, vol. 94, no. 23, p. 233501, 2009.
- [98] S. Lee, S. Park, S. Kim, Y. Jeon, K. Jeon, J. Park, J. Park, I. Song, C. J. Kim, Y. Park, D. M. Kim, and D. H. Kim, "Extraction of Subgap Density of States in Amorphous InGaZnO Thin-Film Transistors by Using Multifrequency Capacitance–Voltage Characteristics," *IEEE Electron Device Lett.*, vol. 31, no. 3, pp. 231–233, Mar. 2010.
- [99] Van De Walle CG, "Hydrogen as a cause of doping in zinc oxide," *Phys. Rev. Lett.*, vol. 85, no. 5, pp. 1012–5, Jul. 2000.

- [100] W.-K. Kim, S. Lee, Y. C. Cho, H. Koinuma, S.-Y. Jeong, J. M. Shin, C. R. Cho, J.-S. Bae, T.-Y. Kim, and S. Park, “Stable high conductive amorphous InGaZnO driven by hydrogenation using hot isostatic pressing,” *Appl. Phys. Lett.*, vol. 98, no. 12, p. 122109, 2011.
- [101] S. Oh, G. Choi, H. Hwang, W. Lu, and J.-H. Jang, “Hydrogenated IGZO Thin-Film Transistors Using High-Pressure Hydrogen Annealing,” *IEEE Trans. Electron Devices*, vol. 60, no. 8, pp. 2537–2541, Aug. 2013.
- [102] K. Nomura, T. Kamiya, and H. Hosono, “Effects of Diffusion of Hydrogen and Oxygen on Electrical Properties of Amorphous Oxide Semiconductor, In-Ga-Zn-O,” *ECS J. Solid State Sci. Technol.*, vol. 2, no. 1, pp. P5–P8, Nov. 2012.
- [103] T. Miyase, K. Watanabe, I. Sakaguchi, N. Ohashi, K. Domen, K. Nomura, H. Hiramatsu, H. Kumomi, H. Hosono, and T. Kamiya, “Roles of Hydrogen in Amorphous Oxide Semiconductor In-Ga-Zn-O: Comparison of Conventional and Ultra-High-Vacuum Sputtering,” *ECS J. Solid State Sci. Technol.*, vol. 3, no. 9, pp. Q3085–Q3090, Aug. 2014.
- [104] D. G. Thomas and J. J. Lander, “Hydrogen as a Donor in Zinc Oxide,” *J. Chem. Phys.*, vol. 25, no. 6, p. 1136, 1956.
- [105] M. P. Hung, D. Wang, J. Jiang, and M. Furuta, “Negative Bias and Illumination Stress Induced Electron Trapping at Back-Channel Interface of InGaZnO Thin-Film Transistor,” *ECS Solid State Lett.*, vol. 3, no. 3, pp. Q13–Q16, Jan. 2014.
- [106] K. Tominaga, N. Ueshiba, Y. Shintani, and O. Tada, “High-Energy Neutral Atoms in the Sputtering of ZnO,” *Jpn. J. Appl. Phys.*, vol. 20, no. 3, pp. 519–526, Mar. 1981.
- [107] J. Jia, Y. Torigoshi, and Y. Shigesato, “In situ analyses on negative ions in the indium-gallium-zinc oxide sputtering process,” *Appl. Phys. Lett.*, vol. 103, no. 1, p. 013501, 2013.
- [108] D. Wang, M. P. Hung, J. Jiang, T. Toda, and M. Furuta, “Suppression of Degradation Induced by Negative Gate Bias and Illumination Stress in Amorphous InGaZnO Thin-Film Transistors by Applying Negative Drain Bias,” *ACS Appl. Mater. Interfaces*, vol. 6, no. 8, pp. 5713–5718, Apr. 2014.

- [109] H.-K. Noh, J.-S. Park, and K. J. Chang, “Effect of hydrogen incorporation on the negative bias illumination stress instability in amorphous In-Ga-Zn-O thin-film-transistors,” *J. Appl. Phys.*, vol. 113, no. 6, p. 063712, 2013.
- [110] J. H. Jeong, H. W. Yang, J.-S. Park, J. K. Jeong, Y.-G. Mo, H. D. Kim, J. Song, and C. S. Hwang, “Origin of Subthreshold Swing Improvement in Amorphous Indium Gallium Zinc Oxide Transistors,” *Electrochem. Solid-State Lett.*, vol. 11, no. 6, p. H157, 2008.
- [111] S. Yang, D.-H. Cho, M. K. Ryu, S.-H. K. Park, C.-S. Hwang, J. Jang, and J. K. Jeong, “Improvement in the photon-induced bias stability of Al-Sn-Zn-In-O thin film transistors by adopting AlO<sub>x</sub> passivation layer,” *Appl. Phys. Lett.*, vol. 96, no. 21, p. 213511, 2010.
- [112] J.-Y. Kwon, K. S. Son, J. S. Jung, K.-H. Lee, J. S. Park, T. S. Kim, K. H. Ji, R. Choi, J. K. Jeong, B. Koo, and S. Lee, “The Impact of Device Configuration on the Photon-Enhanced Negative Bias Thermal Instability of GaInZnO Thin Film Transistors,” *Electrochem. Solid-State Lett.*, vol. 13, no. 6, p. H213, 2010.
- [113] S. Choi, J. Jang, J. Kim, and M. Han, “Low-Temperature Organic ( CYTOP ) Passivation for Improvement of Electric Characteristics and Reliability in IGZO TFTs,” vol. 33, no. 3, pp. 381–383, 2012.
- [114] a. Hino, T. Kishi, H. Tao, S. Morita, K. Hayashi, and T. Kugimiya, “Study of Electronic Structure and Film Composition at the Back Channel Surface of Amorphous In-Ga-Zn-O Thin Films,” *ECS J. Solid State Sci. Technol.*, vol. 2, no. 4, pp. P156–P159, Feb. 2013.
- [115] J.-Y. Kwon, J. S. Jung, K. S. Son, K.-H. Lee, J. S. Park, T. S. Kim, J.-S. Park, R. Choi, J. K. Jeong, B. Koo, and S. Y. Lee, “The impact of gate dielectric materials on the light-induced bias instability in Hf-In-Zn-O thin film transistor,” *Appl. Phys. Lett.*, vol. 97, no. 18, p. 183503, 2010.
- [116] C.-K. Lee, A. Y. Hwang, H. Yang, D.-H. Kim, J.-U. Bae, W.-S. Shin, and J. K. Jeong, “Improvement in the Photo-Bias Stability of Zinc Tin Oxide Thin-Film Transistors by

- Introducing a Thermal Oxidized TiO<sub>2</sub> Film as a Hole Carrier Blocking Layer,” *IEEE Trans. Electron Devices*, vol. 60, no. 12, pp. 4165–4172, Dec. 2013.
- [117] W. Körner, D. F. Urban, and C. Elsässer, “Origin of subgap states in amorphous In-Ga-Zn-O,” *J. Appl. Phys.*, vol. 114, no. 16, p. 163704, 2013.
- [118] D. H. Lee, K. Kawamura, K. Nomura, T. Kamiya, and H. Hosono, “Large Photoresponse in Amorphous In–Ga–Zn–O and Origin of Reversible and Slow Decay,” *Electrochem. Solid-State Lett.*, vol. 13, no. 9, p. H324, 2010.
- [119] Y.-C. Chen, T.-C. Chang, H.-W. Li, W.-F. Chung, T.-Y. Hsieh, Y.-H. Chen, W.-W. Tsai, W.-J. Chiang, and J.-Y. Yan, “Dependence of Light-Accelerated Instability on Bias and Environment in Amorphous Indium-Gallium-Zinc-Oxide Thin Film Transistors,” *ECS J. Solid State Sci. Technol.*, vol. 2, no. 4, pp. Q74–Q76, Feb. 2013.
- [120] a. Suresh and J. F. Muth, “Bias stress stability of indium gallium zinc oxide channel based transparent thin film transistors,” *Appl. Phys. Lett.*, vol. 92, no. 3, p. 033502, 2008.
- [121] J. Lee, I. Cho, J. Lee, and H. Kwon, “Bias-stress-induced stretched-exponential time dependence of threshold voltage shift in InGaZnO thin film transistors,” *Appl. Phys. Lett.*, vol. 93, no. 093504, pp. 3–5, 2008.
- [122] P. Barquinha, L. Pereira, G. Gonçalves, R. Martins, D. Kuščer, M. Kosec, and E. Fortunato, “Performance and Stability of Low Temperature Transparent Thin-Film Transistors Using Amorphous Multicomponent Dielectrics,” *J. Electrochem. Soc.*, vol. 156, p. H824, 2009.
- [123] J. Lee, J.-S. Park, Y. S. Pyo, D. B. Lee, E. H. Kim, D. Stryakhilev, T. W. Kim, D. U. Jin, and Y.-G. Mo, “The influence of the gate dielectrics on threshold voltage instability in amorphous indium-gallium-zinc oxide thin film transistors,” *Appl. Phys. Lett.*, vol. 95, no. 12, p. 123502, 2009.
- [124] K. Nomura, T. Kamiya, M. Hirano, and H. Hosono, “Origins of threshold voltage shifts in room-temperature deposited and annealed a-In–Ga–Zn–O thin-film transistors,” *Appl. Phys. Lett.*, vol. 95, no. 1, p. 013502, 2009.

- [125] M. D. H. Chowdhury, P. Migliorato, and J. Jang, "Time-temperature dependence of positive gate bias stress and recovery in amorphous indium-gallium-zinc-oxide thin-film-transistors," *Appl. Phys. Lett.*, vol. 98, no. 15, p. 153511, 2011.
- [126] H. Yamazaki, M. Fujii, Y. Ueoka, Y. Ishikawa, M. Fujiwara, E. Takahashi, and Y. Uraoka, "P-22 Highly Reliable a-IGZO TFTs with SiN X Gate Insulator deposited by SiF<sub>4</sub> / N<sub>2</sub>," *AM-FPD' 12*, pp. 163–165, 2012.
- [127] H. Yamazaki, Y. Ishikawa, M. Fujii, Y. Ueoka, M. Fujiwara, E. Takahashi, Y. Andoh, N. Maejima, H. Matsui, F. Matsui, H. Daimon, and Y. Uraoka, "The Influence of Fluorinated Silicon Nitride Gate Insulator on Positive Bias Stability toward Highly Reliable Amorphous InGaZnO Thin-Film Transistors," *ECS J. Solid State Sci. Technol.*, vol. 3, no. 2, pp. Q20–Q23, 2013.
- [128] J. Jiang, T. Toda, M. P. Hung, D. Wang, and M. Furuta, "Highly stable fluorine-passivated In–Ga–Zn–O thin-film transistors under positive gate bias and temperature stress," *Appl. Phys. Express*, vol. 7, p. 114103, 2014.
- [129] X. Huang, C. Wu, H. Lu, F. Ren, D. Chen, R. Zhang, and Y. Zheng, "Enhanced bias stress stability of a-InGaZnO thin film transistors by inserting an ultra-thin interfacial InGaZnO:N layer," *Appl. Phys. Lett.*, vol. 102, no. 19, p. 193505, 2013.
- [130] T. Toda, D. Wang, J. Jiang, M. P. Hung, and M. Furuta, "Quantitative Analysis of the Effect of Hydrogen Diffusion from Silicon Oxide Etch-Stopper Layer into Amorphous In-Ga-Zn-O on Thin-Film Transistor," *IEEE Trans. Electron Devices*, vol. 61, no. 11, pp. 3762–3767, 2014.
- [131] N. Shiono, "Interface Trapped Charge Generation and Electron Trapping Kinetics in MOSFET's due to Substrate Hot-Electron Injection into Gate SiO<sub>2</sub>," *J. Electrochem. Soc.*, vol. 129, no. 8, p. 1760, 1982.
- [132] M. Kimura, T. Nakanishi, K. Nomura, T. Kamiya, and H. Hosono, "Trap densities in amorphous-InGaZnO<sub>4</sub> thin-film transistors," vol. 133512, pp. 1–4, 2008.

- [133] J. M. Noras, "Extraction of interface state attributes from MOS conductance measurements," *Solid. State. Electron.*, vol. 30, no. 4, pp. 433–437, 1987.
- [134] N. Konofaos, "New evidence on the relation between tunnelling and trap density at insulator/semiconductor interfaces," *Semicond. Sci. Technol.*, vol. 16, no. 8, pp. 733–738, 2001.
- [135] W. Fahrner and A. Geotzberger, "Energy Dependence of electrical properties of interface state in Si-SiO<sub>2</sub> interfaces," *Appl. Phys. Lett.*, vol. 17, no. 1, p. 16, 1970.
- [136] E. H. Nicollian, a. Goetzberger, and a. D. Lopez, "Expedient method of obtaining interface state properties from MIS conductance measurements," *Solid. State. Electron.*, vol. 12, no. 12, pp. 937–944, 1969.
- [137] N. Konofaos and E. K. Evangelou, "Electrical characterization of the SiON/Si interface for applications on optical and MOS devices," *Semicond. Sci. Technol.*, vol. 18, no. 1, pp. 56–59, 2002.
- [138] L. Qiang and R. Yao, "A New Extraction Method of Trap States in Amorphous InGaZnO Thin-Film Transistors," *J. Disp. Technol.*, vol. 11, no. 4, pp. 325–329, 2015.
- [139] X. Zou, G. Fang, L. Yuan, X. Tong, and X. Zhao, "A comparative study of amorphous InGaZnO thin film transistor with HfO<sub>x</sub>Ny and HfO<sub>2</sub> Gate dielectric," *Semicond. Sci. Technol.*, vol. 25, no. 5, p. 055006, 2010.
- [140] M. Kimura, T. Nakanishi, K. Nomura, T. Kamiya, and H. Hosono, "Trap densities in amorphous-InGaZnO[sub 4] thin-film transistors," *Appl. Phys. Lett.*, vol. 92, no. 13, p. 133512, 2008.
- [141] T. T. Trinh, V. D. Nguyen, K. Ryu, K. Jang, W. Lee, S. Baek, J. Raja, and J. Yi, "Improvement in the performance of an InGaZnO thin-film transistor by controlling interface trap densities between the insulator and active layer," *Semicond. Sci. Technol.*, vol. 26, no. 8, p. 085012, 2011.

- [142] D. a. Buchanan, J. H. Stathis, and P. R. Wagner, “Trapped positive charge in plasma-enhanced chemical vapor deposited silicon dioxide films,” *Appl. Phys. Lett.*, vol. 56, no. 1990, p. 1037, 1990.
- [143] F. Jiménez-Molinos, a. Palma, F. Gámiz, J. Banqueri, and J. a. López-Villanueva, “Physical model for trap-assisted inelastic tunneling in metal-oxide-semiconductor structures,” *J. Appl. Phys.*, vol. 90, no. 7, pp. 3396–3404, 2001.
- [144] D. Garetto, Y. M. Randriamihaja, A. Zaka, D. Rideau, A. Schmid, H. Jaouen, and Y. Leblebici, “Analysis of defect capture cross sections using non-radiative multiphonon-assisted trapping model,” *Solid. State. Electron.*, vol. 71, pp. 74–79, 2012.
- [145] D. Sands, K. M. Brunson, and C. B. Thomas, “The relative contributions of recombination and tunnelling at interface states to the a.c. conductance of metal-insulator-semiconductor diodes,” *Solid. State. Electron.*, vol. 30, no. 5, pp. 543–548, May 1987.
- [146] K. Hoshino, D. Hong, H. Q. Chiang, and J. F. Wager, “Constant-Voltage-Bias Stress Testing of a-IGZO Thin-Film Transistors,” *IEEE Trans. Electron Devices*, vol. 56, no. 7, pp. 1365–1370, Jul. 2009.
- [147] H.-H. Nahm and Y.-S. Kim, “Undercoordinated indium as an intrinsic electron-trap center in amorphous InGaZnO<sub>4</sub>,” *NPG Asia Mater.*, vol. 6, no. 11, p. e143, Nov. 2014.